

Numerical study on non-Hermitian quantum dynamics

非エルミート量子系の動力学の数値的研究

by

Takahiro Orito

折戸 隆寛

A Doctor Thesis

博士論文

Submitted to

the Graduate School of the Advanced Science and Engineering,

Hiroshima University

on January 26, 2023

in Partial Fulfillment of the Requirements

for the Degree of Engineering

Thesis Supervisor: Yositake Takene 高根 美武

Professor of the Graduate School of the Advanced Science and

Engineering, Hiroshima University

Acknowledgements

I would like to thank my supervisor, Professor Yositake Takane, for his advice on my studies. He gave opportunities to enable me to deal with the problem and topic of my interest throughout my three years of study at Hiroshima University.

I am also grateful to Dr. Ken-Ichiro Imura for his patience and sincere support. He has always been available for consulting on personal and scientific problems. The discussion with him not only advanced my studies but also comprised the valuable, enjoyable time spent. Moreover, I am grateful to him for reading my thesis and providing constructive comments.

I would like to thank all members of the thesis committee, Prof. Yutaka Kadoya, Prof. Holger Friedrich Hofmann, Prof. Seiji Higashitani, and Prof. Munehiro Nishida, for the acceptance of the review of my thesis.

Outside of Hiroshima University, I am grateful to Prof. Ikuo Ichinose of Nagoya Institute of Technology and Prof. Yoshihito Kuno of Akita University for various discussions and advice.

Furthermore, I am thankful to my family for their understanding and support.

Finally, I would like to acknowledge the financial support received from the Japan Science and Technology Agency (JST) through the Program for Developing and Supporting the Next-Generation of Innovative Researchers at Hiroshima University (JST SPRING, Grant Number JPMJSP2132).

Contents

1	Introduction	1
2	(De)localization transition of (non-)Hermitian systems	5
2.1	Quantification of the degree of localization and delocalization in quantum mechanics	6
2.2	Absence of delocalization in one space dimension and case of the Aubry–André model	7
2.3	Case of the Hatano–Nelson model: a non-Hermitian extension of quantum mechanics	9
2.4	Localization/delocalization phenomena from the perspective of wave packet dynamics	13
3	ETH, MBL, and entanglement entropy	14
3.1	Eigenstate thermalization hypothesis (ETH)	14
3.2	Many-body localization (MBL)	17
3.3	Quantum entanglement and entanglement entropy	19
3.3.1	General definition of the entanglement	19
3.3.2	Two types of contributions to the entanglement entropy: number and configuration entropies	20
3.4	Static and dynamical properties of the ETH and MBL phases	22
3.4.1	Static property of S_{tot} in the ETH and MBL phases	22
3.4.2	Dynamical property of the ETH and MBL phases: Imbalance and S_{tot}	23
3.5	Slow logarithmic growth of entanglement entropy in the MBL phase	25
3.6	Non-Hermitian many-body localization	29
4	Non-Hermitian wave packet dynamics	31
4.1	Single-particle case: Hatano-Nelson model and Aubry-André model	31
4.2	Case of an interacting system	38
5	Non-Hermitian entanglement dynamics	42
5.1	Entanglement dynamics	42
5.2	Entanglement entropy in the non-interacting limit: wave packet spreading versus entanglement entropy	43
5.3	Case of $V \neq 0$ and $g \neq 0$: non-monotonic behavior	45
5.4	Effect of finite size and nonequilibrium steady state	47
5.5	Profile of the reduced density matrix	50
6	Concluding remarks	53

A	Notes on the choice of the boundary condition	56
B	Free particle wave-packet dynamics in a Hermitian system	58
C	Free particle wave-packet dynamics in a non-Hermitian system with $\text{Im } \epsilon_k \neq 0$	60
D	Effects of anticommutation relation on entanglement dynamics	62
E	The entanglement entropy in the ETH and MBL phases (Hermitian case)	64
	References	65

Chapter 1

Introduction

Does a quantum mechanical system thermalize? The answer is certainly yes; research is underway to establish that an isolated many-body quantum system is thermalized by its dynamics. Here, thermalization refers to the process via which, through time evolution, the quantum expectation value of an observable tends to approach and eventually becomes practically identical to the corresponding microcanonical expectation value. The eigenstate thermalization hypothesis (ETH) [1, 2, 3] proposes sufficient conditions for such thermalization. Subsequent theoretical, numerical, and experimental studies have shown the validity of the hypothesis under various conditions.

On contrary, many-body localization (MBL) [4, 5, 6, 7, 8, 9, 10, 11, 12, 13] phase is rather an exceptional case wherein this ETH breaks down. In the presence of strong disorder, the wave function is known to localize at the level of single-particle quantum mechanics (Anderson localization) [14]. In the presence of inter-particle interaction, localization still occurs; however, it occurs in the Hilbert/Fock space; as in case of MBL. In time evolution the initial density (or spin) pattern remains essentially unchanged, while the expectation value of an observable does not reach its microcanonical ensemble averaged value. This lack of thermalization stems from the emergence of an extensive number of locally conserved quantities, each of which is called a local integral of motion (LIOM). Since a conserved quantity commutes with the Hamiltonian, LIOM acts as a constraint to dynamics and prohibits the quantum state from thermalization. Hereafter, we state that a system is in the ETH phase if ETH holds therein.

The entanglement entropy S is a measure of non-local correlation (entanglement) between subsystems; here, it is presumed that the system is divided into two parts and only one subsystem is focused on (for a more precise definition of the entanglement, see Chapter 3). If the entire system is in a pure state, the subsystems attain a mixed state if $S \neq 0$, implying the emergence of a certain *ensemble*. The entanglement entropy S measures the entropy of such an ensemble, and the expectation value of an observable in the subsystem is equal to its statistical average over this ensemble. The behaviors of S is qualitatively different in the MBL and ETH phases in terms of both their static [15, 16, 17, 18, 19] and dynamical [20, 21, 22, 23, 24, 25] properties. Therefore, the entanglement entropy S can be used for characterizing the MBL and ETH phases. For an eigenstate obeying ETH, the ensemble describing a subsystem is akin to a thermal (statistical) ensemble, and thus the expectation value of an observable is regarded as a thermal expectation value. This implies that S of the eigenstate obeys a

volume-law scaling since thermodynamic entropy is extensive. In contrast, in the MBL phase, an eigenstate only possesses a correlation within a localization length, and thus S of the eigenstate obeys an area-law scaling [15, 16, 17, 18, 19]. Therefore, the ETH-MBL transition involves the transition of entanglement from volume-law to area-law scaling.

Particle transport generally involves the growth of entanglement entropy with time evolution of an initial state expressed in the form of a wave packet. Such particle transport is hindered by the random potential, and thus, a power-law growth of S [25] in the ETH phase gradually decreases as the disorder strength increases. However, even in the MBL phase, a logarithmic growth of S with time still exists. This relaxation dynamics, i.e., the logarithmic growth of S [20, 21, 22], is unique to the MBL phase. For the Anderson localization (AL) phase in a noninteracting system, in an early time scale, S exhibits similar behavior to the MBL phase, although S ceases to increase after its initial growth. An extensive set of LIOMs provides an intuitive explanation for this behavior: even if the interaction is exponentially small, the time evolution of a wave packet becomes more complicated than that in the AL phase owing to the mutual interaction of LIOMs [see Eq. (3.17)].

Another motivation of this work lies in recent renewed interests [26, 27, 28, 29, 30, 31, 32] in the previously proposed (late 1990's) non-Hermitian extension of quantum mechanics [33, 34, 35]. Remarkable advances in experiments in the last decades have changed and is still changing the shape of theoretical research.¹ One of the advantages of such experiments is their high controllability. This realizes a bonafide example of the so-called open quantum system, that is essentially a quantum system coupled to the measuring equipment or surrounding environment. Such a system is effectively described by a non-Hermitian Hamiltonian, whose characteristics are essentially different from those of the original closed systems, excluding the environment. In the effective tight-binding model in Refs. [33, 34], lies in the non-reciprocity of hopping amplitudes;² the amplitude with which an electron hops to the right neighboring site is different from the one with which it hops to the left neighboring site.

In this thesis, we consider the case of the many-body Hatano–Nelson model, wherein nearest-neighbor short-range interactions are incorporated into the original tight-binding model; see Eq. (2.12). In this non-Hermitian many-body system, we have examined how/whether existing scenarios on Hermitian ETH-MBL systems function, particularly focusing on the behavior of entanglement entropy. Few existing studies regarding this system include Refs. [36, 37], typical entanglement dynamics are stated to be qualitatively similar to the Hermitian case (at least in an early time scale). In this thesis, I show that this statement is validated based on observations only in the extreme cases of exceedingly weak and strong disorder, without considering the typical behavior of the entanglement entropy $S(t)$ observed in the moderate disorder case. In the moderate disorder case, $S(t)$ typically turns to decrease after an initial growth, exhibiting a remarkable non-

¹The theoretical research on thermalization (ETH) and MBL have also been much pushed forward by such remarkable advances in the experiments, which has enabled us (experimentalists) to investigate thermalization and MBL in an isolated many-body quantum system in real experimental setups.

²Another typical example of the non-Hermitian effective Hamiltonian is the case of complex potential, which has been much studied from the viewpoint of PT symmetry [35].

monotonic time dependence. An interesting feature of the Hatano–Nelson model, i.e., the localization length ξ in the Hermitian limit is definitely related to the critical value g_c of a non-reciprocal parameter at the localization–delocalization transition point in the non-Hermitian regime (see Chapter 2 for details). This relation has not been examined in the presence of many-body effects.

Specifically, the following unsolved issues have been clarified in this thesis:

- i the extent to which non-reciprocal hopping qualitatively changes the entanglement behavior, and
- ii whether the relation between ξ and g_c still holds in a many-body system.

Note the result reported in Ref. [38]: the saturation value of $S(t)$ in a many-body system with non-reciprocity increases as the disorder strength increases under a specific parameter setting. This indicates that non-reciprocity affects the entanglement behavior and is related to issue (i). However, the authors of Ref. [38] did not investigate this behavior; instead, they focused on another feature: non-monotonic time evolution of $S(t)$. In this study, the increase in the saturation value of $S(t)$ is found to disappear if the system approaches the localization transition point, which is determined via a separate analysis [38]. This suggests that one can detect the transition between the MBL and ETH phases by observing the time evolution of $S(t)$, paving a way for tackling issue (ii) from the perspective of dynamics.

In the Hermitian case, the spreading of a wave packet (quasiparticle) is closely related to the growth of $S(t)$ over time [39, 40, 41]. Assume that a pair of entangled quasiparticles is given as an initial state in the system comprising of two subsystems. $S(t)$ grows if the two quasiparticles propagate in opposite directions in different subsystems. Consequently, in the clean limit, the entanglement entropy increases as $S(t) \propto 2v_f t$, where v_f is the velocity of the quasiparticles. For a disordered system, a wave packet ceases to spread, and thus the growth of entanglement entropy is suppressed. The author of Ref. [42] has reported that a wave-packet spreading in non-Hermitian systems with nonreciprocal hopping is substantially different from that in Hermitian systems. In the presence of non-reciprocity, a wave packet does not spread; rather it slides in the direction determined by the non-reciprocity. This behavior is immune to disorder, and the wave packet spreads through the entire system only in the vicinity of the transition point. Therefore, the non-reciprocal hopping should strongly affect the entanglement entropy.

Here, we systematically study the entanglement dynamics in non-Hermitian systems with non-reciprocal hopping. Notably, non-reciprocal hopping qualitatively changes the entanglement dynamics compared with that in the Hermitian system. Interestingly, disorder generates entanglement entropy S in the delocalized phase, suppressing S in the localized phase, enabling estimation of the localization–delocalization transition from $S(t)$. Additionally, we validate that a non-reciprocal parameter g relates to the localization length in a non-interacting many-body system. This relation holds even in an interacting many-body system. We also provide a more detailed reason why entanglement dynamics leads to non-monotonic behavior over time. We employ number and configuration entropies (S_{num} and S_{conf}) that play different roles in entanglement dynamics and constitute the entanglement entropy S_{tot} as $S_{\text{tot}} = S_{\text{num}} + S_{\text{conf}}$.

In addition to the work described in this thesis, the following relevant topics have also been studied:

1. Fock-space localization in many-body systems [43, 44]
2. Many-body localization in a Flat-band system [45, 46]
3. Many-body localization with topological order [47, 48]
4. Information spreading and scrambling in many-body systems [49, 50].

This thesis is structured as follows. In Chapter 2, we review the localization phenomenon in Hermitian and non-Hermitian (Hatano–Nelson model) systems. In Chapter 3, we review the characteristic features of the ETH and MBL phases in the Hermitian and non-Hermitian systems. We particularly focus on the properties of entanglement entropy in these phases. In Chapter 4, we demonstrate how a wave packet spreads in a non-Hermitian disordered system with non-reciprocal hopping. Employing single and few particle (three-particle) cases, we show that the spreading of wave-packet is considerably different from its behavior in the Hermitian system. In Chapter 5, we examine entanglement dynamics, highlighting its non-monotonic time evolution and a characteristic disorder-dependence. We also study the size dependence of the results, predicting an unusual area-volume-area law crossover of the maximal entanglement entropy, which is not observed in the Hermitian case and allows us to estimate the localization transition even in dynamics. Finally, we examine and visualize the characteristic stages in the evolution of the reduced density matrix, which closely relates to the entanglement entropy. We emphasize that the difference in its behavior between Hermitian and non-Hermitian cases arises from the imaginary part of eigenenergy. Chapter 6 incorporates the concluding remarks. Details are provided in Appendices. In this thesis, Quspin [51, 52] is used to compute various physical quantities of a quantum many-body system.

Chapter 2

(De)localization transition of (non-)Hermitian systems

In quantum mechanics, disorder in the form of a random potential tends to localize the wave function of a quantum particle [14]. Figure 2.1 shows such a localized wave function (plotted in orange) and a delocalized wave function (plotted in blue) for comparison, both in real space [panel (a)] and the corresponding reciprocal space [panel (b)]. Here, W represents the strength of disorder, ¹ i.e., the magnitude of the random potential. Naturally, the case of $W = 0$ falls within the clean limit, while the relatively strong disorder case of $W = 4$ corresponds to the localized regime. In the case of $W = 0$, the eigen wave function $\psi(j)$ is a superposition of plane waves e^{ikj} and e^{-ikj} , extending uniformly to the entire system, so that $|\psi(j)|^2$ is almost constant in real space (or in the local basis) [panel (a)], where j specifies a site in real space. Contrastingly, it shows only the δ -function peaks in the reciprocal space [panel (b)]. This is precisely prescribed by the uncertainty principle of quantum mechanics. Similarly, in case of $W = 4$, the eigen wave function $\psi(j)$ becomes a localized wave function, expressed in the form of a localized function in the local basis [orange plots in panel (a)], while it is almost uniformly distributed (up to a weak modulation associated with the quasi periodicity) in the reciprocal space.

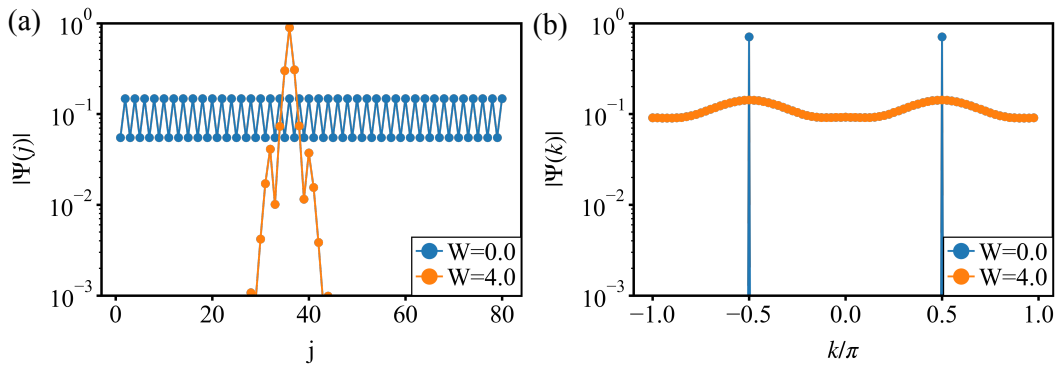


Figure 2.1: A (de)localized eigenstate in the (a) local basis ($|j\rangle$) and (b) reciprocal space ($|k\rangle$) with a specific disorder configuration.

In this chapter, we first distinguish such localized and delocalized wave functions in a quantitative manner, i.e., the approach to quantify the degree of localization in quantum mechanics (Section 2.1). We introduce a common knowledge

¹Here, the strength W of disorder is in the sense of Eq. (2.7).

of the field: in the model case of one spatial dimension (specifically focused on in this study), as soon as moderate randomness or disorder (in the form of a very weak random potential) is introduced into a system, the wave function is immediately localized, so that delocalization never occurs in one spatial dimension, except in the clean limit ² of $W = 0$. We argue the existence of certain (known) exceptions to this common knowledge, even in one spatial dimension. Furthermore, we also argue that the indices describing the localization–delocalization transition introduced in Section 2.1 are indeed useful in the description of these systems. The case of correlated disorder [Aubry–André (AA) model] [53] (Section 2.2) and that of non-reciprocal hopping [Hatano–Nelson model] [33, 34, 54] (Section 2.3) include such exceptional cases. Finally, we introduce a perspective on the localization/delocalization phenomena from quantum dynamics, thus far described as properties of the eigen wave function.

2.1 Quantification of the degree of localization and delocalization in quantum mechanics

The probability amplitude of a localized eigenstate features an imbalanced distribution, whereas a delocalized eigenstate exhibits a uniform distribution. Let us introduce a normalized wave function ψ_j , where j specifies a site in the system. One of the effective measures to quantify the degree of localization and delocalization is the inverse participation ratio (IPR):

$$\text{IPR} = \sum_j |\psi_j|^4 \quad (2.1)$$

or multifractal dimension (MFD):

$$\text{MFD} = -\frac{\ln(\text{IPR})}{\ln(L)}. \quad (2.2)$$

In the delocalized phase, the probability amplitude $|\psi_j|^2$ is uniformly distributed over the entire system, and thus, the probability amplitude is $|\psi_j|^2 \sim \frac{1}{L}$. Substituting $\frac{1}{L^2}$ for $|\psi_j|^4$ in Eq. (2.1), we obtain

$$\text{IPR} = \sum_j |\psi_j|^4 \sim \sum_j \frac{1}{L^2} \sim \frac{1}{L}, \quad (2.3)$$

which results in

$$\text{MFD} = -\frac{\ln(\text{IPR})}{\ln(L)} \sim -\frac{\ln(1/L)}{\ln(L)} = 1. \quad (2.4)$$

While in the localized phase, the probability amplitude exponentially localizes in a domain of width ξ centered at a point called the localization center, where ξ is referred to as the localization length. If the probability amplitude is uniformly

²In this sense, the clean limit is an exceptional and unstable limit, at least in the Hermitian case with uncorrelated disorder [cf. Eq. (2.7)].

distributed in the domain, the typical probability amplitude becomes $|\psi_j|^2 \sim \frac{1}{\xi}$. Substituting $\frac{1}{\xi^2}$ for $|\psi_j|^4$ in Eq. (2.1), we obtain

$$\text{IPR} = \sum_j |\psi_j|^4 \sim \sum_{|j-j_0| \in \xi/2} |\psi_j|^4 = \xi \frac{1}{\xi^2} = \frac{1}{\xi}, \quad (2.5)$$

which results in

$$\text{MFD} = -\frac{\ln(\text{IPR})}{\ln(L)} \sim \frac{\ln(\xi)}{\ln(L)}. \quad (2.6)$$

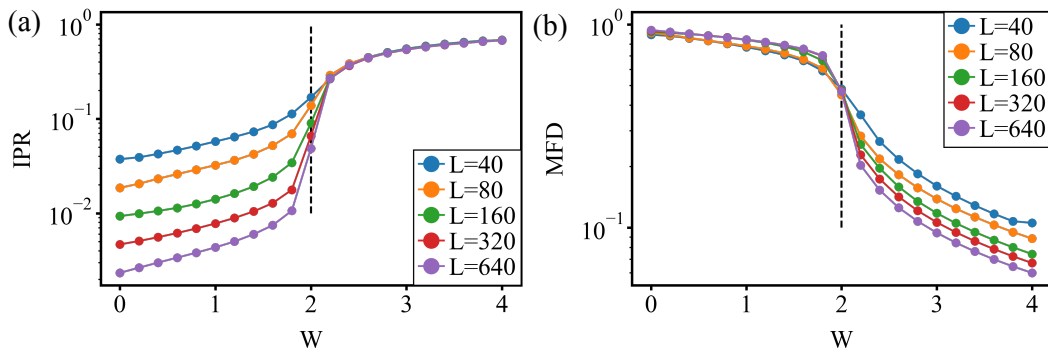


Figure 2.2: IPR and MFD in the AA model as a function of W with $\phi = 0$. In calculating (a) IPR and (b) MFD, a specific disorder configuration is used for each value of L .

Figure 2.2 shows the IPR (panel (a)) and MFD (panel (b)) as a function of W with various values of L . At weak disorder ($W \sim 0$), IPR shows size-dependent behavior, which is consistent with Eq. (2.3). As W increases, IPR gradually increases in a weakly disordered regime, suddenly increases near $W = 2J$ (localization transition point), and it exhibits size-independent behavior ($\sim 1/\xi$), which is consistent with Eq. (2.5). In contrast to IPR, under weak disorder ($W \sim 0$), MFD exhibits size-independent behavior (cf. Eq. (2.4)). As W increases, MFD gradually decreases in a weakly disordered regime, suddenly decreases near $W = 2J$, and it exhibits size-dependent behavior ($\sim \ln(\xi)/\ln(L)$) (cf. Eq. (2.6)). Remarkably, MFD's with different system sizes cross at $W = 2J$, represented by the black dashed line. This implies that MFD is an effective good indicator, enabling the estimation of the localization–delocalization transition.

2.2 Absence of delocalization in one space dimension and case of the Aubry–André model

We have discussed in the previous section that disorder tends to localize the wave function in quantum mechanics. This is known as Anderson localization, and is quantified [14, 55] through analyses of the so-called Anderson model:

$$H = \sum_j [-J(|j\rangle\langle j+1| + |j+1\rangle\langle j|) + W_j|j\rangle\langle j|], \quad (2.7)$$

where J represents the strength of hopping and W_j denotes the random on-site potential disorder at site j . As mentioned at the beginning of this Chapter,

the localization–delocalization transition is commonly known to not occur in one spatial dimension since the wave function tends to be localized if negligible amount of disorder is introduced into the system. In higher dimensions, even in the presence of such random potential, a particle (usually an electron) can still avoid it and move almost freely, since there is sufficient room/space or allowed paths to evade the randomness. The corresponding wave function in this case remains delocalized/extended unless the random potential is exceedingly strong. This common knowledge is well-established through analyses of the Anderson model (2.7) in the case of the random potential W_j distributed randomly but uniformly in the range $W_j \in [-W, W]$, where the (half) width W of this uniform distribution represents the strength of disorder.

The uniform distribution, which is the most standard form of random potential in the study of Anderson localization, is referred to as uncorrelated disorder, in contrast to the case of correlated disorder, which we will discuss next. The case of quasi-periodic disorder or the Aubry–André (AA) model falls within this second category:

$$W_j = W \cos(2\pi\alpha j + \phi), \quad (2.8)$$

where α is an irrational number, considered typically to be the following inverse golden ratio:

$$\alpha = \frac{\sqrt{5} - 1}{2}. \quad (2.9)$$

An unimportant constant ϕ in Eq. (2.8) is set equal to 0 in this chapter. Since an irrational number α may be suitably approximated by a fraction M/N with both M and N being a large integer: $M, N \gg 1$, so that $\alpha j \bmod 1$ assumes an almost random number between 0 and 1 for integer j 's. Correspondingly, $2\pi\alpha j$ represents an almost random phase, and the periodic potential (2.8) exhibits an extremely large period. We can regard it as a quasi-periodic potential representing correlated disorder. The Anderson Hamiltonian (2.7) with the quasi-periodic potential (2.8) is referred to as the AA model. Previous studies [56, 57, 58] show that in this model, the delocalized phase continues to exist even in one space dimension and at a finite disorder strength, indicating that the effect of correlated disorder is weak compared with that of uncorrelated disorder. This implies that by adopting the quasi-periodic potential (2.8), we can compare differences between the delocalized and localized phases in one spatial dimension under various conditions, such as with and without interaction and non-reciprocity. For this reason, we employ the AA model in the remainder of this thesis.

In the AA model, the existence of a delocalized phase and that of a localized phase are related to duality of the model. In the following, we see that this duality of the AA model allows us to identify the critical disorder strength W_c at the delocalization–localization transition. We introduce the following unitary transformation with integer \tilde{k} :

$$|j\rangle = \frac{1}{\sqrt{L}} \sum_{\tilde{k}} \exp(2\pi i\alpha\tilde{k}j/L) |\tilde{k}\rangle, \quad (2.10)$$

which is different from the Fourier transformation ($|j\rangle = \frac{1}{\sqrt{L}} \sum_{\tilde{k}} \exp(2\pi i\tilde{k}j/L) |\tilde{k}\rangle$). Substituting Eq. (2.10) into Eq. (2.7), we obtain the Hamiltonian in \tilde{k} -space ($|\tilde{k}\rangle$)

as follows:

$$H_{AA} = \sum_{\tilde{k}} \left[-\frac{W}{2J} J(|\tilde{k}\rangle\langle\tilde{k}+1| + |\tilde{k}+1\rangle\langle\tilde{k}|) + \frac{2J}{W} W \cos(2\pi\alpha\tilde{k}) |\tilde{k}\rangle\langle\tilde{k}| \right]. \quad (2.11)$$

Comparing Eq. (2.7) to (2.11), both Hamiltonians exhibit the same structure, and the unitary transformation changes the hopping amplitude from J to $\frac{W}{2J}J$ and the disorder strength from W to $\frac{2J}{W}W$. Since both Hamiltonians include the same delocalization-localization transition point, the hopping amplitude and disorder strength in Eq. (2.7) must become identical to those in Eq. (2.11) at the transition point, i.e., $J = (W/2J)J$ and $W = (2J/W)W$. Let W_c be the critical disorder strength of the Hamiltonian in Eq. (2.7) for a given J . Accordingly $W_c = 2J$. The transition occurs in the local basis ($|j\rangle$) and \tilde{k} -space ($|\tilde{k}\rangle$) simultaneously.

In the previous section we have seen that IPR and MFD are suitable measures for quantifying the extent to which a wave function is localized or delocalized. In Fig. 2.2 we have also visualized localization–delocalization transition in a disordered system. The results illustrated in Fig. 2.1 and Fig. 2.2 are based on the simulation performed for the AA model. As noted in Chapter 2, we cannot observe such localization–delocalization transition in one spatial dimension if the Anderson model with uncorrelated disorder is employed.

2.3 Case of the Hatano–Nelson model: a non-Hermitian extension of quantum mechanics

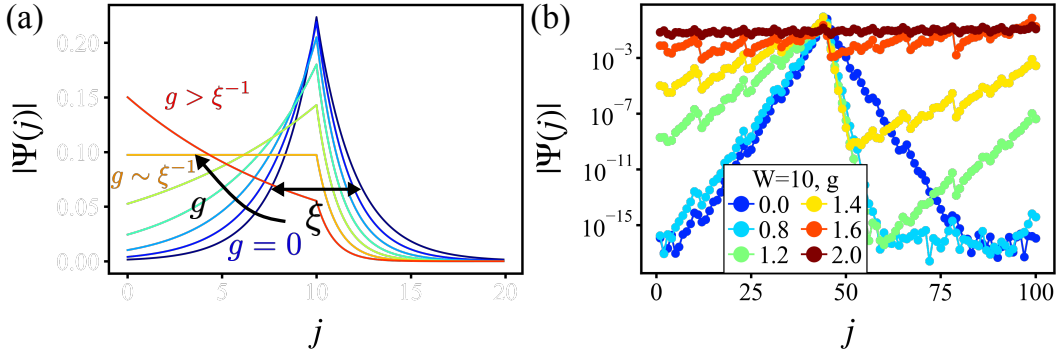


Figure 2.3: Role of the similarity transformation U given in Eq. (2.13), which transforms an eigen wave function $\Psi(j)$ to $\Psi_g(j) = U\Psi(j)$. Panel (a) schematically shows how $|\Psi_g(j)|$ varies with increasing g . Panel (b) shows numerical results of $|\Psi_g(j)|$ for several values of g with a specific disorder configuration for $W = 10$.

Non-Hermitian quantum mechanics has attracted considerable attention in various fields. The Hatano–Nelson (HN) model [33, 34, 54] is one example. Although the HN model was originally introduced to describe the phenomenon of flux-line depinning of the type-II superconductors, this model also entails an interesting implication for a disordered quantum system. In this section, we summarize the basic properties of the HN model and highlight the emergence of

delocalization transition in a disordered quantum system as an exception to the Anderson localization. The Hatano–Nelson model is expressed as follows:

$$H_{ns}(g) = \sum_{j=1}^{L-1} [-J(e^g|j\rangle\langle j+1| + e^{-g}|j+1\rangle\langle j|)] + \sum_{j=1}^L W_j|j\rangle\langle j|, \quad (2.12)$$

where the first two terms are hopping terms with g being a parameter quantifying the degree of non-reciprocity, and the third term is the onsite potential. If $g \neq 0$, the Hamiltonian is non-Hermitian $H \neq H^\dagger$, and thus, the eigenenergy can become a complex number.

To understand the role of g , the following similarity transformation may be introduced:

$$\begin{aligned} U|j\rangle &= e^{-gj}|j\rangle, \\ \langle j|U^{-1} &= e^{gj}\langle j|. \end{aligned} \quad (2.13)$$

Equation (2.13) represents the gauge transformation if g is iA ($A \in \mathbb{R}$). Thus, the similarity transformation is referred to as the imaginary gauge transformation. Using this transformation, we can reduce the non-Hermitian Hamiltonian $H_{ns}(g)$ to the Hermitian Hamiltonian $H_{ns}(0) = U^{-1}H_{ns}(g)U$. This means that the eigenenergies of $H_{ns}(g)$ are real numbers [59]. Additionally, the n th left and right eigenvectors of $H_{ns}(g)$ are expressed as

$$|\Psi_n^R\rangle = U|\Psi_n\rangle, \quad (2.14)$$

and

$$\langle\Psi_n^L| = \langle\Psi_n|U^{-1}, \quad (2.15)$$

respectively, where $|\Psi_n\rangle$ is the n th eigenvector of $H_{ns}(0)$. These results do not apply under the periodic boundary condition (PBC).

Under PBC, Eq. (2.12) transforms $H_{ns}(g)$ as

$$\begin{aligned} U^{-1}H_{ns}(g)U &= \sum_{j=1}^{L-1} [-J(|j\rangle\langle j+1| + |j+1\rangle\langle j|)] + \sum_j^L W_j|j\rangle\langle j| \\ &\quad - J(e^{Lg}|L\rangle\langle 1| + e^{-Lg}|1\rangle\langle L|). \end{aligned} \quad (2.16)$$

The non-Hermiticity of the HN model is described by only the last two hopping terms of Eq. (2.16). In the delocalized phase, these terms dominate the Hamiltonian and generate a complex eigenenergy. However, these terms become unimportant in the localized phase. To verify this, we consider a perturbation of non-reciprocal hopping to the localized eigenstate $|\Psi^0\rangle \sim \sum_j \frac{1}{\sqrt{\xi}} \exp(-\frac{|j-L/2|}{\xi})|j\rangle$,³ where ξ is a localization length of $H_{ns}(0)$. The correction ΔE to an eigenenergy due to the perturbation is expressed as

$$\begin{aligned} \Delta E &= \langle\Psi^0| - J((e^{Lg} - 1)|L\rangle\langle 1| + (e^{-Lg} - 1)|1\rangle\langle L|)|\Psi^0\rangle \\ &\sim -J e^{Lg} \langle\Psi^0|L\rangle\langle 1|\Psi^0\rangle \\ &= -\frac{J}{\xi} e^{Lg} \exp(-\frac{L/2}{\xi}) \exp(-\frac{L/2}{\xi}) \\ &= -\frac{J}{\xi} e^{L(g-\xi^{-1})}. \end{aligned} \quad (2.17)$$

³We assume that the localization center of $|\Psi^0\rangle$ is located at $L/2$.

When $g < \xi^{-1}$, ΔE is exponentially small as per Eq. (2.17) and hence, the eigenenergy remains a real number. Contrastingly, when $g > \xi^{-1}$, Eq. (2.17) shows that ΔE is exponentially large. Note that Eq. (2.17) captures only the magnitude of ΔE . Since the perturbation is non-Hermitian, ΔE should contain an imaginary part. Consequently, the eigenenergy becomes a complex number. These results indicate that the critical value g_c is expressed as follows:

$$g_c = \xi^{-1}. \quad (2.18)$$

Equation (2.18) suggests that the non-Hermiticity enables us to evaluate the localization length. Interestingly, the normalization condition of a localized eigenstate also presents the same condition of the critical value g_c . Under the similarity transformation of Eq. (2.13), a localized eigen wave function⁴ is transformed to

$$\Psi_g(j) \equiv U\Psi(x) \sim \exp\left(\frac{-|x|}{\xi} - gx\right), \quad (2.19)$$

Figure 2.3(a) schematically shows the variation of $\Psi_g(j)$ with increasing g . Until g exceeds g_c , $\Psi_g(j)$ maintains a tendency to localize. The critical value g_c can be determined by the normalization condition of the eigenstate. If $\xi^{-1} > g$, the normalization constant is expressed as follows:

$$\begin{aligned} 1 = C^2 \int_{-\infty}^{\infty} |\Psi_g(x)|^2 dx &\sim C^2 \int_{-\infty}^{\infty} dx \exp\left(2\frac{-|x| - \xi gx}{\xi}\right) \\ &= C^2 \left[\int_0^{\infty} dx + \int_{-\infty}^0 dx \right] \exp\left(2\frac{-|x| - \xi gx}{\xi}\right) \\ &= \tilde{C}^2 \left(\frac{\xi}{2(1 + \xi g)} + \frac{\xi}{2(1 - \xi g)} \right) \\ &= \tilde{C}^2 \frac{\xi}{1 - \xi^2 g^2}, \end{aligned}$$

leading to

$$\tilde{C} = \frac{\sqrt{1 - \xi^2 g^2}}{\sqrt{\xi}}. \quad (2.20)$$

If $\xi^{-1} < g$, the integration diverges, i.e., $\Psi_g(j)$ is not square integrable, indicating that the eigenstate is delocalized. Therefore, critical g_c is expressed as

$$g_c = \xi^{-1}. \quad (2.21)$$

Using Eq. (2.12), we numerically examine the above results. Figure 2.3(b) shows $|\Psi_g(j)|$ as a function of j for various values of g with a specific disorder configuration ($W = 10$). As g increases, the eigenstate changes according to Eq. (2.19), and the eigenstate extends the entire system beyond g_c . In the actual computation, we obtain eigenstates at $g = 0$ and select one eigenstate $|\Psi_{g=0}\rangle$ at random. Next, we calculate eigenstate $|\Psi_g\rangle$ for several values of g . The resulting $|\Psi_g\rangle$'s are plotted in Fig. 2.3(b).

⁴We assume that the localization center of $\Psi(x)$ is located at 0.

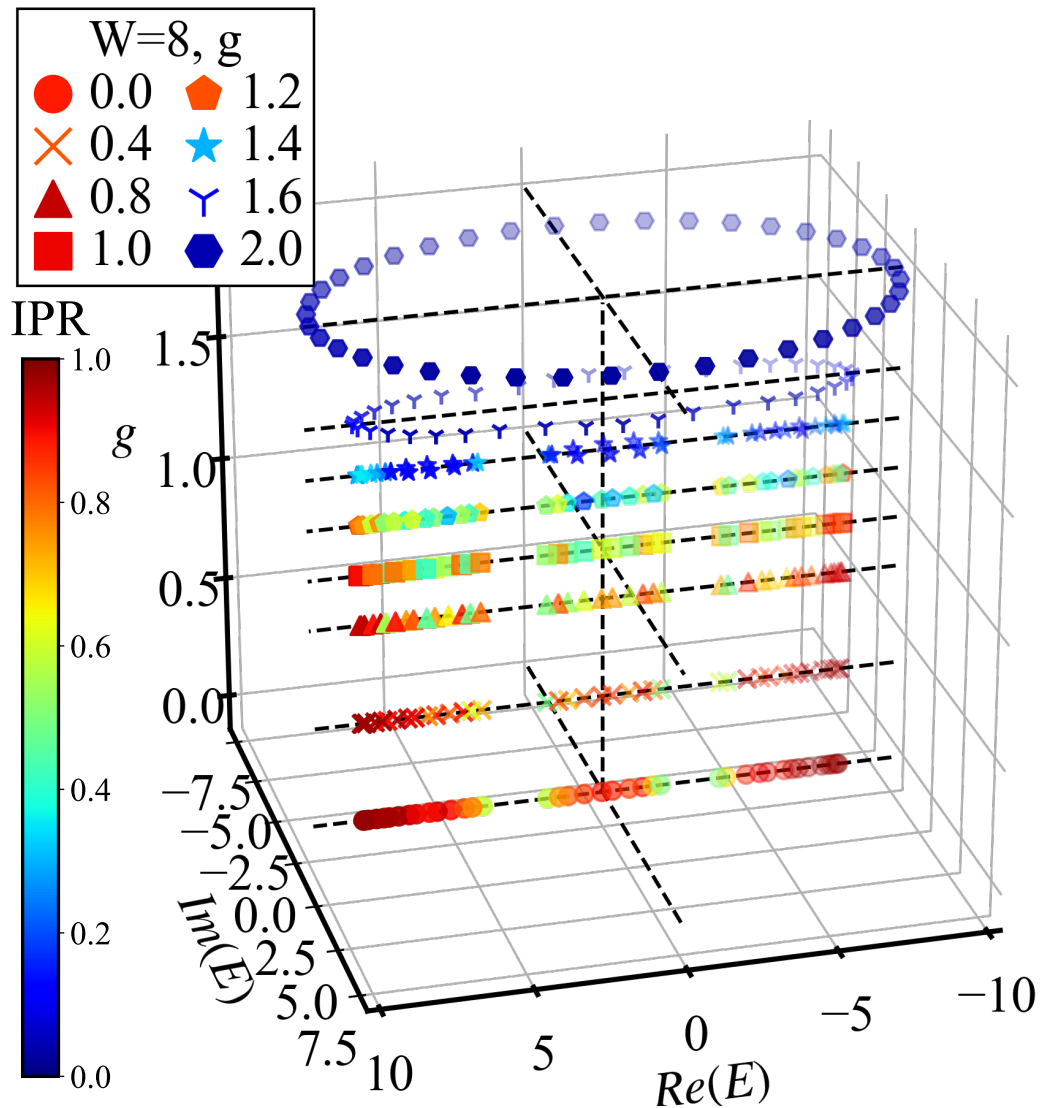


Figure 2.4: Typical behavior of IPR and eigenenergies for several values of g with $L = 100$.

We characterize the delocalization transition due to g by employing IPR and complex spectrum. Figure 2.4 shows complex eigenenergies and IPRs in a complex plane as a function of g . Here, the color map represents values of IPR. When g is small, eigenenergies do not exhibit an imaginary part, and $IPR \sim 1$. As g increases, IPRs gradually decrease reflecting the fact that an eigenstate becomes more extended than that of the $g = 0$ case. Eigenenergies remain real numbers as long as $g < g_c$. Beyond g_c , eigenenergies become complex numbers, and IPRs take small values as $IPR \sim \frac{1}{L}$. These results suggest that the localization–delocalization transition accompanies the real–complex transition.

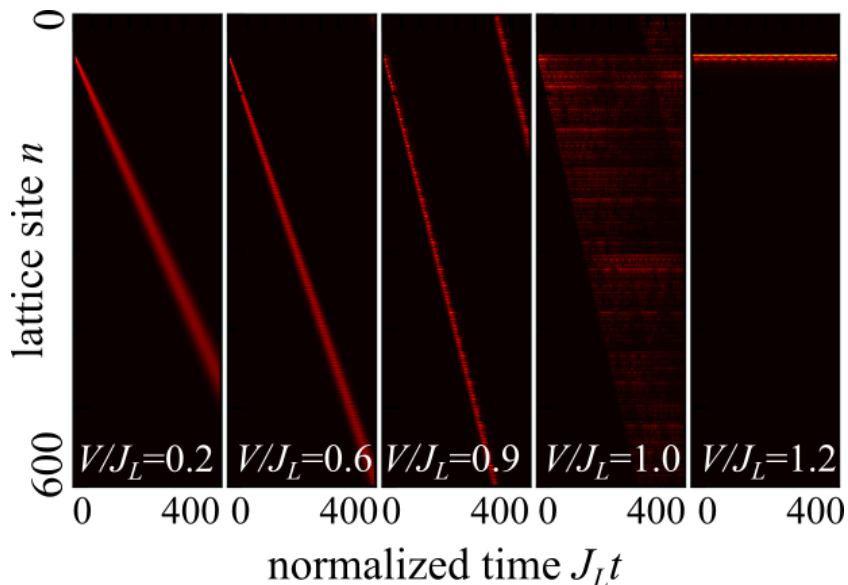


Figure 2.5: Wave packet spreading in the HN model with several values of disorder strength V/J with $J_R = 0$ and $J = J_L = 1$. The behavior of wave packet spreading is qualitatively similar to that reported in Ref. [42].

2.4 Localization/delocalization phenomena from the perspective of wave packet dynamics

Dynamical behavior of the HN model has been studied in Ref. [42]: the author employs a modified version of the HN model expressed as

$$H = \sum_j [-J_R|j+1\rangle\langle j| - J_L|j\rangle\langle j+1| + V \cos(2\pi\alpha j)|j\rangle\langle j|]. \quad (2.22)$$

Eigenstates of H are delocalized as long as $V/J < 1$. Time evolution of a wave packet is shown in Fig. 2.5 for several values of V/J . This figure shows that the wave packet moves in the positive direction (unidirectional motion) when $V/J < 1$ and stops moving when $1 < V/J$. These features indicate that the diffusion constant β , defined as

$$\langle x^2 \rangle = \frac{\sum_j j^2 |\psi_j|^2}{\sum_j |\psi_j|^2} \propto t^\beta, \quad (2.23)$$

takes a positive value when $V/J < 1$ and vanishes when $1 < V/J$. The author of Ref. [42] has mainly focused on the relationship between β and the complex spectrum of the system. Cascade-like spreading of the wave packet near the transition point ($V/J = 1$) is also reported in Ref. [42].

At this stage, an intuitive explanation of unidirectional motion has not been provided. Why does the wave packet show a unidirectional motion against disorder? We will provide an intuitive explanation of the above features in Chapter 4.

Chapter 3

ETH, MBL, and entanglement entropy

In this chapter, we explain ETH, MBL, and its extension to the non-Hermitian case. First, we discuss the thermalization of an isolated many body system and its relationship to ETH. We subsequently introduce a phenomenological view of MBL. We show differences in static and dynamical features of entanglement entropy between ETH and MBL phases. We also discuss differences between AL and MBL phases and discuss why the MBL phase exhibits relaxation behavior in its dynamics. We comment on open problems of the ETH–MBL transition and elucidate why estimating its transition point is difficult. Finally, we summarize the previous study of the many-body HN model and highlight potential problem related to its dynamics.

3.1 Eigenstate thermalization hypothesis (ETH)

In an isolated quantum many-body system, its energy is conserved in the course of time evolution. At equilibrium, the system with certain energy E is described by a microcanonical ensemble:

$$\hat{\rho}_{mic}(E) = \frac{1}{Z_{E,\delta E}} \sum_{|E_N - E| < \delta E} |E_N\rangle\langle E_N|, \quad (3.1)$$

where $|E_N\rangle$ is an eigenstate in the microcanonical energy shell $|E_N - E| < \delta E$, and $Z_{E,\delta E}$ is the number of such eigenstates. Using $\hat{\rho}_{mic}(E)$, the expectation value of an observable \hat{O} in the microcanonical ensemble is expressed as

$$\langle \hat{O} \rangle_{mic} = \text{Tr}(\hat{\rho}_{mic}(E)\hat{O}). \quad (3.2)$$

The expectation value of \hat{O} evolves as

$$\begin{aligned} \langle \hat{O}(t) \rangle &= \langle \Psi(t) | \hat{O} | \Psi(t) \rangle \\ &= \sum_{N,N'} e^{iE_N t} \phi_N^* \langle E_N | \hat{O} | E_{N'} \rangle e^{-iE_{N'} t} \phi_{N'} \\ &= \sum_{N,N'} e^{i(E_N - E_{N'})t} \phi_N^* \phi_{N'} \hat{O}_{N,N'}, \end{aligned} \quad (3.3)$$

where $\phi_N = \langle E_N | \Psi(0) \rangle$ and $\hat{O}_{N,N'} = \langle E_N | \hat{O} | E_{N'} \rangle$. We expect that $\langle \hat{O}(t) \rangle$ approaches the microcanonical ensemble averaged value expressed in Eq. (3.2). As per Eq. (3.3), $\langle \hat{O}(t) \rangle$ oscillates reflecting the phase factor arising from the

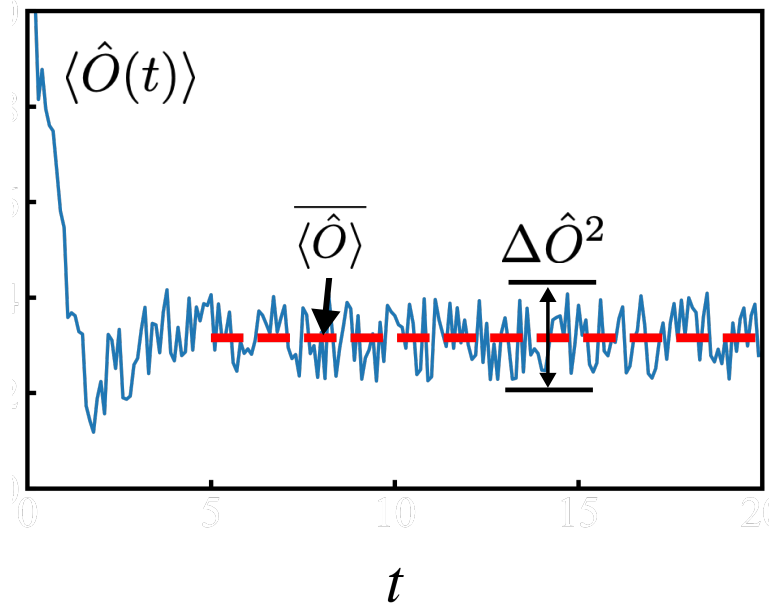


Figure 3.1: Time evolution of $\langle \hat{O}(t) \rangle$ (a schematic picture); the broken redline represents the time average of $\langle \hat{O}(t) \rangle$, and $\Delta \hat{O}^2$ represents the variance of $\langle \hat{O}(t) \rangle$.

time evolution operator. Figure 3.1 shows the behavior of $\langle \hat{O}(t) \rangle$ in a schematic manner.

Considering the thermalization of a given state, we are interested in the statistical behavior of $\langle \hat{O} \rangle$. Thus, we focus on the time average of $\langle \hat{O}(t) \rangle$ defined as

$$\overline{\langle \hat{O} \rangle} = \lim_{T \rightarrow \infty} \frac{1}{T} \int_0^T \langle \Psi(t) | \hat{O} | \Psi(t) \rangle dt. \quad (3.4)$$

Generally, one defines the thermalization in such a manner that $\overline{\langle \hat{O} \rangle}$ becomes equal to $\langle \hat{O} \rangle_{mic}$. This results in $\langle \hat{O}(t) \rangle \sim \langle \hat{O} \rangle_{mic}$ because a quantum state should reach the equilibrium state if it is thermalized. To satisfy the above condition, the variance of $\langle \hat{O}(t) \rangle$ defined as

$$\Delta \hat{O}^2 = \overline{[\langle \hat{O}(t) \rangle - \overline{\langle \hat{O} \rangle}]^2} \quad (3.5)$$

must be small.

In considering the average over t , we assume that E_N and $E_{N'}$ are not degenerate

$$E_N \neq E_{N'} \quad (3.6)$$

and that arbitrary two pairs of eigenstates (N and N' , and N'' and N''') satisfy

$$E_N - E_{N'} \neq E_{N''} - E_{N'''} \quad (3.7)$$

Accordingly we can rewrite Eq. (3.4) as follows:

$$\begin{aligned}
\overline{\langle \hat{O} \rangle} &= \lim_{T \rightarrow \infty} \frac{1}{T} \int_0^T \langle \Psi(t) | \hat{O} | \Psi(t) \rangle dt \\
&= \lim_{T \rightarrow \infty} \frac{1}{T} \int_0^T \sum_{N, N'} e^{i(E_N - E_{N'})t} \phi_N^* \phi_{N'} \hat{O}_{N, N'} \\
&= \sum_N |\phi_N|^2 \hat{O}_{N, N}
\end{aligned} \tag{3.8}$$

and Eq. (3.5) as

$$\begin{aligned}
\Delta \hat{O}^2 &= \overline{[\langle \hat{O}(t) \rangle - \overline{\langle \hat{O}(t) \rangle}]^2} \\
&= \overline{\langle \hat{O} \rangle^2} - [\overline{\langle \hat{O} \rangle}]^2 \\
&= \lim_{T \rightarrow \infty} \frac{1}{T} \int_0^T \sum_{N, N', N'', N'''} [e^{i[(E_N - E_{N'}) + (E_{N''} - E_{N'''})t]} \\
&\quad \times (\phi_N^* \phi_{N'} \phi_{N''}^* \phi_{N'''} \hat{O}_{N, N'} \hat{O}_{N'', N'''})] - [\overline{\langle \hat{O} \rangle}]^2 \\
&= \sum_{N \neq N'} \sum_{N'' \neq N'''} \overline{\phi_N^* \phi_{N'} \phi_{N''}^* \phi_{N'''} \times} \\
&\quad \times e^{i[(E_N - E_{N'}) - (E_{N'''} - E_{N''})t]} \hat{O}_{N, N'} \hat{O}_{N''', N''}^* \\
&= \sum_{N \neq N'} \sum_{N'' \neq N'''} \phi_N^* \phi_{N'} \phi_{N''}^* \phi_{N'''} \\
&\quad \times \delta_{N, N'''} \delta_{N', N''} \hat{O}_{N, N'} \hat{O}_{N''', N''}^* \\
&= \sum_{N \neq N'} |\phi_N|^2 |\phi_{N'}|^2 |\hat{O}_{N, N'}|^2.
\end{aligned} \tag{3.9}$$

One of the promising hypotheses for realization of thermalization is the eigenstate thermalization hypothesis (ETH) that comprises two parts: off-diagonal ETH and diagonal ETH. The off-diagonal ETH assumes that $O_{N, N'} = \langle N | \hat{O} | N' \rangle$ with $N \neq N'$ in the microcanonical energy shell satisfying

$$\lim_{L \rightarrow \infty} O_{N, N'} \rightarrow 0. \tag{3.10}$$

Under the off-diagonal ETH, $\Delta \hat{O}^2$ vanishes in the limit of $L \rightarrow \infty$. This can be expressed as follows:

$$\begin{aligned}
\Delta \hat{O}^2 &= \sum_{N \neq N'} |\phi_N|^2 |\phi_{N'}|^2 |\hat{O}_{N, N'}|^2 \\
&\leq \sum_{N, N'} |\phi_N|^2 |\phi_{N'}|^2 \left| \max_{N \neq N'} \{ |\hat{O}_{N, N'}| \} \right|^2 \\
&\leq \left| \max_{N \neq N'} \{ |\hat{O}_{N, N'}| \} \right|^2 \rightarrow 0.
\end{aligned} \tag{3.11}$$

The diagonal ETH assumes that $O_{N, N} = \langle N | \hat{O} | N \rangle$ in the microcanonical energy shell satisfying

$$\lim_{L \rightarrow \infty} O_{N, N} \rightarrow \langle \hat{O} \rangle_{mic}(E). \tag{3.12}$$

Under the diagonal ETH, $\overline{\langle \hat{O} \rangle} \sim \langle \hat{O} \rangle_{mic}$ is expressed as

$$\begin{aligned} \overline{\langle \hat{O} \rangle} &= \sum_N |\phi_N|^2 \hat{O}_{N,N} \\ &\simeq \sum_N |\phi_N|^2 \langle \hat{O} \rangle_{mic}(E) \\ &= \langle \hat{O} \rangle_{mic}(E). \end{aligned} \quad (3.13)$$

Next, we finally comment on the physical representation of thermalization in a isolated quantum system without a heat bath. A possible interpretation is the occurrence of thermalization as a consequence of entanglement. Let us assume that the system can be divided into two subsystems A and B, and we consider the expectation value of an operator \hat{O}_A that belongs to A. The expectation value is expressed as $\langle \hat{O}_A \times I_B \rangle$, where I_B is the identity operator in B. The expectation value is expressed as follows:

$$\begin{aligned} \langle \Psi(t) | \hat{O}_A \times I_B | \Psi(t) \rangle &= \text{Tr}(\hat{O}_A \times I_B \rho) \\ &= \text{Tr}_A \text{Tr}_B(\hat{O}_A \times I_B \rho) \\ &= \text{Tr}_A(\hat{O}_A \rho_A), \end{aligned} \quad (3.14)$$

where ρ_A in the last line is the reduced density matrix of the subsystem A defined as $\rho_A = \text{Tr}_B\{\rho\}$. If $|\Psi(t)\rangle$ is entangled, the quantum state described by ρ_A becomes a mixed state. One can interpret $\langle \hat{O}_A \times I_B \rangle$ as the expectation value of \hat{O}_A with a statistical distribution ρ_A . This implies that the subsystem B plays the role of a bath for subsystem A [6], leading to the thermalization of A. Conversely, the subsystem A leads to the thermalization of subsystem B.

3.2 Many-body localization (MBL)

Under the ETH, the expectation value of an observable O in an eigenstate of H depends on only its eigenenergy E without large fluctuation. The fluctuation vanishes in the thermodynamic limit. However, in a strongly disordered system, such a quantity fluctuates and does not depend on E [60]. We examine such behavior, employing the Hamiltonian expressed as

$$H = \sum_j \left[\frac{J_{xy}}{2} (S_j^+ S_{j+1}^- + S_{j+1}^+ S_j^-) + J_{zz} S_j^z S_{j+1}^z + W_j S_j^z \right], \quad (3.15)$$

where the first two terms represent exchange interaction, the third term represents Ising interaction, and the last term represents an onsite random magnetic field term with uniform random distribution $W_j \in [-W, W]$. In considering a quantum system, attention is typically focused on the properties of the ground state. Notably, we focus on highly excited states in the studies on ETH–MBL transition. We introduce normalized eigenenergy:

$$\epsilon = \frac{E - \text{Min}(E)}{\text{Max}(E) - \text{Min}(E)}, \quad (3.16)$$

where $\text{Max}(E)$ and $\text{Min}(E)$ are the maximum and minimum eigenenergies, respectively. Figure 3.2 shows $\langle S_{L/2}^z \rangle$ as a function of ϵ at weak ($W = 0.4$) and

strong ($W = 8.0$) disorder strength. In the weak disorder case, $\langle S_{L/2}^z \rangle$ depends on ϵ , and its fluctuation is sufficiently small in the middle of the spectrum. These tendencies become more apparent as the system size increases [60]. In the strong disorder case, $\langle S_{L/2}^z \rangle$ is independent of ϵ , and its fluctuation is considerably large. That is, ETH does not hold. This failure of ETH stems from the many-body

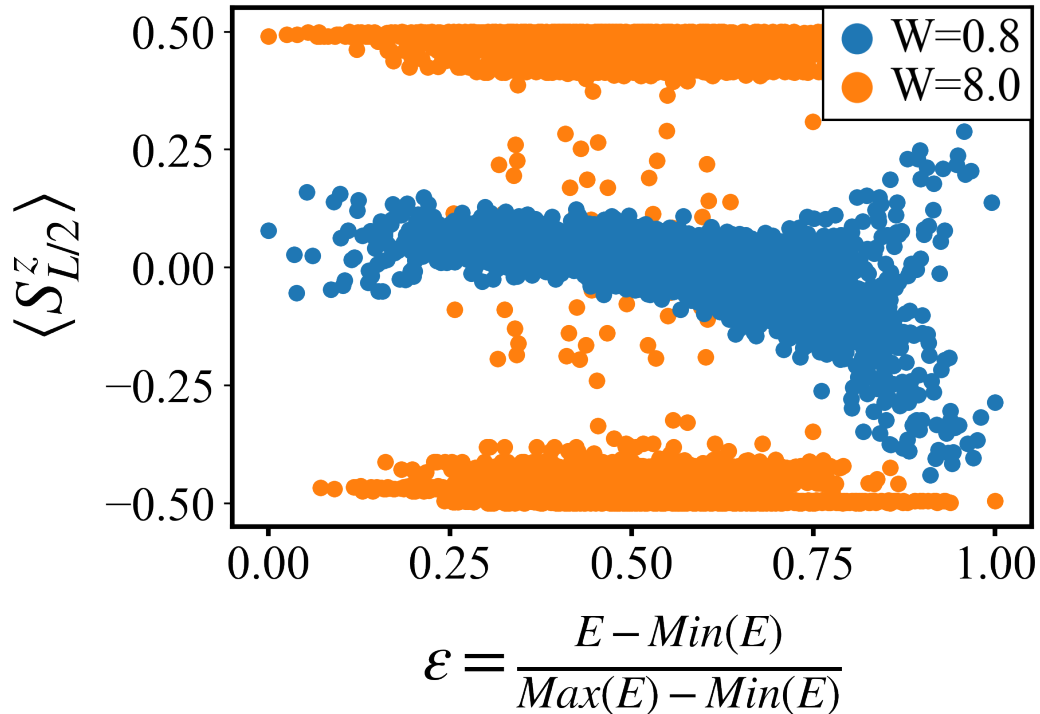


Figure 3.2: Expectation value $\langle S_{L/2}^z \rangle$ as a function of ϵ , where $L = 14$, $J_{xy} = 1$, and $J_{zz} = 1$ with a specific disorder configuration. We consider the zero magnetization sector $\sum_j S_j^z = 0$.

localization (MBL), which is intrinsic to a quantum many-body system. An eigenstate of the MBL phase localizes in the Fock space [61, 62, 63, 43] and typically involves localization in real space [64] as well. Here, the localization in real space means that the system is separated into several domains: $\langle S_j^z \rangle \sim \frac{1}{2}$ in certain domains and $\langle S_j^z \rangle \sim -\frac{1}{2}$ in others. This localization behavior is shown in Fig. 3.2 in the strong disorder case of $W = 8.0$. The authors of Refs. [22, 65] have suggested that an ideal MBL phase is described by a phenomenological Hamiltonian that is expressed as

$$H_{MBL} = E_0 + \sum_j h_j \tau_j^z + \sum_{j,k} J_{j,k} \tau_j^z \tau_k^z + \sum_{j,k,l} J_{j,k,l} \tau_j^z \tau_k^z \tau_l^z + \dots, \quad (3.17)$$

where E_0 is a constant value, and τ_i^z is a locally conserved quantity called a local integral of motion (LIOM). Equation (3.17) has been justified for a certain class of spin chains [66]. LIOM's are operator which exponentially localize in Fock space and are expressed as

$$\tau_i^z = \sum_{i_1} \sum_{\alpha=x,y,z} a_{i_1}^\alpha \sigma_x^\alpha / \sqrt{\xi} + \sum_{i_1, i_2} \sum_{\alpha, \beta=x,y,z} b_{i_1, i_2}^{\alpha, \beta} \sigma_{i_1}^\alpha \sigma_{i_2}^\beta + \dots, \quad (3.18)$$

where ξ is the localization length, i_k denotes the k th localization center, and $a_{i_1}^\alpha$ and $b_{i_1, i_2}^{\alpha, \beta}$ are proportional to $e^{-|i-i_1|/\xi}$ and $e^{-(|i-i_1|+|i-i_2|)/\xi}$, respectively [67, 68, 69]. Hamiltonian (3.17) incorporates only the terms with τ_j^z 's and therefore commutes with τ_j^z :

$$[H_{MBL}, \tau_j^z] = 0. \quad (3.19)$$

This means that each τ_j^z is a conserved quantity [22, 65], and the ideal MBL phase can be regarded as an integrable system [8, 65]. LIOMs act as constraint in the quench dynamics without particle transport under the breaking of ETH [68, 69]. The existence of such operators explains the relaxation behavior of observables and entanglement entropy [22, 70], which we discuss in Section 3.5.

3.3 Quantum entanglement and entanglement entropy

3.3.1 General definition of the entanglement

Let us introduce Fock basis $|\{n\}\rangle \equiv |n_1 n_2 \cdots n_{L-1} n_L\rangle$, where n_j ($j = 1, 2, \dots, L$) denotes the number of electrons in the j th orbital ¹. One can describe a general many-body quantum state $|\Psi\rangle$ as a superposition of basis states corresponding to different particle configurations with many-body coefficients $\psi_{\{n\}}$:

$$|\Psi\rangle = \sum_{\{n\}} \psi_{\{n\}} |\{n\}\rangle. \quad (3.20)$$

Here, we divide the system of length L into two subsystems A and B of length $L/2$, where A consists of the sites with $j \in j_A = \{1, 2, \dots, L/2\}$, while B consists of the sites with $j \in j_B = \{L/2 + 1, L/2 + 2, \dots, L\}$. By tracing out subsystem B , we calculate the entanglement entropy S_{tot} for subsystem A . To concretize this procedure, we employ the density matrix Ω ,

$$\begin{aligned} \Omega &= |\Psi\rangle\langle\Psi| \\ &= \sum_{\{n\}, \{n'\}} \psi_{\{n\}} \psi_{\{n'\}}^* |\{n\}\rangle\langle\{n'\}| \\ &= \sum_{\{n_A\}, \{n_B\}, \{n'_A\}, \{n'_B\}} \psi_{\{n_A\}, \{n_B\}} \psi_{\{n'_A\}, \{n'_B\}}^* |\{n_A\}\rangle\langle\{n'_A\}| \langle\{n_B\}| \langle\{n'_B\}|, \end{aligned} \quad (3.21)$$

where $\{n_A\} = n_1, n_2, \dots, n_{L/2}$ and $\{n_B\} = n_{L/2+1}, \dots, n_L$ ². We perform partial trace over $\{n_B\}$:

$$\begin{aligned} \Omega_A &= \text{Tr}_B \Omega \\ &= \sum_{\{n'_B\}} \langle\{n'_B\}| \Omega |\{n'_B\}\rangle \\ &= \sum_{\{n_A\}, \{n'_A\}, \{n_B\}} \psi_{\{n_A\}, \{n_B\}} \psi_{\{n'_A\}, \{n_B\}}^* |\{n_A\}\rangle\langle\{n'_A\}|. \end{aligned} \quad (3.22)$$

¹For a spin 1/2 system, $n_i = 0$ and $n_i = 1$ is interpreted as \downarrow_i and \uparrow_i , respectively. Additionally, $\{n\}$ corresponds to the configuration of spins in real space.

²Here, $\psi_{\{n\}} \equiv \psi_{\{n_A\}, \{n_B\}}$ and $|\{n\}\rangle \equiv |\{n_A\}\rangle |\{n_B\}\rangle$.

The entanglement entropy is defined as

$$S_{\text{tot}} = -\text{Tr} \Omega_A \log \Omega_A, \quad (3.23)$$

which is written in terms of the eigenvalues λ_α of the reduced density matrix Ω_A as

$$S_{\text{tot}} = -\sum_{\alpha} \lambda_{\alpha} \log \lambda_{\alpha}. \quad (3.24)$$

3.3.2 Two types of contributions to the entanglement entropy: number and configuration entropies

- Color representation of the basis

$$|ij\rangle_A |kl\rangle_B \quad N_A \equiv i + j, N_B \equiv k + l$$

$$N_A = 0, N_B = 2 \quad \color{red}{\square} \quad N_A = 1, N_B = 1 \quad \color{blue}{\square} \quad N_A = 2, N_B = 0 \quad \color{green}{\square}$$

- Quantum state

$$\begin{aligned} |\Psi\rangle = & \psi_1 \color{red}{|00\rangle_A |11\rangle_B} + \psi_2 \color{blue}{|01\rangle_A |01\rangle_B} + \psi_3 \color{blue}{|01\rangle_A |10\rangle_B} \\ & + \psi_4 \color{blue}{|10\rangle_A |01\rangle_B} + \psi_5 \color{blue}{|10\rangle_A |10\rangle_B} + \psi_6 \color{green}{|11\rangle_A |00\rangle_B} \end{aligned}$$

- Reduced density matrix

$$\Omega_A = \text{Tr}_B (|\Psi\rangle\langle\Psi|)$$

Constructing the density matrix and tracing over the degree of freedom of the subsystem B

$$\begin{aligned} = & |\psi_1|^2 \color{red}{|00\rangle_{AA}\langle 00|} + |\psi_6|^2 \color{green}{|11\rangle_{AA}\langle 11|} \\ & + (|\psi_2|^2 + |\psi_3|^2) \color{blue}{|01\rangle_{AA}\langle 01|} + (\psi_2\psi_4^* + \psi_3\psi_5^*) \color{blue}{|01\rangle_{AA}\langle 10|} \\ & + (\psi_2^*\psi_4 + \psi_3^*\psi_5) \color{blue}{|10\rangle_{AA}\langle 01|} + (|\psi_4|^2 + |\psi_5|^2) \color{blue}{|10\rangle_{AA}\langle 10|} \end{aligned}$$

Matrix representation

$$\Omega_A = \begin{pmatrix} \color{red}{|\psi_1|^2} & 0 & 0 & 0 \\ 0 & \color{blue}{|\psi_2|^2 + |\psi_3|^2} & \color{blue}{\psi_2\psi_4^* + \psi_3\psi_5^*} & 0 \\ 0 & \color{blue}{\psi_2^*\psi_4 + \psi_3^*\psi_5} & \color{blue}{|\psi_4|^2 + |\psi_5|^2} & 0 \\ 0 & 0 & 0 & \color{green}{|\psi_6|^2} \end{pmatrix}$$

Figure 3.3: Schematic derivation of the reduced density matrix from a given quantum state in the system with four sites at half filling.

We consider that a quantum state $|\Psi\rangle$ is described by a superposition of the Fock bases $|\{n\}\rangle = |\{n_A\}\rangle|\{n_B\}\rangle$. We assume that the total number of particles is $\frac{L}{2}$ that is half of the total number of sites (i.e., half filling). The number of particles in $|\{n_A\}\rangle$ defined as

$$N_A \equiv \sum_{j \in j_A} n_j \quad (3.25)$$

relates to that in $|\{n_B\}\rangle$ defined as

$$N_B \equiv \sum_{j \in j_B} n_j, \quad (3.26)$$

since they satisfy the half filling condition: $N_A + N_B = \frac{L}{2}$. The vector space \mathcal{H}_A spanned by $|\{n_A\}\rangle$'s can be decomposed into subspaces specified by $N_A \in \{0, 1, \dots, \frac{L}{2}\}$. The vector space \mathcal{H}_B spanned by $|\{n_B\}\rangle$'s can also be decomposed into subspaces specified by $N_B \in \{0, 1, \dots, \frac{L}{2}\}$. Under the constraint of $N_A + N_B = \frac{L}{2}$, the subspace of \mathcal{H}_A with $N_A = j$ is paired with the subspace of \mathcal{H}_B with $N_B = \frac{L}{2} - j$. Indeed, the density matrix includes non-zero components only in such paired subspaces, which are mutually isolated in the full vector space. Reflecting this isolated structure, the reduced density matrix is expressed in a block diagonal form, as can be observed in Fig. 3.3. Here, each block corresponds to a subspace of \mathcal{H}_A and the total number of the blocks is $L/2 + 1$. The reduced density matrix is expressed as follows:

$$\Omega_A = \Omega_{N_0} \oplus \Omega_{N_1} \oplus \dots \oplus \Omega_{N_{\frac{L}{2}-1}} \oplus \Omega_{N_{\frac{L}{2}}}, \quad (3.27)$$

where Ω_{N_j} describes the subspace specified by $N_A = j$ (cf. Fig. 3.3). Using the block diagonal representation of Ω_A , we can rewrite Eq. (3.23) as

$$\begin{aligned} S_{\text{tot}} &= -\text{Tr} [\Omega_A \log \Omega_A] \\ &= -\sum_{j=0}^{L/2} [\text{Tr} \{ \Omega_{N_j} \log \Omega_{N_j} \}] \\ &= -\sum_{j=0}^{L/2} \sum_{\alpha=1}^{\dim(\Omega_{N_j})} \lambda_{\alpha}^{(N_j)} \log \lambda_{\alpha}^{(N_j)}, \end{aligned} \quad (3.28)$$

where $\lambda_{\alpha}^{(N_j)}$ is the α th eigenvalue of Ω_{N_j} , and $\dim(\Omega_{N_j})$ is the dimension of Ω_{N_j} . We define p_{N_j} as

$$p_{N_j} = \sum_{\alpha} \lambda_{\alpha}^{(N_j)}, \quad (3.29)$$

and $\tilde{\lambda}_{\alpha}^{(N_j)}$ as

$$\tilde{\lambda}_{\alpha}^{(N_j)} = \frac{1}{p_{N_j}} \lambda_{\alpha}^{(N_j)}. \quad (3.30)$$

The contributions to the entanglement entropy S_{tot} can be divided into two parts: the number and configuration entropies (S_{num} and S_{conf}) [71]:

$$\begin{aligned} S_{\text{tot}} &= -\sum_{j=0}^{L/2} \sum_{\alpha=1}^{\dim(\Omega_{N_j})} \lambda_{\alpha}^{(N_j)} \log \lambda_{\alpha}^{(N_j)} \\ &= -\sum_{j=0}^{L/2} \sum_{\alpha=1}^{\dim(\Omega_{N_j})} p_{N_j} \tilde{\lambda}_{\alpha}^{(N_j)} (\log p_{N_j} + \log \tilde{\lambda}_{\alpha}^{(N_j)}) \\ &= -\sum_{j=0}^{L/2} p_{N_j} \log p_{N_j} - \sum_{j=0}^{L/2} \sum_{\alpha=1}^{\dim(\Omega_{N_j})} p_{N_j} \tilde{\lambda}_{\alpha}^{(N_j)} \log \tilde{\lambda}_{\alpha}^{(N_j)} \\ &= S_{\text{num}} + S_{\text{conf}}, \end{aligned} \quad (3.31)$$

where

$$S_{\text{num}} = - \sum_{j=0}^{L/2} p_{N_j} \log p_{N_j}, \quad (3.32)$$

$$S_{\text{conf}} = - \sum_{j=0}^{L/2} \sum_{\alpha=1}^{\dim(\Omega_{N_j})} p_{N_j} \tilde{\lambda}_{\alpha}^{(N_j)} \log \tilde{\lambda}_{\alpha}^{(N_j)}. \quad (3.33)$$

Let us consider the properties of S_{num} and S_{conf} . The number entropy S_{num} is essentially the Shannon entropy of p_{N_j} , which is a probability that one observes N_j particles in the subsystem A; therefore, S_{num} quantifies the fluctuation of the number of particles in the subsystem A. Particle transport generates this type of entropy; i.e., S_{num} is controlled by a local process. The configuration entropy S_{conf} arises from non-local correlations in the many-body state that are intrinsic to a many-body state. In contrast to p_{N_j} , $\tilde{\lambda}_{\alpha}^{(N_j)}$ can change without particle transport, indicating that non-particle transport (i.e., evolution of non-local correlations) can generate S_{conf} in a many-body localized state.

3.4 Static and dynamical properties of the ETH and MBL phases

3.4.1 Static property of S_{tot} in the ETH and MBL phases

The authors of Ref. [16] have reported on the characteristic scaling transition of S_{tot} . They have studied S_{tot} in the random field spin 1/2 XXZ model, which is the same as Eq. (3.15), employing a sophisticated exact diagonalization method. The definition of S_{tot} is the same as Eq. (3.24) (cf. Sec. 3.3). The behavior of S_{tot} shown in Fig. 3.4 is qualitatively similar to that reported in Ref. [16]. The top panel of Fig. 3.4 show S_{tot}/L as a function of L for various values of disorder strength h . In the weakly disordered regime of $h \sim 1$, S_{tot}/L takes a constant value for large L , which implies the volume-law scaling of entanglement entropy $S_{\text{tot}} \propto L$. This behavior is consistent with the view that the system is in the ETH phase, where an eigenstate is thermalized and yields the volume-law scaling of entanglement entropy. In the strongly disordered regime of $h \sim 4$, S_{tot}/L decreases as L increases, which implies the area-law scaling of entanglement entropy $S_{\text{tot}} \sim \text{const}$. This behavior is consistent with the view that the system is in the MBL phase, where a localized eigenstate only generates an entanglement when the localization length exceeds the subsystem size.

They have estimated this volume-to-area law scaling transition point and the exponent of entanglement entropy, employing finite size scaling. Additionally, they have attempted to conduct finite size scaling of the variance of S_{tot} . The variance of S_{tot} , shown in the bottom panel of Fig. 3.4, can be interpreted as specific heat if S_{tot} acts as a thermodynamic entropy. Notably, the actual phase transition point and exponent remain unaddressed problems; indeed, such a transition has recently been regarded as a Kosterlitz–Thouless-like transition. One of the possible directions for a more detailed analysis of this transition is to calculate S_{tot} in a quantum many-body system whose system size is larger than that of the previous study. Unfavorably, the Hilbert space of a many-body system exponentially increases as a function of system size L , and thus,

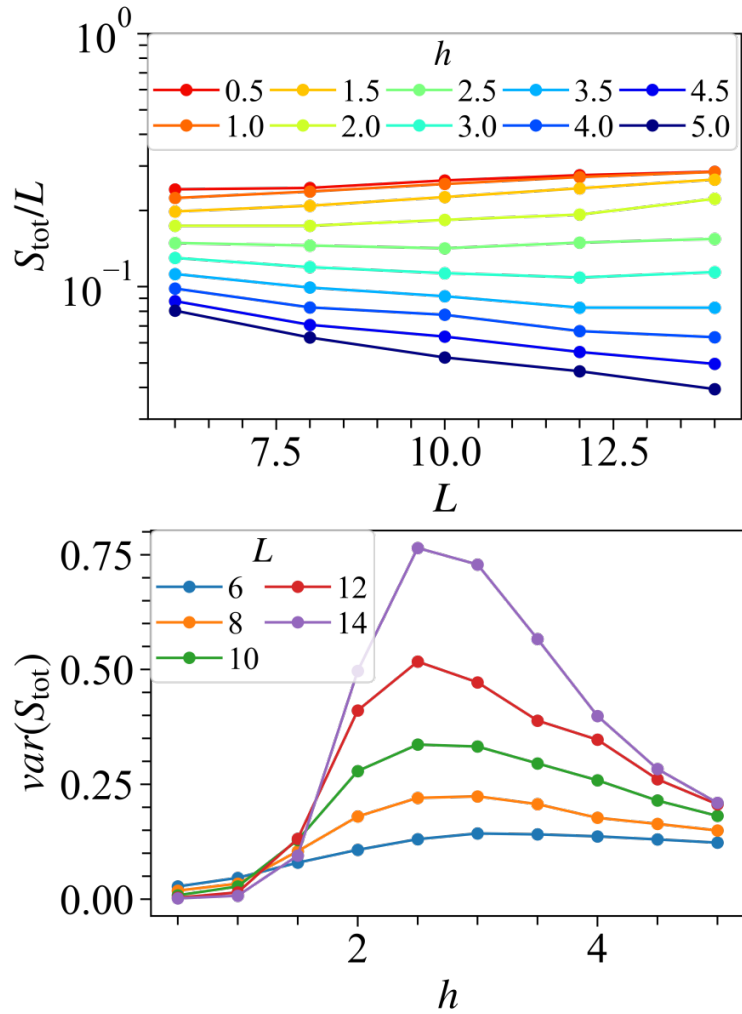


Figure 3.4: Scaling of S_{tot} in the case of $\epsilon = 0.5$: top panel; S_{tot}/L as a function of L , bottom panel; variance of S_{tot} as a function of h . We focus on the zero magnetization sector $\sum_j S_j^z = 0$ as in Ref. [16].

calculating S_{tot} in a large system size is a challenging problem. The tensor network method is one of the methods that has addressed such an inevitable problem and thus has attracted considerable attention recently.

3.4.2 Dynamical property of the ETH and MBL phases: Imbalance and S_{tot}

The authors of Ref. [72] have reported on the characteristic dynamical behavior in a disordered quantum many-body system. They have studied the random field spin 1/2 XXZ model [Eq. (3.15)], employing a sophisticated tensor network method. In the study of the time evolution of a many-body quantum system, the tensor-network method enables treating the system size up to $L = 100$, which is considerably larger than $L \leq 28$ that can be treated by an exact diagonalization method.

Imbalance I is often employed to characterize the ETH-MBL transition point.

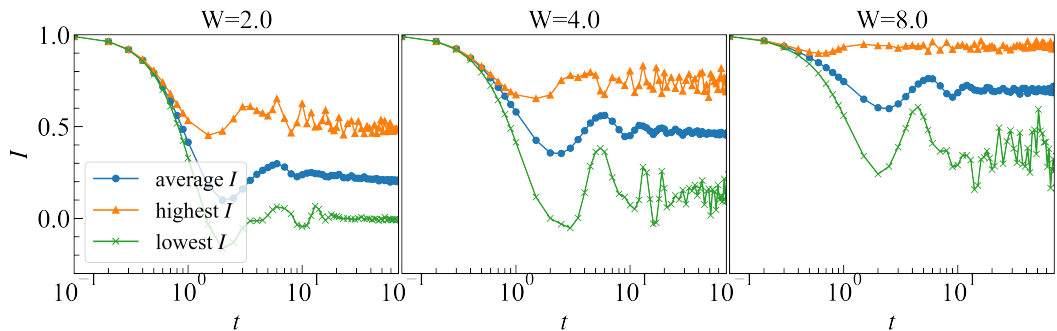


Figure 3.5: Imbalance as a function of time: left, middle, and right panels show the $W = 2, 4,$ and 8 cases with chain length $L = 18$. We focus on the zero magnetization sector $\sum_j S_j^z = 0$ as in Ref. [72].

I is defined by

$$I = \frac{4}{L} \sum_j \langle \Psi(0) | S_j^z | \Psi(0) \rangle \langle \Psi(t) | S_j^z | \Psi(t) \rangle, \quad (3.34)$$

where $|\Psi(0)\rangle$ is an initial state, and $|\Psi(t)\rangle = e^{-iHt}|\Psi(0)\rangle$. This quantity characterizes the time period for which the quantum state memorizes an initial state after time evolution. In the delocalized phase, an initially provided spin pattern melts with increasing time, and I becomes 0. While in the localized phase, an initially provided spin pattern persists, and I becomes finite. Figure 3.5 shows the Imbalance I as a function of time obtained by an exact diagonalization method. The behavior of I is qualitatively similar to that reported in Ref. [72]. They employed the Néel state $|\Psi(t=0)\rangle = |\uparrow\downarrow\uparrow\downarrow \dots\rangle$ as an initial state. In the weakly disordered regime (left panel of Fig. 3.5), I reaches 0 as time evolves, which implies thermalization of the quantum many-body system. As the disorder increases (middle panel of Fig. 3.5), I becomes finite, and in the strongly disordered regime (right panel of Fig. 3.5), I does not decrease, implying that the system localizes.

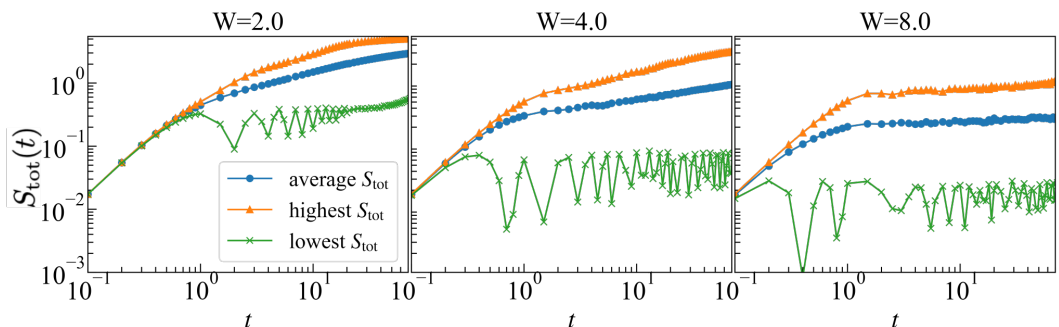


Figure 3.6: $S_{\text{tot}}(t)$ as a function of time: left, middle, and right panels show the $W = 2, 4,$ and 8 cases with chain length $L = 18$. We focus on the zero magnetization sector $\sum_j S_j^z = 0$ as in Ref. [72].

Entanglement entropy also characterizes the dynamical behavior of both the ETH and MBL phases. Figure 3.6 shows $S_{\text{tot}}(t)$ as a function of time obtained

by using an exact diagonalization method. The definition of S_{tot} is the same as Eq. (3.24) (cf. Section 3.3). The behavior of $S_{\text{tot}}(t)$ is qualitatively similar to that reported in Ref. [72]. In a weakly disordered regime (left panel of Fig. 3.6), S_{tot} exhibits a power-law growth $S_{\text{tot}} \propto t^\beta$. As the disorder strength W increases (middle panel of Fig. 3.6), an exponent β gradually decreases (i.e., S_{tot} decreases). This decrease in β is consistent with the behavior of I , which characterizes a relaxation time of a quantum many-body system. As disorder strength W increases, the relaxation time duration of such a system increase, leading to potential divergence in the MBL phase. However, in a strongly disordered regime (right panel of Fig. 3.6), S_{tot} still shows a logarithmic growth in time evolution, although I does not decrease, i.e., without particle transport. This slow logarithmic growth of entanglement entropy stems from dephasing, (discussed in Section 3.5) and characterizes the MBL phase.

We have seen that the entanglement entropy characterizes the dynamical behavior of both ETH and MBL phases. However, this quantity is unsuitable for estimating the ETH–MBL transition because one cannot distinguish between a logarithmic growth and an extremely slow power-law growth of S_{tot} . Additionally, the saturation value of S_{tot} obeys the volume law in both ETH and MBL phases, i.e., the non-scaling transition of entanglement entropy. Unfavorably, I is also unsuitable for estimating the ETH–MBL transition because its saturation value cannot be calculated. Using the tensor network method, we can study a quantum many-body system for large system sizes, but cannot evaluate a sufficient long-time scale. Therefore, estimating the ETH–MBL transition point requires a quantity or method which enables estimation of such a transition point from behavior in a finite time.

3.5 Slow logarithmic growth of entanglement entropy in the MBL phase

The static properties of the MBL phase, characterized by IPR, gap ratio, and S_{tot} , show qualitatively similar behavior to the AL phase. Here an obvious question arises: does interaction cause any difference between the AL and MBL phases? The answer is Yes. The dynamical properties of the MBL phase is qualitatively different from those in the AL phase.

The authors in Refs. [20, 21] have examined the dynamical behavior of S_{tot} in the AL and MBL phases. The top panel of Fig. 3.7 shows S_{tot} as a function of time in a strongly disordered regime. In contrast to the non-interacting case (AL case), S_{tot} exhibits a slow logarithmic growth in the case including interaction. Additionally, the saturation value of S_{tot} shown in the bottom panel of Fig. 3.7 exhibits a volume law in the interacting cases, which is different from the AL case showing area law.

Based on Ref. [22], we consider a two-particle system as a simple example to examine the effect of interaction on S_{tot} . We consider the conventional Hamiltonian with open boundary condition expressed as

$$H = \sum_j [-J(c_j^\dagger c_{j+1} + c_{j+1}^\dagger c_j) + W_j n_j + V n_j n_{j+1}], \quad (3.35)$$

where c_j^\dagger (c_j) creates (annihilates) a fermion at site j , while $\hat{n}_j = c_j^\dagger c_j$ counts the

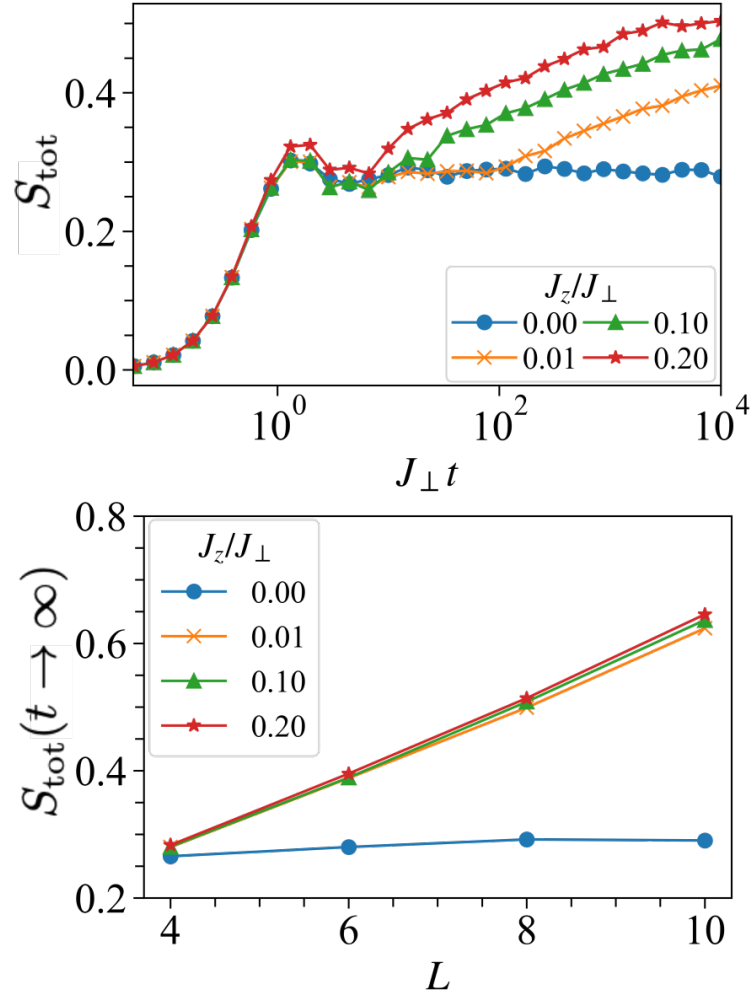


Figure 3.7: Quench dynamics of S_{tot} in the strongly disordered regime. Top panel represents S_{tot} as a function of a normalized time, where J_{\perp} is the strength of exchange interaction and J_z is the strength of Ising interaction. Bottom panel represents the saturation value of S_{tot} as a function of system size L .

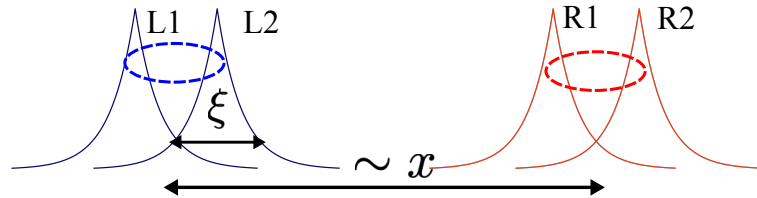


Figure 3.8: Schematic of the initial state [Eq. (3.36)].

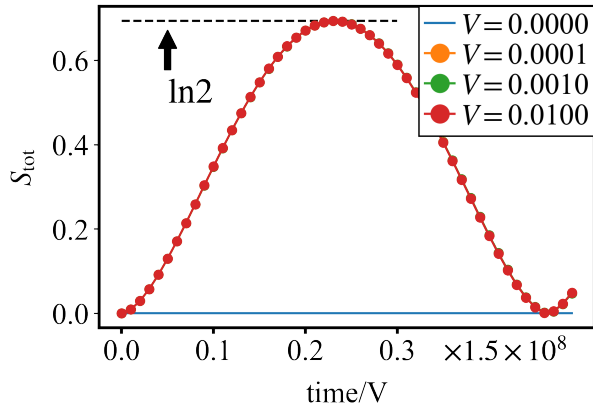


Figure 3.9: Time evolution of S_{tot} with various disorder strengths with $L = 10$ and $J = 1$, and W_j 's are uniformly distributed in $[-6, 6]$.

number n_j of fermions at site j . Even if the interaction is sufficiently weak, a logarithmic growth of S_{tot} emerges, and thus we consider the weak interaction $V \ll J$ and strong disorder $W \gg J$ limit. In the non-interacting limit of $V = 0$, we introduce two eigenstates localized near the left end of the system. Their eigenenergies are expressed as ϵ_{L_i} ($i = 1, 2$), where i is used to specify the two states. We also introduce two eigenstates localized near the right end with ϵ_{R_i} ($i = 1, 2$). Let $c_{L_i}^\dagger$ and $c_{R_i}^\dagger$ ($i = 1, 2$) be the creation operators of the eigenstates localized near the left and right ends, respectively. Let us consider the time evolution of an initial state defined as

$$|\Psi(t=0)\rangle = \frac{1}{2}(c_{L_1}^\dagger + c_{L_2}^\dagger)(c_{R_1}^\dagger + c_{R_2}^\dagger)|0\rangle. \quad (3.36)$$

A schematic of the initial state is shown in Fig. 3.8. The energy of this state is expressed as

$$E_{\alpha,\beta} = \epsilon_\alpha + \epsilon_\beta + \delta E_{\alpha,\beta}, \quad (3.37)$$

where $\alpha \in \{L_1, L_2\}$, $\beta \in \{R_1, R_2\}$, and $\delta E_{\alpha,\beta}$ represents the correction arising from the interaction term with V . If only the first order correction with respect to the interaction is considered,

$$\delta E_{\alpha,\beta} \sim C_{\alpha,\beta} V \exp\left(\frac{-|x_\alpha - x_\beta|}{2\xi}\right), \quad (3.38)$$

where x_α and x_β represent the localization centers of the states specified by α and β , respectively, ξ is a localization length, and $C_{\alpha,\beta}$ is a constant that is not significant in the following argument. Since $V \ll J$ is assumed, the time evolution of the state is expressed as

$$|\Psi(t)\rangle = \frac{1}{2} \sum_{\alpha \in L_1, L_2 \text{ and } \beta \in R_1, R_2} \exp(-iE_{\alpha,\beta}t) |\alpha, \beta\rangle, \quad (3.39)$$

where $|\alpha, \beta\rangle = |\alpha\rangle|\beta\rangle$ with $|\alpha\rangle = c_\alpha^\dagger|0\rangle$ and $|\beta\rangle = c_\beta^\dagger|0\rangle$. To define S_{tot} in this case, we introduce the reduced density matrix

$$\rho_L = \sum_{\beta \in R_1, R_2} \langle \beta | \Psi(t) \rangle \langle \Psi(t) | \beta \rangle, \quad (3.40)$$

which is expressed as

$$\rho_L = \frac{1}{2} \begin{pmatrix} 1 & F(t)/2 \\ F^*(t)/2 & 1 \end{pmatrix}, \quad (3.41)$$

where $F(t) = e^{-i\omega t}(1 + e^{-i\delta\omega t})$, $\delta\omega = \delta E_{L_1, R_2} - \delta E_{L_2, R_2} + \delta E_{L_1, R_1} + \delta E_{L_2, R_1}$, and $\omega = \epsilon_{L_1} + \epsilon_{L_2} + \delta E_{L_1, R_1} - \delta E_{L_2, R_1}$. Let $\lambda_1(t)$ and $\lambda_2(t)$ be the eigenvalues of ρ_L , in terms of which we define S_{tot} as

$$S_{\text{tot}} = - \sum_{i=1,2} \lambda_i(t) \ln \lambda_i(t). \quad (3.42)$$

When $t \sim 0$, $S_{\text{tot}} \sim 0$, since the eigenvalues are 0 and 1. When $t \sim T = \frac{\pi}{\delta\omega} \sim \frac{1}{2V} e^{x/\xi}$, $S_{\text{tot}} \sim \ln 2$, since both eigenvalues are $\frac{1}{2}$.

Using Eq. (3.35), we numerically examine the above results in an initial state that is compatible with Eq. (3.36). Figure 3.9 shows S_{tot} as a function of time/ V with various strengths of V . Except for the case of $V = 0$, S_{tot} gradually increases with time, and takes the maximal value $\ln 2$, which is consistent with the perturbation analysis discussed above.

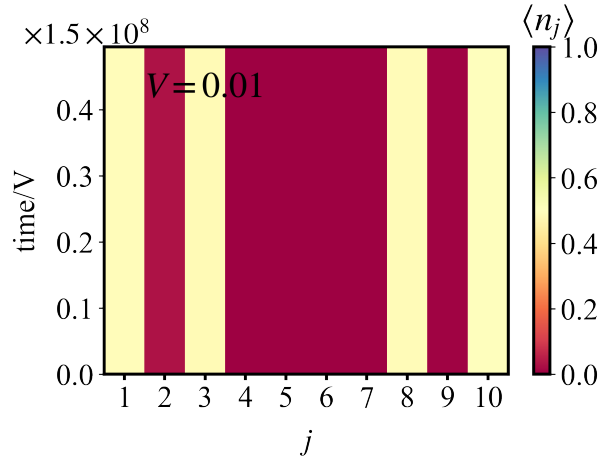


Figure 3.10: Time evolution of the density $\langle n_j \rangle$ as a function of time/ V . We employ the same data used to draw Fig. 3.9.

Note that $\langle n_j(t) \rangle$ exhibits localization tendency in dynamics as shown in Fig. 3.10, which suggests that a non-particle transport generates S_{tot} . Employing the same data used to draw Fig. 3.10, we compare S_{tot} , S_{num} , and S_{conf} in Fig. 3.11 and observe that S_{conf} dominates S_{num} , i.e., $S_{\text{tot}} \sim S_{\text{conf}}$.

The perturbation analysis tells us that the growth of S_{conf} is ascribed to the suppression of the off-diagonal elements of ρ_L caused by the small corrections of ϵ_α and ϵ_β due to interaction. If the number of particles included in the initial state increases, the suppression of the off-diagonal terms due to the interaction is more pronounced. Now, let us focus on the fact that any off-diagonal element consists of many components, each of which shows complicated time evolution due to interaction. Hence any off-diagonal element decreases in time owing to the distractive interference among the many components. This phenomenon is referred to as dephasing. The perturbation analysis shows that a pair of particles suppresses the off-diagonal elements of ρ_L , contributing to the growth of S_{tot} ,

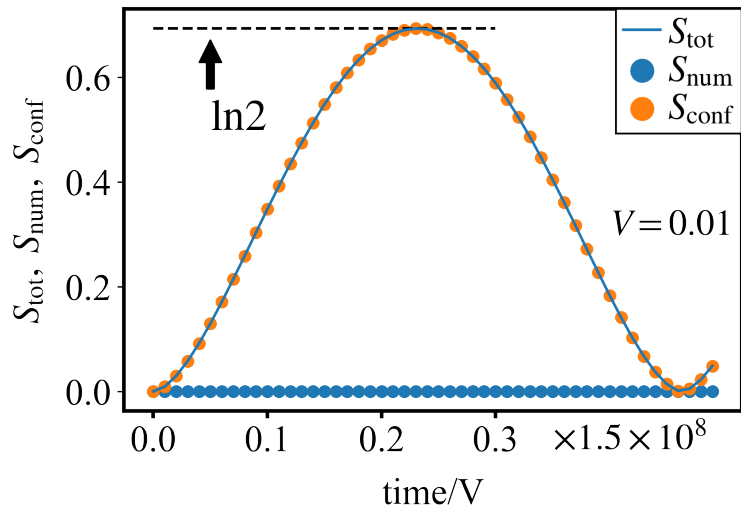


Figure 3.11: Time evolution of S_{tot} , S_{num} , and S_{conf} . We employ the same data used to draw Fig. 3.9.

when distance x between them is smaller than $\xi \log(2Vt)$. Hence, the growth of S_{tot} in the many particle case is expressed as

$$S_{\text{tot}} \propto x(t) = \xi \log(2Vt). \quad (3.43)$$

3.6 Non-Hermitian many-body localization

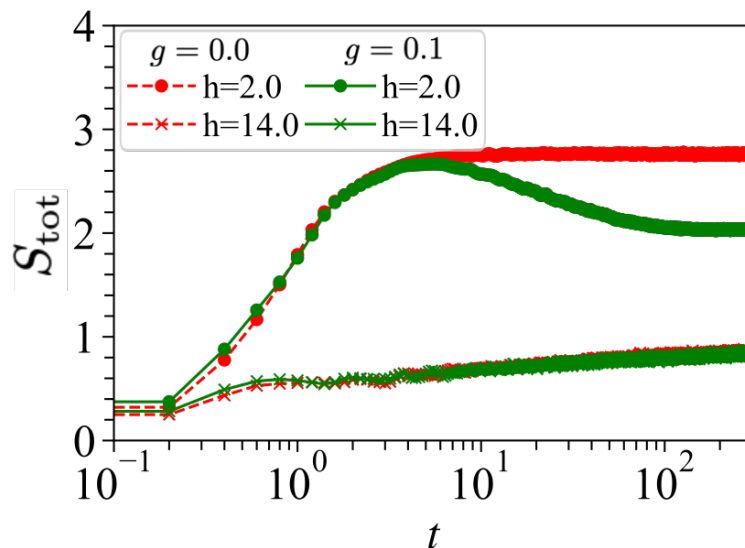


Figure 3.12: S_{tot} as a function of time with $L = 12$, averaged over various disorder configurations in the two cases of $h = 2$ and 14 , where h represents disorder strength.

The authors of Ref. [36] have studied the localization problem in a Hatano-Nelson model with many-body interaction. They have reported on level statistics, entanglement entropy of eigenstates, and complex spectrum (cf. Chapter 2).

Let us focus on entanglement entropy in the many-body HN model. The authors of Ref. [36] reported on the time evolution of S_{tot} only in the weak disorder case of $h = 2$ and the strong disorder case of $h = 14$. The behavior of S_{tot} shown in Fig. 3.12 is qualitatively similar to that reported in Ref. [36]. As we shown in Fig. 3.12, S_{tot} exhibits a power-law growth in the weak disorder case and a logarithmic growth in the strong disorder case. These features are observed in the Hermitian case, as shown in Fig. 3.6; apparently, non-Hermiticity (i.e., non-reciprocal hopping) does not affect S_{tot} in a drastic manner. This observation leads to one of the two questions in Chapter 1, i.e., to what extent non-reciprocal hopping qualitatively changes the entanglement behavior. The other question is whether the relation between a non-reciprocal parameter g and the localization length still holds in a many-body system (see Chapter 2 for details).

We have conducted a systematic study of $S_{\text{tot}}(t)$ and revealed characteristic disorder-dependence of $S_{\text{tot}}(t)$, which is the answer to the first question, that is, non-reciprocal hopping qualitatively changes the entanglement behavior. Additionally, the characteristic behavior of $S_{\text{tot}}(t)$ closely related to the second question. Such a unique behavior of $S_{\text{tot}}(t)$ allows estimation of the localization length.

Chapter 4

Non-Hermitian wave packet dynamics

In this chapter, we study how a wave packet spreads in a disordered non-Hermitian system, considering the Hatano–Nelson model as a concrete example. Interestingly, a cascade-like wave packet spreading in the Hermitian case is suppressed within the clean limit and at weak disorder, while it revives in the vicinity of the localization–delocalization transition. We explain why the wave-packet dynamics in the non-Hermitian system becomes considerably different from that in the Hermitian case.

4.1 Single-particle case: Hatano-Nelson model and Aubry-André model

Let us consider the Hatano-Nelson model [33] under the periodic boundary condition, which we introduced in Section 2.3:

$$\begin{aligned} H &= - \sum_{j=0}^{L-1} \left(\Gamma_L |j+1\rangle \langle j| + \Gamma_R |j\rangle \langle j+1| \right) \\ &+ \sum_{j=0}^{L-1} W_j |j\rangle \langle j|, \end{aligned} \quad (4.1)$$

where $|j\rangle$ represents a single-particle state localized at site j , $\Gamma_L = e^g \Gamma_0$ and $\Gamma_R = e^{-g} \Gamma_0$ with g being a parameter quantifying the degree of non-reciprocity. g can be regarded as an imaginary vector potential [33]. The first two terms represent the nearest neighbor hopping with non-reciprocal hopping amplitude.¹ The third term is on-site potential. We have chosen quasi-periodic potential as on-site potential, i.e.,

$$W_j = W \cos(2\pi\theta j + \theta_0), \quad (4.2)$$

which effectively acts as random potential (Aubry-André model [53]), where θ is an irrational constant, which we choose to be the so-called (inverse) golden ratio: $\theta = (\sqrt{5} - 1)/2$. $\theta_0 \in R$ is a free parameter used to consider a disorder average; θ_0 's distributed uniformly in the range of $\theta_0 \in [0, 2\pi)$ provide a random ensemble. The θ_0 -averaging has been considered over 50 samples, e.g., $x_G(t)$ and its fluctuation (Figs. 4.4 and 4.6), S_{tot} , S_{num} and S_{conf} .

¹In non-Hermitian quantum mechanics with non-reciprocal hopping, choice of the boundary condition is a subtle issue in its statics, whereas it is not a central issue in its dynamics (see Appendix A for details).

In the Hermitian case ($g = 0$), the eigenstates are extended when W is sufficiently weak ($W < W_c$), while they are localized for $W > W_c$, where

$$\frac{W_c}{2\Gamma_0} = 1, \quad (4.3)$$

which provides the critical point (cf. Section 2.2). This is consistent with the divergence of localization length ξ defined in the localized phase [42, 67]:

$$\xi^{-1} \simeq \log \frac{W}{2\Gamma_0}. \quad (4.4)$$

The localization length ξ diverges as W approaches the critical value (4.3) from above.

In the non-Hermitian case ($g \neq 0$), the critical value g_c is related to the localization length ξ as [34, 73]²

$$\xi^{-1} = g_c. \quad (4.5)$$

Substituting Eq. (4.5) into Eq. (4.4), the delocalization transition point is

$$W_c = 2\Gamma_0 e^g = 2\Gamma_L, \quad (4.6)$$

where $\Gamma_L > \Gamma_R$ ($g > 0$); i.e., W_c in the non-Hermitian case is found simply by replacing Γ_0 in Eq. (4.3) with the left/large hopping amplitude $\Gamma_L = e^g \Gamma_0$. Both in the Hermitian and non-Hermitian cases, the location of the transition point (4.6) does not depend on the energy, indicating the absence of a mobility edge. When $g \neq 0$, the eigenenergy ϵ_n becomes complex in the extended phase ($W < W_c = 2\Gamma_L$) as is also seen in the case of free particle motion described in Appendix C. Contrastingly, the eigenenergy remains real in the localized phase ($W > W_c$). Thus, the localization–delocalization transition is accompanied by a real–complex transition of the eigenenergies (see Section 2.3 and Appendix A for details).

Let us consider how the initially localized wave packet evolves in time following quantum mechanics. Four panels of Figs. 4.1 and 4.2 show examples of such dynamics. We consider the wave packet located in site $j = j_0$ at $t = 0$:

$$|\psi(t=0)\rangle = |j_0\rangle. \quad (4.7)$$

At time t , the wave packet that follows the Schrödinger equation with time-independent Hamiltonian evolves as

$$\begin{aligned} |\psi(t)\rangle &= \sum_j \psi_j(t) |j\rangle \\ &= \sum_n c_n e^{-i\epsilon_n t} |n\rangle, \end{aligned} \quad (4.8)$$

²In the non-Hermitian case: $g \neq 0$, g plays the role of an imaginary vector potential that appears in the wave functions of a localized state so that

$$\psi^{L,R}(x) \sim \exp\left(-\frac{|x-x_c|}{\xi} \mp g(x-x_c)\right),$$

where $\psi^{L,R}(x)$ are left and right eigenvectors; x_c is its localization center, while ξ represents the corresponding localization length. If $|g| > \xi^{-1}$, $\psi^L(x)$ or $\psi^R(x)$ diverges; the wave functions $\psi^{L,R}(x)$ no longer represent an exponentially localized state. Therefore, the delocalized transition point is determined by the condition (4.5). Further details are presented in Section 2.3.

where $|n\rangle$ represents the n th single-particle eigenstate of the Hamiltonian with an eigenenergy ϵ_n , i.e., $H|n\rangle = \epsilon_n|n\rangle$, while $c_n = \langle\langle n|\psi(t=0)\rangle\rangle$. Here, $\langle\langle n|$ represents the *left* eigenstate defined as $\langle\langle n|H = \epsilon_n\langle\langle n|$, where $\langle\langle n| \neq |n\rangle^\dagger$. Notably, we impose the biorthogonal condition, i.e., $\langle\langle n|m\rangle\rangle = \delta_{n,m}$. In the case of $g \neq 0$, the eigenenergy ϵ_n is typically complex; cf. the free particle case in Appendix C [Eqs. (4.14) and (4.15)], so that the probability amplitude of the eigenstate $|n\rangle$ tends to exponentially grow or decay reflecting $\text{Im}(\epsilon_n) > 0$ or $\text{Im}(\epsilon_n) < 0$. Consequently, the normalization condition $\langle\psi(t)|\psi(t)\rangle = 1$ is not satisfied. In the actual computation, we therefore rescale (renormalize) $|\psi(t)\rangle$ at every interval Δt as

$$|\psi(t)\rangle \rightarrow |\tilde{\psi}(t)\rangle = \frac{|\psi(t)\rangle}{\sqrt{\langle\psi(t)|\psi(t)\rangle}}, \quad (4.9)$$

where Δt is chosen as $\Delta t \simeq 10^{-4} - 10^{-1}$.

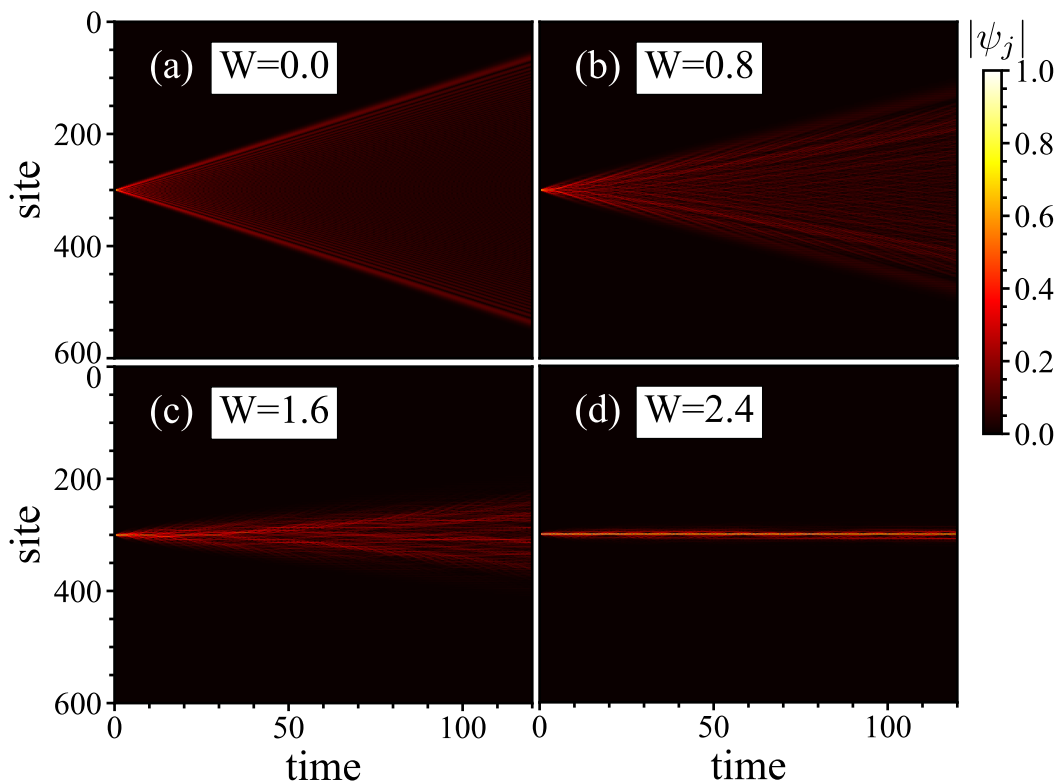


Figure 4.1: Single-particle dynamics in the Hermitian case of $g = 0$. Time evolution of the initial wave packet: $\psi_j(0) = \delta_{j,j_0}$ is visualized with $j_0 = 300$ and $L = 601$. The amplitude $|\psi_j(t)|$ [cf. Eq. (4.8)] is shown by a gradation of plot colors indicated in the color bar. The x -axis represents time t , and the y -axis represents the site j . Different panels (a-d) correspond to different values of disorder strength W ; $W = 0.0, 0.8, 1.6, 2.4$, respectively, for panels (a-d). θ_0 is fixed at $\theta_0 = 0$ (i.e., no disorder averaging). Taken from Fig. 1 of Ref. [74]. ©2022 American Physical Society.

Let us first consider the Hermitian case. The four panels of Fig. 4.1 show the distribution of $|\psi_j(t)|$ in the Hermitian case for different values of W . At site j (the y -axis) and at time t (the x -axis), the amplitude of $|\psi_j(t)|$ is specified

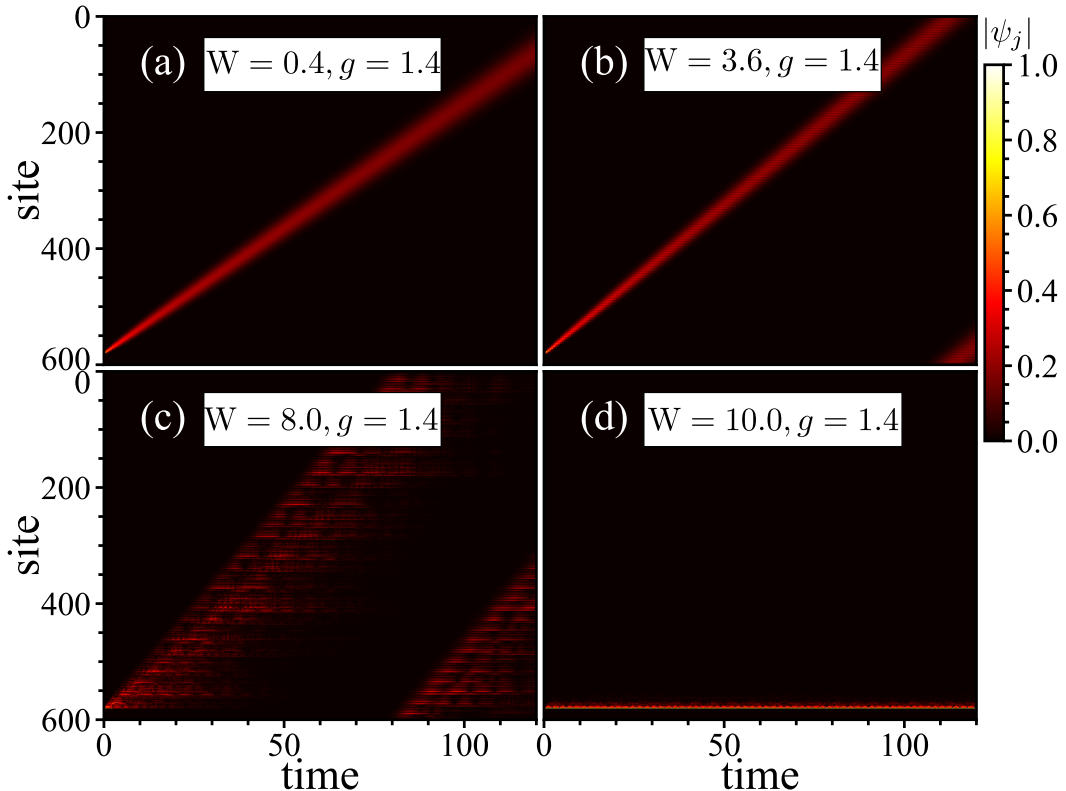


Figure 4.2: Single-particle dynamics in the non-Hermitian case: $g = 1.4$. Time evolution of the initial wave packet under the same condition as in Fig. 4.1 with $\theta_0 = 0$, $j_0 = 580$, and $L = 601$. The values of disorder strength W are $W = 0.4, 3.6, 8.0$, and 10.0 , respectively, for panels (a–d). Taken from Fig. 2 of Ref. [74]. ©2022 American Physical Society.

by a variation of the plot color indicated in the color bar. In the clean limit [Fig. 4.1(a)], the wave packet spreads symmetrically in two directions. As W increases (Fig. 4.1(b), (c)), spreading of the wave packet is weakly suppressed. Finally, beyond the critical disorder strength (Fig. 4.1(d)), the wave packet ceases to spread. The four panels of Fig. 4.2 show the distribution of $|\psi_j(t)|$ in the case of $g = 1.4$ ($L = 601$, $j_0 = 580$) for different values of W . Unlike the Hermitian case³ (Fig. 4.1), the four panels show that the wave packet does not spread at least in the regime of weak W [cases of panels (a–b)],⁴ but rather *slides* in the direction imposed by the non-reciprocity g .

In the non-Hermitian case, the wave packet shows unique unidirectional motion in the weakly disordered regime $W \ll W_c$ [panels (a–b)] [42]; however the Hermitian-like (cascade-like) wave packet spreading reappears in the vicinity of the localization transition point $W \sim W_c$ [panel (c)]. Beyond the critical dis-

³In the Hermitian limit ($g = 0$) the wave packet *spreads* with time, unless disorder W is not too strong ($W/J < 2$); see e.g., Fig. 2 of Ref. [42]. In a non-Hermitian system ($g \neq 0$), the wave packet does not show the cascade-like spreading seen in the Hermitian case. In any case, the dynamics becomes very different from the Hermitian case. Here, we further clarify this point.

⁴At least in the short time scale; in the long time regime at which the imaginary part $\text{Im } \epsilon_n$ comes into play, $|\psi(t)\rangle$ decays into a single eigenstate with a maximal $\text{Im } \epsilon_n$; see Appendix C for details. In such a long time scale the wave packet may spread in time, but not in the sense considered here.

order strength $W > W_c$, the wave packet suddenly ceases to spread, thereby exhibiting shows localization tendency [panel (d)]. Comparing the three cases on the delocalized side [panels (a-c)], one also notices that the sliding velocity of the wave packet tends to increase as W is increased [42].

To understand why in the non-Hermitian case the wave-packet dynamics become substantially different from that in the standard Hermitian case, the clean limit, $W = 0$, must be considered first. In this limit, the eigenstates are plane waves $\langle j|k\rangle = e^{ikj}/\sqrt{L}$, so that

$$\begin{aligned} |\psi(t)\rangle &= \sum_k e^{-i\epsilon_k t} |k\rangle \langle k|j_0\rangle \left(\equiv \sum_k \psi_k(t) |k\rangle \right) \\ &= \frac{1}{\sqrt{L}} \sum_j \sum_k e^{-i\epsilon_k t + ik(j_0-j)} |j\rangle, \end{aligned} \quad (4.10)$$

where $|\psi(t)\rangle$ is expressed as a superposition of the plane waves. At site j , each contribution to $|\Psi(t)\rangle$ is expressed in the form of a phase factor

$$e^{i\phi(k)} = e^{-i\epsilon_k t + ik(j_0-j)}. \quad (4.11)$$

At $t = 0$ and $j \neq j_0$, such contributions are out of phase and cancel each other, while at $j = j_0$ they add up in phase to form the peak of the initial wave packet. Similarly, at $t > 0$, the only non-vanishing contributions [in the summation over k in Eq. (4.10)] are those from the neighborhood of $k = \bar{k}$ at which the phase $\phi(k)$ becomes *stationary*; i.e., $\phi'(\bar{k}) = 0$, or

$$2\Gamma_0 \sin \bar{k} t = j - j_0. \quad (4.12)$$

Since $|\sin \bar{k}| \leq 1$, $|j - j_0| = 2\Gamma_0 t \equiv v_f t$ defines the position of the wave front, or a “light cone” [42]. In the Hermitian limit the initially localized wave packet spreads linearly in time as $\Delta x(t) \propto t$ (i.e., $\Delta x(t) \sim t^\sigma$) with the exponent $\sigma \simeq 1$, where

$$\Delta x(t) = \sqrt{\sum_j (j - j_0)^2 |\psi_j(t)|^2} \quad (4.13)$$

represents the spread of the light cone. In fact, the stationary phase condition correctly characterizes the free particle motion. Further details are shown in Appendix B. The addition of disorder W suppresses the wave-packet spreading; as shown in Fig. 2 of Ref. [42], the velocity $v = \Delta x(t)/t$ characterizing the spreading of wave packet decreases linearly with W and vanishes at $W = W_c$.

Upon the addition of non-Hermiticity $g \neq 0$, a different mechanism or a principle governs the wave-packet dynamics of Eq. (4.10), since the eigenenergies ϵ_k become complex:

$$\epsilon_k = -2\Gamma_0 \cos(k - ig), \quad (4.14)$$

which in the complex energy plane, takes values on an ellipse:

$$\left(\frac{\text{Re } \epsilon_k}{\Gamma_0 \cosh g} \right)^2 + \left(\frac{\text{Im } \epsilon_k}{\Gamma_0 \sinh g} \right)^2 = 1. \quad (4.15)$$

Among the k values satisfying Eq. (4.15), those with maximal or near maximal $\text{Im } \epsilon_k$ become important in the superposition (4.10). In case of Eq. (4.14), such values of k are found near

$$k_0 = -\pi/2. \quad (4.16)$$

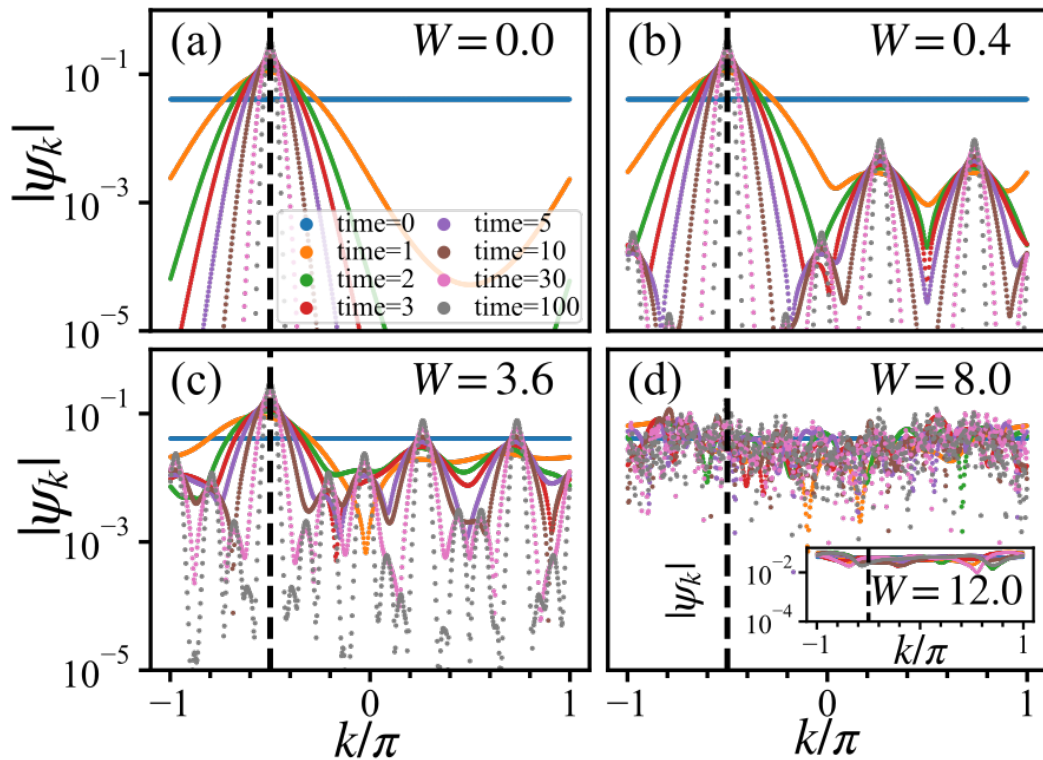


Figure 4.3: Single-particle dynamics; profile of the wave function in k -space. The Fourier transform $|\psi_k(t)|$ [Eq. (4.10)] of the wave packet is plotted as a function of k at different time slices $t = 0, 1, 2, 3, 5, 30,$ and 100 as indicated in the inset of panel (a). Panels (a–d) and the inset of panel (d) correspond, respectively, to different values of disorder strength $W = 0, 0.4, 3.6, 8.0,$ and 12.0 with $g = 1.4$ and $\theta_0 = 0$. Other settings follow those of Fig. 4.2. Taken from Fig. 3 of Ref. [74]. ©2022 American Physical Society.

Thus, in the non-Hermitian free-particle dynamics, the initial state (4.7) dissolves in the course of time evolution (4.10) into a Gaussian wave packet:

$$\begin{aligned}
 |\psi(t)\rangle &\simeq \sum_j |j\rangle \exp\left(-\frac{((j_0 - j) + 2(\cosh g)t)^2}{4(\sinh g)t}\right) \\
 &\times e^{2(\sinh g)t} / \sqrt{4(\sinh g)t}, \quad (4.17)
 \end{aligned}$$

which are composed of plane waves with k values found near k_0 . As for the derivation of Eq. (4.17), see Eq. (C.2) and related arguments in Appendix C. The resulting Eq. (4.17) is a wave packet that slides in the direction imposed by g , and its expanse gradually increases as time evolves. The aforementioned argument is summarized in a guiding principle:

- i the survival of $\text{Max Im } \epsilon_k$ has priority over
- ii the stationary phase condition [cf. Eq. (4.12) in the Hermitian case].

The non-Hermitian (free-particle) dynamics is fully governed by principle (i), which is replaced with principle (ii) when principle (i) tends to be ineffective. In Fig. 4.3, panel (a) the distribution of $|\psi_k(t)|$ at certain fixed values of t are

shown. $|\psi_k(t)|$ shows a Gaussian-type distribution centered at $k = k_0$, and its width tends to become narrower as t evolves [cf. Appendix C].

Panels (b–e) of Fig. 4.3 show how the addition of disorder W affects and eventually destroys this peak structure of ψ_k . In panel (b), two side peaks appear at $k = k_1$ and k_2 , which reflect the quasi-periodic nature of the potential (4.2); Bloch waves of these k values are quasi-commensurate with the potential. As W is increased, such side peaks multiply [panel (c)], and the system gradually evolves into the cascade regime represented by panel (d), where the distribution of $|\psi_k(t)|$ is almost uniform, but still there are plenty of tiny peaks, while in the localized regime [inset of panel (d)], the distribution becomes flat and smooth.

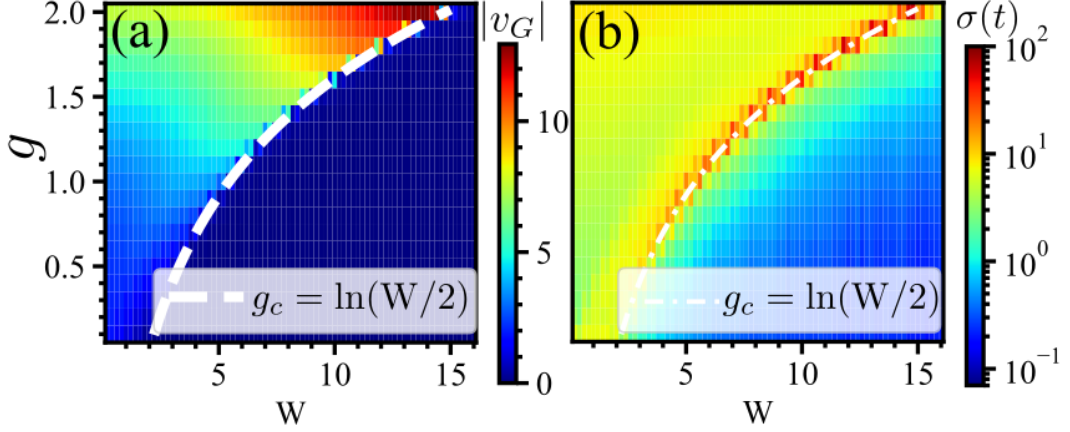


Figure 4.4: Single-particle dynamics; velocity and density fluctuation profiles averaged over 50 samples with different θ_0 . Panel (a) and (b) represent the sliding velocity $v_G = [x_G(t) - x_G(0)]/t$ and the density fluctuation $\sigma(t) = \Delta x(t) - \Delta x(0)$ in the (W, g) -plane by a variation of plot colors indicated in the color bar. These quantities are evaluated at $t = t_1 = 20$ in the same initial state as in Figs. 4.2 and 4.3. Taken from Fig. 4 of Ref. [74]. ©2022 American Physical Society.

To further quantify features specific to the non-Hermitian wave packet dynamics, we must focus on

1. how speedily the center of gravity

$$x_G(t) = \sum_j j |\psi_j(t)|^2 \quad (4.18)$$

of the wave packet moves, and

2. to what extent the wave packet is spread around $x_G(t)$.

$x_G(t) \simeq x_G(0) + v_G t$, so that the velocity of $x_G(t)$ is given by v_G . In panel (a) of Fig. 4.4, the magnitude of v_G is plotted based on the variation of plot color, where v_G is determined by evaluating $x_G(t)$ at $t = t_1$ ⁵) as changing the set of parameters (W, g) , and is indicated by a variation of plot color. The plot shows that v_G is finite in the extended phase $W < W_c$, while it practically vanishes

⁵The measurement time t_1 has been chosen to be a value ($t = t_1 = 20$ in Fig. 4.4) such that the wave packet does not travel across the (periodic) boundary.

in the localized phase $W > W_c$. The location of the phase boundary (4.6), or equivalently,

$$g = \log \frac{W}{2} \quad (4.19)$$

is indicated by a broken curve in the panel. On the side of the extended phase $W < W_c$, v_G continues to take a relatively large value, until approaching the phase transition; at a fixed value of g , it rather tends to increase as W increases, until it abruptly falls at the phase transition.

Panel (b) shows a similar plot for the quantity: $\sigma(t) = \Delta x(t) - \Delta x(0)$ at a certain time $t = t_1$, where $\Delta x(t)$ has been redefined as

$$\Delta x(t) = \sqrt{\sum_j (j - x_G(t))^2 |\psi_j(t)|^2}. \quad (4.20)$$

The quantity $\sigma(t)$ is expected to measure the extent to which the density $\rho_j(t)$ is spread around $x_G(t)$. The plot shows that similar to the behavior of v_G in panel (a), the spread of the wave packet also exhibits a sharp distinction in the extended ($W < W_c$) and localized ($W > W_c$) phases. $\Delta x(t)$ takes a finite value on the side of the extended phase: $W < W_c$, and the appearance of a peak as W is increased toward and close to the localization transition (4.19) at a fixed value of g . We interpret that this enhancement of $\sigma(t)$ slightly before the localization transition reflects the cascade-like explosion of the wave packet observed in the density profile in panel (c) of Fig. 4.2.

4.2 Case of an interacting system

Here, we consider how the presence of interaction affects the above non-interacting case. As a concrete model, we have employed the following bosonic tight-binding model with the nearest neighbor inter-particle interaction V :

$$\begin{aligned} \mathcal{H} &= - \sum_{j=0}^{L-1} \left(\Gamma_L b_j^\dagger b_{j+1} + \Gamma_R b_{j+1}^\dagger b_j \right) \\ &+ \sum_{j=0}^{L-1} \left(V \hat{n}_j \hat{n}_{j+1} + W_j \hat{n}_j \right), \end{aligned} \quad (4.21)$$

where b_j^\dagger (b_j) creates (annihilates) a boson at site j , while $\hat{n}_j = b_j^\dagger b_j$ counts the particle number n_j at site j . This is the bosonic version of a hybrid consisting of Hatano–Nelson and Aubry–André models. Following Refs. [36] and [37], we assume that our particles are hard-core bosons: $n_j = 0, 1$.⁶ Figure 4.5 shows examples of multi-particle dynamics in this system. The initial state is prepared in the following domain wall state:

$$|\Psi(t=0)\rangle = |00 \cdots 011 \cdots 1\rangle, \quad (4.22)$$

⁶If they are true fermions, anticommutation of b_j and b_j^\dagger may lead to a quantitatively different result under a periodic boundary condition, particularly in the delocalized regime; see Appendix D for details.

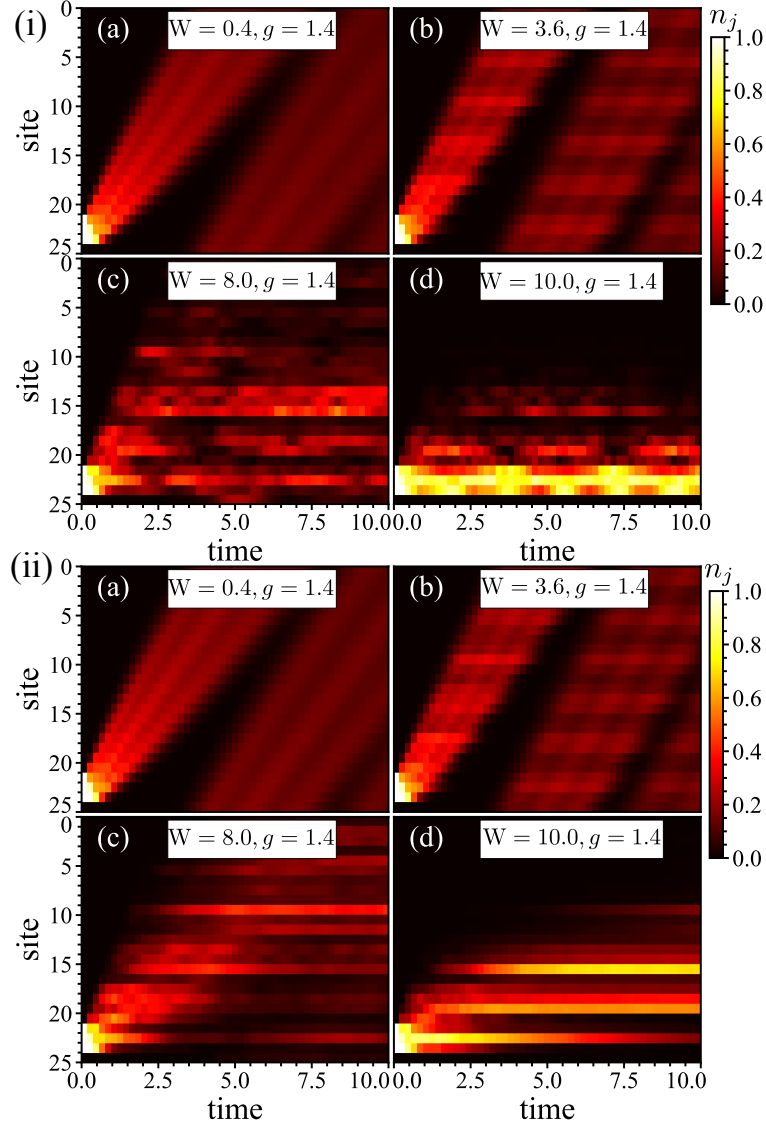


Figure 4.5: Multi-particle dynamics; evolution of the initial wave packet chosen to be in a domain wall form expressed in Eq. (4.22). The eight panels show the evolution of the particle density $n_j(t)$ at site j and at time $t = t_1$ based on the gradation of plot colors indicated in the color bar, where t_1 is chosen as $t_1 = 2.2$ with $L = 25$, $g = 1.4$, and $\theta_0 = 0$. Panels (a–d) correspond to $W = 0.4, 3.6, 8.0$, and 10.0 , respectively, for panels (a–d). The four upper panels in case (i) represent the non-interacting case: $V = 0$, while those in case (ii) represent an interacting case: $V = 2$. Taken from Fig. 5 of Ref. [74]. ©2022 American Physical Society.

i.e., bosons occupy the last N_b sites⁷: N_b represents the number of bosons, and here we have chosen $N_b = 3$. At time t , the initial state (4.22) evolves as

$$|\Psi(t)\rangle = \sum_{\mu} c_{\mu} e^{-iE_{\mu}t} |\mu\rangle, \quad (4.23)$$

⁷In the actual simulation, we have shifted the domain of occupied sites; i.e., $\Pi_{j=L-2}^{j=L} b_j^{\dagger} |0\rangle \rightarrow \Pi_{j=L-3}^{j=L-1} b_j^{\dagger} |0\rangle$ so that the wave function does not spread across the boundary.

where $|\mu\rangle$ is the eigenstate of the Hamiltonian expressed in Eq. (4.21) and E_μ is the corresponding eigenenergy: $\mathcal{H}|\mu\rangle = E_\mu|\mu\rangle$. Here, $c_\mu = \langle\langle\mu|\Psi(t=0)\rangle\rangle$. Here, $\langle\langle\mu|$ with $\langle\langle\mu|$ representing the left eigenstate defined by $\langle\langle\mu|\mathcal{H} = E_\mu\langle\langle\mu|$, where $\langle\langle\mu| \neq |\mu\rangle^\dagger$. We impose the biorthogonal condition, i.e., $\langle\langle\mu|\nu\rangle = \delta_{\mu,\nu}$, analogous to the single-particle case. As the single-particle eigenenergy ϵ_n is complex in general, the many-body eigenenergy E_μ is also complex. As a result, the time-evolved wave packet $|\Psi(t)\rangle$ as expressed in Eq. (4.23) tends to grow exponentially. To avoid this computational difficulty, we rescale (renormalize) $|\Psi(t)\rangle$ in the same manner as in Eq. (4.9) at every interval $\Delta t \simeq 10^{-4} - 10^{-1}$ in the actual computation. The eight panels of Fig. 4.5 show the evolution of the particle density

$$n_j(t) = \langle\Psi(t)|\hat{n}_j|\Psi(t)\rangle \quad (4.24)$$

at site j at time t based on color variation; the higher the density, the brighter the color. The system size L is set as $L = 25$. The four panels in the upper case (i) represent the non-interacting case: $V = 0$, while those in the lower case (ii) represent an interacting case: $V = 2$. In these panels one can still see the tendency observed in the single-particle dynamics; e.g., the cascade-like feature in wave packet spreading can be seen in panel (c) [both in (i) and (ii)].

Figure 4.6 represents the distribution of v_G and $\sigma(t) = \Delta x(t) - \Delta x(0)$ in the parameter space: (W, g) ; the two figures correspond, respectively, to the cases of $V = 0$ and $V = 2$. v_G and $\sigma(t)$ are calculated similarly in the single-particle case as follows:

$$\begin{aligned} x_G(t) &= \sum_j j n_j(t) \simeq x_G(0) + v_G t, \\ \Delta x(t) &= \sqrt{\sum_j (j - x_G(t))^2 n_j(t) / \sum_j n_j(t)}. \end{aligned} \quad (4.25)$$

In both the figures, both v_G and $\sigma(t)$ take a finite value on the side of the extended phase: $W < W_c$, while they vanish on the localized side: $W > W_c$. In $\sigma(t)$ [panels (b)], an enhancement is also observed before the localization transition. In single-particle dynamics, as shown in Fig. 4.2, the wave packet spreading in non-Hermitian systems shows the specific and unusual features. Figure 4.5 shows that these features found in single-particle dynamics are essentially maintained in multi-particle dynamics though somewhat masked by the inter-particle interaction V .

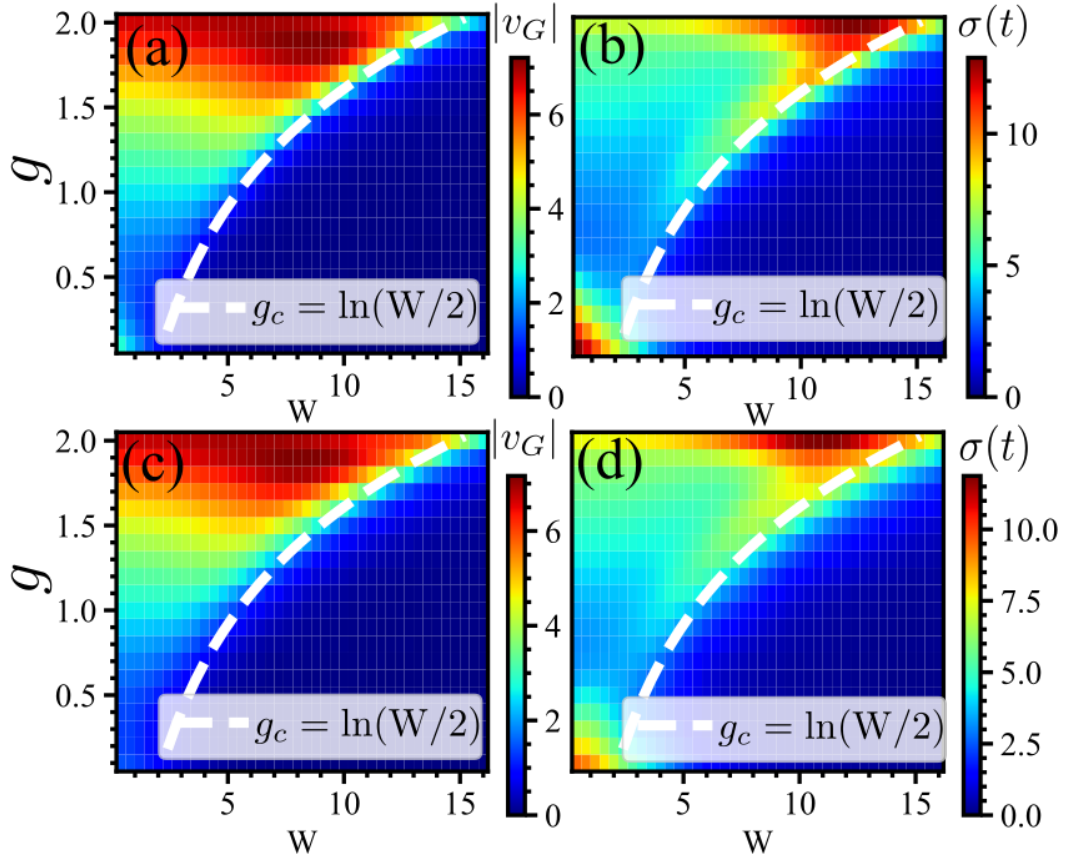


Figure 4.6: Multi-particle dynamics; velocity and density fluctuation profiles averaged over 50 samples with different θ_0 . Panels (a) and (c) show distribution of v_G in the (W, g) -plane, while panels (b), (d) represent a similar plot for $\sigma(t) = \Delta x(t) - \Delta x(0)$. v_G and $\Delta x(t)$ are evaluated using in Eq. (4.25) in the multi-particle case with the same initial state as in Fig. 4.5. Panels (a–b) represent the non-interacting case: $V = 0$, panels (c–d) an interacting case: $V = 2$. Taken from Fig. 6 of Ref. [74]. ©2022 American Physical Society.

Chapter 5

Non-Hermitian entanglement dynamics

5.1 Entanglement dynamics

The entanglement entropy $S_{\text{tot}}(t)$ is defined for a quantum system consisting of two subsystems so that it can measure how the two subsystems are quantum-mechanically entangled. This can be rephrased as follows: $S_{\text{tot}}(t)$ measures the complexity of a given quantum state by using a reduced density matrix for each subsystem. Hence, it also characterizes spreading of a wave packet [39, 40, 41], since such spreading tends to enhance the complexity of the given state. Let us consider the time evolution of $S_{\text{tot}}(t)$ for an initial state. In a non-interacting system, $S_{\text{tot}}(t)$ increases as the corresponding wave function spreads in the system. The initial growth of the number entropy $S_{\text{num}}(t)$ in the quench dynamics is essentially due to this effect (Fig. 5.1 and Fig. 5.4). In Hermitian systems with reciprocal hopping, an initially localized wave packet spreads symmetrically in two directions in the clean limit and, after a duration t , the wave function extends to a region of width $\Delta x \sim 2v_f t$, where v_f is the velocity of the wave front: $v_f \simeq J$ [42]. Consequently, the entanglement entropy also increases as $S_{\text{tot}}(t) \propto \Delta x \sim 2v_f t$. In interacting systems, the same argument applies if v_f is replaced with the Lieb-Robinson velocity [75]. The interaction also modifies the superposition of eigenstates in a nontrivial manner in the time evolution of a wave packet, leading to the generation of entanglement. In the presence of disorder W , as its strength is increased, wave packet spreading tends to be suppressed; v_f decreases and at a certain critical value $W = W_c$, v_f vanishes. When $W > W_c$, the wave function is localized, and the wave packet spreading is essentially suppressed. As for the behavior of $S_{\text{tot}}(t)$, a rapid growth in the extended (delocalized) phase is experienced, while such growth is considerably suppressed in the localized phase [see Fig. 5.1, panel (a)] [22].

Considering how a wave packet spreads in non-Hermitian systems with non-reciprocal hopping, we proceed to the analysis of how the entanglement entropy $S_{\text{tot}}(t)$ evolves over time in such systems. We employ the same many-body Hamiltonian (4.21) as in the analysis of wave packet spreading, while the initial state is prepared as the following density wave form (or Néel form in the pseudo-spin language [38]):

$$|\Psi(t=0)\rangle = |101010\dots\rangle, \quad (5.1)$$

where on the right hand side of the equation we have employed the computational basis $|\nu\rangle = |n_1 n_2 \dots n_L\rangle$; $n_j = 0, 1$ represents occupation of the j th site. ¹

¹We assume that our particles are hard-core bosons unless otherwise mentioned; cf. Ap-

5.2 Entanglement entropy in the non-interacting limit: wave packet spreading versus entanglement entropy

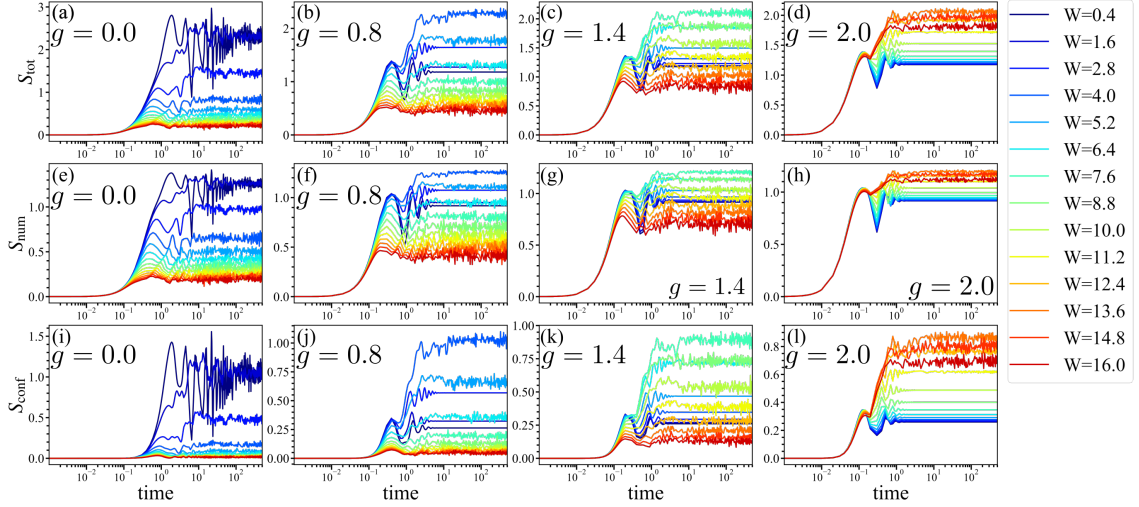


Figure 5.1: Entanglement dynamics in the non-interacting case $V = 0$. Three panels (a), (e), and (i) in the first column represent the Hermitian case $g = 0$, while the other panels represent non-Hermitian cases $g \neq 0$; $g = 0.8$ for panels (b), (f), and (j) in the second column ($W_c \simeq 4.5$), $g = 1.4$ for panels (c), (g), and (k) in the third column ($W_c \simeq 8.1$), $g = 2$ for panels (d), (h), and (l) in the fourth column ($W_c \simeq 14.8$). Panels (a)–(d) in the first row represent the evolution of $S_{\text{tot}}(t)$, while panels (e)–(h) in the second row and panels (i)–(l) in the third row represent $S_{\text{num}}(t)$ and $S_{\text{conf}}(t)$, respectively. They are evaluated based on the average over 50 samples with different θ_0 in the system of $L = 12$ with the initial state (5.1). Taken from Fig. 7 of Ref. [74]. ©2022 American Physical Society.

Figure 5.1 shows time evolution of the entanglement entropy for the initial state (5.1) in non-interacting systems with a variable strength of non-Hermiticity g . Panels (a), (e), and (i) represent $S_{\text{tot}}(t)$, $S_{\text{num}}(t)$, and $S_{\text{conf}}(t)$, respectively, in the Hermitian case $g = 0$. The characteristic of the Hermitian limit in the delocalized regime is that particles initially spread in two hopping directions, and thereafter, the system eventually reaches an equilibrium state [76, 77] resulting from the interference of many plane waves [cf. Eq. (4.10)]. The entanglement entropies show a rapid initial growth and approach a saturated value in such weak W regime, while they are strongly suppressed as W is further increased in the localized regime. In panel (e) we focus on the behavior of $S_{\text{num}}(t)$. In the two cases of $W = 0.4$ and 1.6 in the weak disorder regime, $S_{\text{num}}(t)$ first rapidly grows and approaches the same value subsequently. In any case, particles spread in the delocalized regime, and the system reaches equilibrium after a sufficiently long time although this time lengthens as W increases. $S_{\text{conf}}(t)$ also grows in the delocalized regime; however, the growth is slightly delayed compared with that of $S_{\text{num}}(t)$ [see Fig. 5.1 (i)]. As W exceeds the critical value $W_c = 2$, both the number and configuration entropies decrease, but remain finite. This is because

pendix D.

even in the localized phase, the localization length ξ is finite [78]. This effect is not negligible particularly if W is not exceedingly large and the system is not far from the transition point (see Appendix E).

As shown in Chapter 4, the addition of non-Hermiticity $g \neq 0$ renders a more drastic impact on wave packet dynamics; it breaks the symmetrical propagation of particles. In the presence of $g \neq 0$, the wave packet ceases to spread but starts to slide because non-reciprocal hopping strongly suppresses the interference of a wave function (see Appendix C). We have also discussed in the previous section that as W increases, this sliding velocity often increases, and when W is further increased and approaches the critical value W_c , the wave packet also begins to spread, exhibiting a cascade-like feature as in the Hermitian case at weak W . In the presence of random potential, different scattering paths are expected to interfere despite the presence of non-reciprocal hopping, i.e., quantum interference is partially recovered in this case. In the Hermitian case, the entanglement entropies diminish with an increase in W . In contrast, as g increases, this tendency becomes uncertain and is finally immediately reversed, as can be observed in panels (b)–(d) of Fig. 5.1. This result indicates that the total entanglement entropy is generated by disorder, exhibiting a maximum at finite $W = \tilde{W}_c$, subsequently decreasing.² We argue that this maximum of the

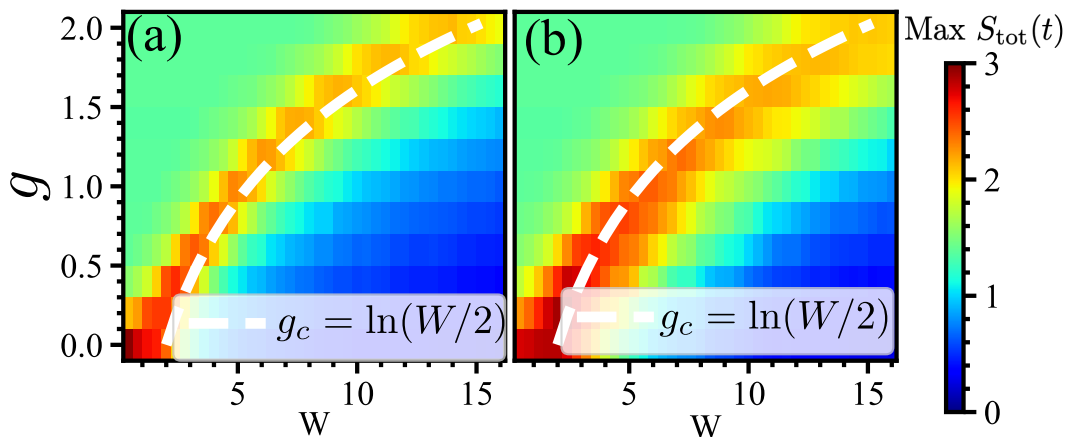


Figure 5.2: Distribution of the maximal entanglement entropy, $\text{Max } S_{\text{tot}}(t)$, in the (W, g) -plane derived from the data used to draw Figs. 5.1 and 5.4. $\text{Max } S_{\text{tot}}(t)$ in the time evolution is plotted in the (a) non-interacting case of $V = 0$ (the corresponding time evolution is plotted in Fig. 5.1) and (b) interacting case of $V = 2$ (id. in Fig. 5.1). The location of the delocalization–localization transition point in the non-interacting case: $g = \log W/2$ [as given in Eq. (4.19)] is indicated by a broken curve (in white) as a guide for the eyes. Taken from Fig. 8 of Ref. [74]. ©2022 American Physical Society with slight modification.

entanglement entropies is related to the delocalization–localization transition. In Fig. 5.2 (a), the maximal value $\text{Max } S_{\text{tot}}(t)$ ³ of the entanglement entropy is plotted in the (W, g) -plane. The distribution of $\text{Max } S_{\text{tot}}(t)$ resembles closely to that of $\sigma(t) = \Delta x(t) - \Delta x(0)$ [see Fig. 4.4 (b)], exhibiting a peak close to the boundary of the localized phase expressed by Eq. (4.19), if observed from the

²Number and configuration entropies also show similar behavior [see e.g., panels (f)–(h) and (j)–(l) of Fig. 5.1].

³Here, the maximal refers to maximal in the time evolution for a given g and W .

weak W (delocalized) side. That is, “the maximum of $\text{Max } S_{\text{tot}}(t)$ ” coincides with the regime where a cascade-like expansion of wave packet occurs in the density dynamics. In other words, the maximum of $\text{Max } S_{\text{tot}}(t)$ occurs close to the delocalization-localization transition point: $W = W_c$. The unusual behavior of entanglement entropies in the non-Hermitian non-reciprocal system is thus revealed to be directly related to a highly specific methodology through which a wave packet spreads or does not spread in this system.

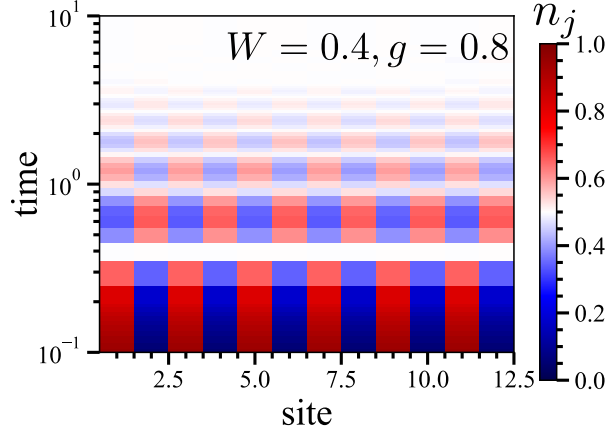


Figure 5.3: Damped oscillatory behavior in the density profile $n_j(t)$. The magnitude of $n_j(t)$ at site j (abscissa) at time t (ordinate) is expressed by a variation of plot color indicated in the color bar. The data is obtained for the density-wave type initial state of Eq. (5.1) with $g = 0.8$, $W = 0.4$, $\theta_0 = 0$, and $L = 12$. Taken from Fig. 9 of Ref. [74]. ©2022 American Physical Society.

Finally, let us comment on the number and configuration entropies. Panels (f)–(h) of Figs. 5.1 show the time evolution of the number entropy. In the delocalized phase, the number entropy rapidly grows in an initial stage in a manner that is almost independent of W and subsequently exhibits a damped oscillation. The damped oscillation is caused by the convergence of the initial state to a single eigenstate $|\mu_0\rangle$ with the maximal imaginary part of eigenenergy E_{μ_0} , which also affects the time evolution of the density profile shown in Fig. 5.3. Note that the state with the maximal imaginary part should be regarded as a non-equilibrium steady state. This also leads to the suppression of configuration entropy, as shown in panels (j)–(l) in Fig. 5.1. The convergence to a single destined eigenstate $|\mu_0\rangle$ implies the loss of superposition; the configuration entropy is significantly reduced in this regime of $W \simeq 0$. The destined eigenstate is delocalized, so that after a certain time, the initial density wave pattern of Eq. (4.22) is almost erased; (Fig. 5.3), while the number and configuration entropies exhibit a damped oscillation before converging to a final value. Beyond the critical disorder strength W_c , the number and configuration entropies significantly fluctuate as in the Hermitian case.

5.3 Case of $V \neq 0$ and $g \neq 0$: non-monotonic behavior

Considering the interaction: $V \neq 0$. Panels (a), (e), and (i) of Fig. 5.4 show the evolution of the entanglement entropy in the Hermitian limit: $g = 0$; panels (a),

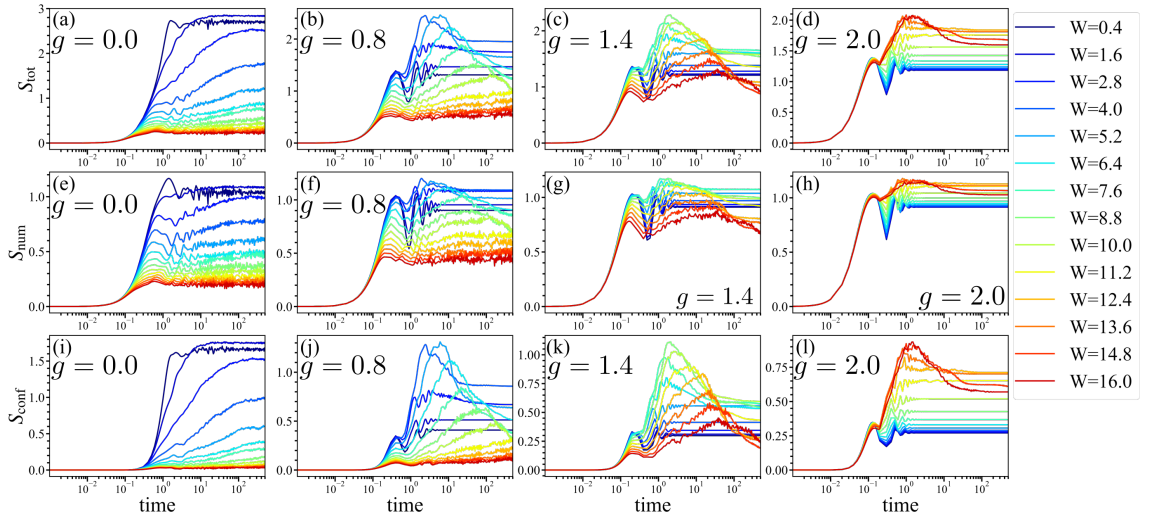


Figure 5.4: Entanglement dynamics in the interacting case ($V = 2$). Three panels (a), (e), and (i) in the first column represent the Hermitian case $g = 0$, while the other panels represent non-Hermitian cases $g \neq 0$; $g = 0.8$ for panels (b), (f), and (j) in the second column, $g = 1.4$ for panels (c), (g), and (k) in the third column, $g = 2$ for panels (d), (h), and (l) in the fourth column. The precise value of W_c is unknown in the interacting case ($V \neq 0$); however, it is not far from (slightly larger than) the non-interacting values given in the main text and caption of Fig. 5.1. Except for the value of V , the other conditions are the same as shown in Fig. 5.1. Taken from Fig. 10 of Ref. [74]. ©2022 American Physical Society.

(e), and (i) represent $S_{\text{tot}}(t)$, $S_{\text{num}}(t)$, and $S_{\text{conf}}(t)$, respectively. Comparing these panels with the corresponding panels in the non-interacting case [Fig. 5.1 (a), (e), and (i)], the total entanglement entropy $S_{\text{tot}}(t)$ [panel (a)] exhibits a speedy initial growth until reaching approximately $2\text{--}5 \times 10^1$, subsequently the growth decelerates and smoothly crosses over to a linear regime (in the logarithmic time scale). Comparing these behaviors in panel (a) with the ones in panels (e) and (i), the rapid initial growth arises from the number entropy $S_{\text{num}}(t)$, while the second slow growth forming a linear regime stems from the configuration entropy $S_{\text{conf}}(t)$ in panel (i).

As the non-Hermiticity g is also introduced (the remaining panels of Fig. 5.4), the entanglement dynamics changes its behavior as in the non-interacting case; cf. corresponding panels in Fig. 5.1. In contrast to the non-interacting case, a characteristic entanglement behavior appears in the interacting case; the second slow growth of S_{tot} begins to decay after a certain time scale, i.e., a characteristic non-monotonic behavior appears. The non-monotonic behavior appears in the intermediate regime of W ; however, it is unclear whether it emerges from the delocalized phase or localized phase. To elucidate this, we employ the maximal value of the entropies, which are expected to be maximal at ⁴ W_c close to the delocalization–localization transition as in the non-interacting case. In panel (b) of Fig. 5.2, the maximal value $\text{Max } S_{\text{tot}}(t)$ in the time evolution is plotted in the (W, g) -plane, exhibiting a broader maximum in contrast to the non-interacting

⁴Especially, the magnitude of configuration entropy $S_{\text{conf}}(t)$ [panel (l)] is sensitive to the change of W .

case [panel (a)], while the location of the peak is slightly shifted to the side of larger W from the non-interacting value (indicated by a white broken curve). The location of the phase boundary estimated from the peak of $\text{Max } S_{\text{tot}}(t)$ in Fig. 5.2 (b) is consistent with an earlier numerical result: $W_c \simeq 6\text{--}7$ at $g = 0.5$ in Ref. [37]. Comparing Fig. 5.2 with Fig. 5.4, the non-monotonic behavior appears in the delocalized side closely near the delocalization–localization transition point W_c .

The non-monotonic evolution of S_{tot} is a consequence of the competition between two mechanics: (i) dephasing and (ii) convergence of the superposition [Eq. (4.23)] into a single non-equilibrium steady state $|\mu_0\rangle$ with the maximal imaginary part of the eigenenergy E_{μ_0} [38]. In the absence of mechanism (ii), the mechanism (i) leads to a slow but unbounded growth of the configuration entropy, where it is typically logarithmic in the MBL phase [22]. For mechanism (ii) to be operational, the eigenenergy must have a finite imaginary part $\text{Im } E_\mu$. Panels (j)–(l) of Fig. 5.4 show the evolution of configuration entropy for different sets of parameters. In the localized regime, the non-monotonic behavior of the entanglement entropy (panels (b)–(d) of Fig. 5.4) stems mainly from the configuration entropy. Note that dephasing enhances the configuration entropy, whereas the convergence suppresses it. In the localized regime, these two effects compete, leading to a non-monotonic entanglement evolution. Contrastingly, no non-monotonic behavior appears in the delocalized phase because convergence dominates dephasing. In the non-interacting case of $V = 0$, the localization transition is believed to coincide with the real-complex transition [33, 34, 54], while in the interacting case of $V \neq 0$, whether the superposition (4.23) converges to a non-equilibrium steady state on the MBL side is a more subtle issue.

Finally, we discuss the behavior of number entropy. In the delocalized phase, the damped oscillatory behavior mentioned earlier is more obvious. As W increases, the damped oscillation disappears and is replaced with a non-monotonic behavior with a broader maximum. On top of the non-monotonic behavior, a speedy oscillatory component is also recognized. Such an oscillatory component is also obvious in the non-interacting case, particularly in the localized regime. In the non-interacting limit the disappearance of damped oscillation coincides with the localization transition. Here, we have shown that this is also the case in an interacting system.

5.4 Effect of finite size and nonequilibrium steady state

Let us comment on the effects of system size. In the three rows of panels in Fig. 5.5, we compare the evolution of the entanglement entropies: (a)–(d) $S_{\text{tot}}(t)$, (e)–(h) $S_{\text{num}}(t)$, and (i)–(l) $S_{\text{conf}}(t)$ for systems of different system size L . Note that the entropies are normalized by the “Page value” [79], given in the case of $N_A = N_B = L/2$ as

$$S_{\text{Page}} = \frac{L}{2} \log 2 - \frac{1}{2}. \quad (5.2)$$

Note that S_{Page} is proportional to the size L of the system, If the entanglement entropies calculated at different system size L are size independent, then it implies that they obeys the volume law over the range of parameters in question. In the Hermitian case, the magnitude of $S_{\text{tot}}(t)$ is size independent [25, 80] at

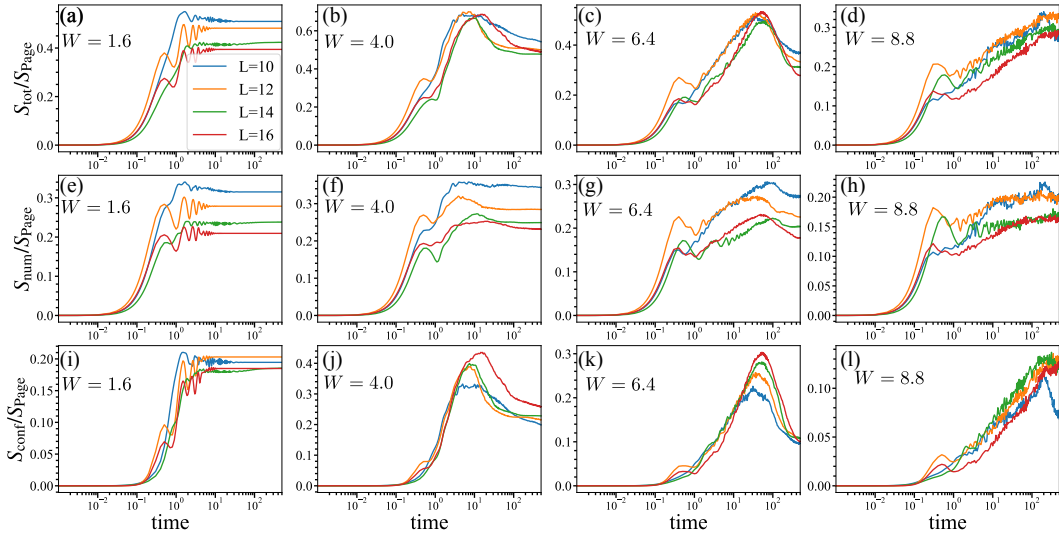


Figure 5.5: Time evolution of the entanglement entropies obtained by the average over 50 samples with different θ_0 in the density-wave type initial state. The first row [panels (a)–(d)], second row [panels (e)–(h)], and third row [panels (i)–(l)] represent $S_{\text{tot}}(t)$, $S_{\text{num}}(t)$, and $S_{\text{conf}}(t)$, respectively. The system is both non-Hermitian $g = 0.6$ and interacting $V = 2$. Each column represents data at $W = 1.6, 4.0, 6.4, 8.8$ from left to right. Curves plotted in different colors correspond to different system sizes as indicated in the inset of panel (a). Taken from Fig. 11 of Ref. [74]. ©2022 American Physical Society.

the stage of rapid initial growth (area law), while its saturation value after a sufficiently long time is size-dependent ($\propto L$), obeying a volume law [21, 22]. In the first row of Fig. 5.5, where different panels correspond to different strengths of disorder W with $g = 0.6$, the total entanglement entropy $S_{\text{tot}}(t)/S_{\text{Page}}$ is plotted for different system sizes L . The magnitude of $S_{\text{tot}}(t)/S_{\text{Page}}$ clearly decreases with an increase in L in panel (a), implying an area-law behavior. In panels (b) and (c), it becomes size-independent at its maximum ($t \simeq 3\text{--}7 \times 10^1$), suggesting a volume-law behavior. For $W = 4.0$ in panel (b) and $W = 6.4$ in panel (c), both values of W are assumed to be not far from W_c at $V = 2$. As W is further increased [panel (d): $W = 8.8$], the second growth of $S_{\text{tot}}(t)$ (a linear growth region in the logarithmic time scale) lasts longer, and the maximum of $S_{\text{tot}}(t)$ is not really achieved in the time scale shown in the panel.

Comparing panels (a), (e), and (i), the area-law behavior of S_{tot} stems from that of S_{num} , while comparing panels (c), (g), and (k), the volume-law behavior of $\text{Max } S_{\text{tot}}$ results from an interplay of the number and configuration entropies. The insensitivity of $\text{Max } S_{\text{tot}}$ to the system size L suggests that the non-monotonic evolution of the entanglement entropy specific to the non-Hermitian many-body system will also occur in case of a larger system size L .

For further clarifying this point in panel (a) of Fig. (5.6), we have plotted the ratio

$$f_{\text{Im}} = D_{\text{Im}}/D, \quad (5.3)$$

where D_{Im} is the number of eigenenergies with a nonzero ($|\text{Im} E_\mu| > 10^{-13}$) imaginary part $\text{Im } E_\mu$, while D is the dimension of the Hilbert space, i.e., the total number of eigenenergies. The existence of nonzero $\text{Im } E_\mu$ leads to suppression

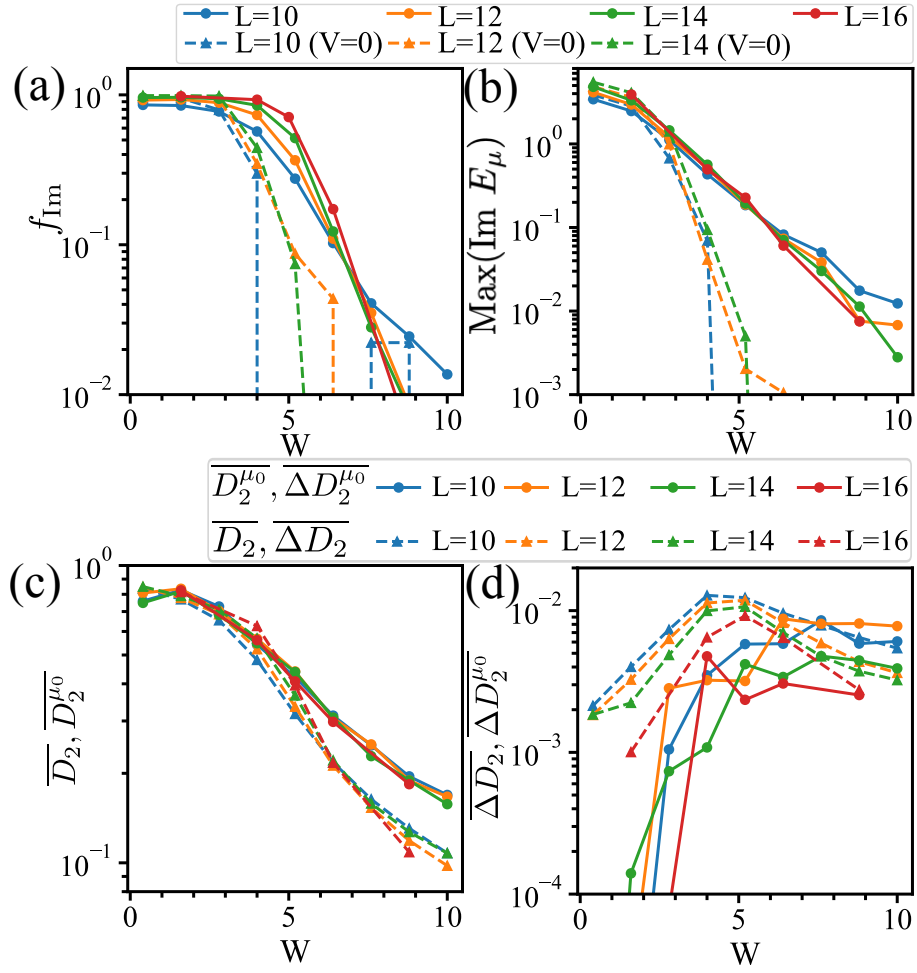


Figure 5.6: Size dependence of the (a) fraction of imaginary eigenvalues: f_{Im} [cf. Eq. (5.3)], (b) $\text{Max}(\text{Im } E_\mu)$, (c) multifractal dimension D_2 , and (d) its fluctuation: ΔD_2 . Data acquired for the interacting case: $V = 2$ (connected by solid lines) is compared with the non-interacting case: $V = 0$ (connected by broken lines). Different colors correspond to different system sizes: $L = 10, 12, 14$, and 16 . The θ_0 -average is obtained over 50 samples. Taken from Fig. 12 of Ref. [74]. ©2022 American Physical Society with slight modification.

of the superposition (4.23), leading to the suppression of the entanglement entropies. The delocalized eigenstates are susceptible to the non-reciprocity g of hopping, generating a finite imaginary part in the eigenenergy. Thus, the quantity f_{Im} measures the fraction of delocalized eigenstates in the total ensemble of eigenstates. Panel (a) of Fig. 5.6 exhibits the evolution of the fraction f_{Im} as a function of W for systems of different sizes L . As W is increased, f_{Im} decreases, first gradually and subsequently swiftly: the more drastic this tendency, the larger the size L . Furthermore, the curves corresponding to a different system size L practically crosses at the same point at a value of $W = W_c \simeq 7$ at least in the interacting case of $V = 2$ corresponding to the solid curves in panel (a).⁵ In a sufficiently large system of size L , the curve $f_{\text{Im}}(W)$ tends to become a sharply

⁵In the non-interacting case of $V = 0$ corresponding to dashed curves in panel (a) of Fig. 5.6, the change of $f_{\text{Im}}(W)$ becomes too drastic, so that one cannot really see the crossing itself, but the overall behavior of $f_{\text{Im}}(W)$ is similar to this interacting case.

edged function: $f_{\text{Im}}(W) \simeq 1$ for $W < W_c$, while $f_{\text{Im}}(W) \rightarrow 0$ for $W > W_c$. In this case, all the eigenstates, including the highly excited states, experience a complex-to-real transition of eigenvalues at $W = W_c$.

In panel (b) of Fig. 5.6, we compare the (ensemble-averaged) maximal value of $\text{Im } E_\mu$ in the cases of $V = 0$ and $V = 2$. As expected, in the non-interacting case: $V = 0$, the magnitude of $\text{Max}(\text{Im } E_\mu)$ experiences a sudden fall at the crossing (size-independent) point: $W = W_c \simeq 3 - 4$. On the two sides of this transition point, the behavior of $\text{Max}(\text{Im } E_\mu)$ exhibits a clear change that tends to magnify as the system size L increases. In particular, in the localized phase ($W > W_c$), the magnitude of $\text{Im } E_\mu$ tends to vanish as L increases. In the interacting case ($V \neq 0$) [Fig. 5.6 (b) solid curves], the ensemble-average of $\text{Max}(\text{Im } E_\mu)$ does not exhibit a sudden fall; instead, it gradually decays over a broad range of W . It exhibits no clear signature in the ETH–MBL crossover/transition regime: $W \simeq W_c$. Additionally, it exhibits no dependence on the system size L . Based on these observations, we guess that generically, $\text{Im } E_\mu$ remains finite even on the MBL side: $W > W_c$; i.e., the superposition (4.23) converges to a non-equilibrium steady state $|\mu\rangle = |\mu_0\rangle$, which has the maximal $\text{Im } E_\mu$, although it may consume a sufficiently long time.⁶ To understand the nature of this steady state $|\mu_0\rangle$, it is important to understand if it really is in a localized state. This question arises, because one usually associates the imaginary part of E_μ with an extended state, as explained in Section 2.3. To clarify this point, we have estimated the multi-fractal dimension

$$D_2^\mu = -\frac{\log(\sum_{\nu=1}^D |c_\nu^\mu|^4)}{\log(D)}, \quad (5.4)$$

encoding the (de)localized nature of the eigenstate $|\mu\rangle$; $D_2^\mu = 1$ ($= 0$) corresponds to a fully delocalized (localized) eigenstate. c_ν^μ 's is the amplitude of computational basis $|\nu\rangle = |n_1 n_2 \cdots n_L\rangle$ of the μ th eigenstate, and D is the dimension of the many-body Hilbert space. In panel (c) of Fig. 5.6, disorder averaged $\overline{D_2^{\mu_0}}$ (represented by solid lines) is compared with the disorder and all eigenstates averaged $\overline{D_2}$ (represented by broken lines).

The plots show that in the deep MBL regime, the eigenstates $|\mu_0\rangle$ exhibit a localized tendency, even though its eigenenergy E exhibit a finite imaginary part; to be precise, the state $|\mu_0\rangle$ is less localized than the other eigenstates. Panel (d) of Fig. 5.6 exhibits the variance $\overline{\Delta D_2}$ of the multi-fractal dimension as a function of W , which suggests a qualitatively different behavior in the ETH–MBL crossover regime for $\overline{\Delta D_2}$ and $\overline{\Delta D_2^{\mu_0}}$. To summarize, the superposition (4.23) indeed converges to a non-equilibrium steady state $|\mu_0\rangle$ even in the deep MBL phase, while the destined state $|\mu_0\rangle$ shows a spatially localized signature.

5.5 Profile of the reduced density matrix

Let us finally visualize how different stages in the time evolution of the entanglement entropy can be understood from the behavior of the reduced density

⁶The authors of Ref. [36] have reported that $\max \text{Im}(E_\mu)$ also shows the real-complex transition. In fact, in a sufficiently large disorder strength ($W \sim 10$), in panel (b) of Fig. 5.6, $\max \text{Im}(E_\mu)$ also weakly shows size-dependent behavior. However, study for $\max \text{Im}(E_\mu)$ remains an underway, so that we have concluded that $\max \text{Im}(E_\mu)$ is finite in the numerically accessible system size.

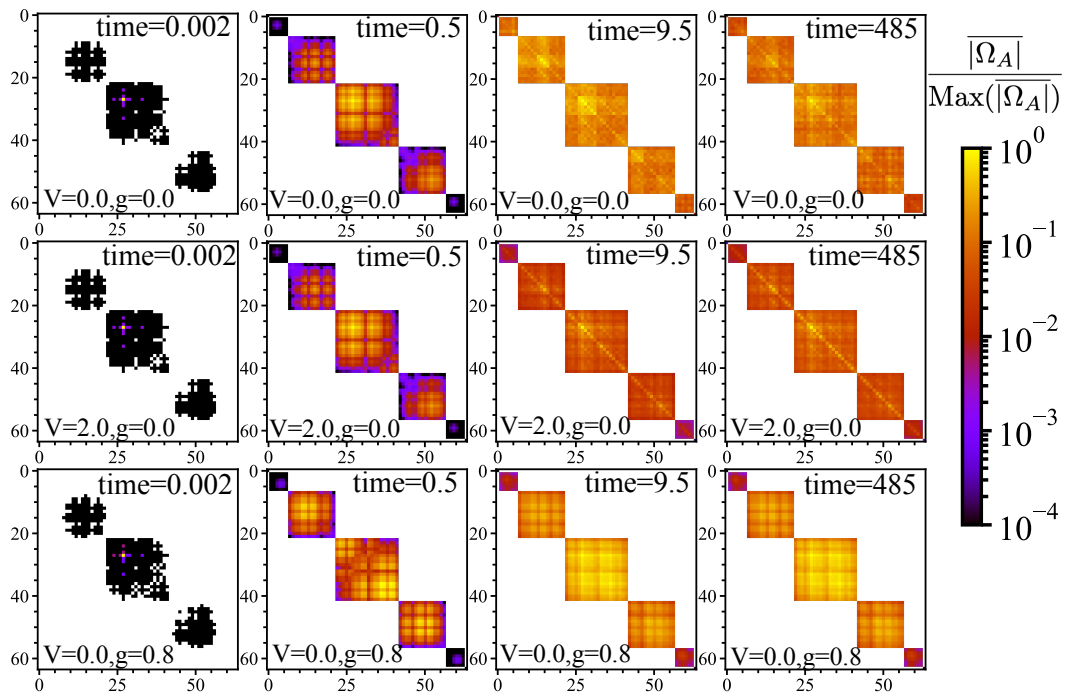


Figure 5.7: Evolution of the reduced density matrix in the wave-packet dynamics. The first, second, and third row, respectively, show the results in the non-interacting ($V = 0$) and Hermitian ($g = 0$) case, those in the interacting ($V \neq 0$) and Hermitian ($g = 0$) case, and those in the non-interacting ($V = 0$) and non-Hermitian ($g \neq 0$) case. The same initial state as in Fig. 5.1 is used and the θ_0 -average is obtained over 50 samples. Taken from Fig. 13 of Ref. [74]. ©2022 American Physical Society.

matrix $\Omega_A(t)$. In the twelve panels of Fig. 5.7, we have plotted the elements of $\Omega_A(t)$ at different times to visualize its time evolution. We note that there are 4–5 characteristic stages in the evolution of $\Omega_A(t)$.

In the first row of Fig. 5.7, we start with the Hermitian case ($g = 0$) with no interaction ($V = 0$). At $t = 0$, the initial state $|\Psi(t)\rangle$ is chosen to be a simple product state, so that the reduced density matrix $\Omega_A(t = 0)$ includes a single finite element ($= 1$) in one of the diagonals. As time passes by, the region of a finite matrix element (represented by bright spots in the panels) spreads. However, for a while, most of the amplitudes are limited within the same diagonal block in certain Ω_{N_j} ($N_j = 0, 1, \dots, 5, 6$) [cf. Eq. (3.27)]⁷ as is seen in the first panel from the left ($t = 0.002$). From the start of quench dynamics, the system is susceptible to the process of wave packet spreading; however, as far as N_j is kept unchanged, such dynamics does not lead to an immediate increase of the number entropy. After a certain time, bright spots start to appear in the neighboring blocks as is seen in the second panel ($t = 0.5$), and they finally become distributed almost equally in all the blocks as is observed in the third and fourth panels ($t = 9.5, 485$). It is expected that the number entropy experiences a rapid growth over this period and becomes saturated afterwards.

Next, we consider interaction ($V \neq 0$). The corresponding results are shown

⁷Recall that the reduced density matrix Ω_A is block diagonalized as in Eq. (3.27) with Ω_{N_j} representing a block in which the number of particles is restricted to N_j .

in the second row of Fig. 5.7. In the first two panels, the evolution of $\Omega_A(t)$ appears similar to the non-interacting case, that is, bright spots tend to spread over all different blocks as time passes by, and meanwhile the number entropy tends to be saturated. In the third and fourth panels, the bright spots are distributed equally across all the blocks as in the noninteracting case; however, here they converge on the diagonals inside each block Ω_{N_j} .⁸ This is due to dephasing [22]. Due to interaction $V \neq 0$, off-diagonal matrix elements tend to acquire a random phase and vanish on average after certain time. Dephasing leads to increase of the configuration entropy $S_{\text{conf}}(t)$; thus, in the present case after the number entropy is saturated, the total entanglement entropy $S_{\text{tot}}(t)$ continues to increase with no systematic bound, except the one due to the size of the system.

In the non-interacting ($V = 0$) and non-Hermitian ($g \neq 0$) case (see the third row of Fig. 5.7), the overall behavior of the evolution of the reduced density matrix $\Omega_A(t)$ resembles the Hermitian case in the first row except that here the pattern of the matrix elements appears considerably regular inside each block Ω_{N_j} , while the pattern appears random in the Hermitian case ($g = 0$). The reason is the following: in the regime of weak W , the eigenenergy E is typically complex, so that in the time evolution of a many-body wave packet $|\Psi(t)\rangle$ in Eq. (4.23), a single eigenstate $|\mu_0\rangle$ with the maximal imaginary part $\text{Im } E_\mu$ tends to predominate in the superposition. This tendency in the evolution of the entanglement entropy $S_{\text{tot}}(t)$ (cf. Fig. 5.1) has already been observed; in the regime of weak W , $S_{\text{tot}}(t)$ speedily converges to a fixed value and practically shows no fluctuation.

⁸In the non-interacting case (first row), on contrary, the bright spots spread over all parts of the matrix almost randomly in each block Ω_{N_j} .

Chapter 6

Concluding remarks

A century has passed, since quantum mechanics first appeared in the history of mankind. In its one-century-long history, quantum mechanics has been applied to the description of sub-atomic objects in various of circumstances. The discrete quantized spectrum of eigenenergies (the eigenvalues of the Hamiltonian ¹) for electrons trapped in the atom is a hallmark of quantum mechanics. The corresponding eigenfunctions take a spatial profile that can be naturally interpreted as a bound state. Quantum mechanics has been widely applied to the description of matter, leading to the birth of the field of condensed-matter physics, wherein matter is analyzed from a microscopic perspective. In this subfield, roles of periodic crystalline structure, fermionic/bosonic statistics, disorder in the form of a random potential, and many-body effects stemming from interparticle interaction have been extensively studied.

In this thesis, I have focused on the fact that the (eigen) wave functions tend to be localized in the presence of a random potential, and how this phenomenon, also known as Anderson localization, is modified by the presence of interparticle interaction. ² I have also considered the fact that in generic circumstances, our system is inevitably influenced by the environment. Namely, we regard our system as an open quantum system, i.e., a closed quantum mechanical system (described by a Hermitian Hamiltonian) coupled to an environment. Following the standard procedure to determine an effective Hamiltonian, we trace out the environment, and typically establish a non-Hermitian Hamiltonian as an effective model. Finally, I have focused not only on the eigenstates of such an effective Hamiltonian, but also on quantum dynamics, i.e., the time evolution of a given initial state. Particular attention is paid to the entanglement entropy that quantifies the complexity of the state as a function of time.

In Chapter 2, we have reviewed the so-called localization phenomena that occur in the presence of random potentials. We naturally started with the Hermitian case, and subsequently considered the non-Hermitian case as well. As an illustrative example, we have discussed in detail the case of the so-called AA model, in which a quasi-periodic potential mimics the random potential. In this case, a duality argument enables us to analytically determine the localization–delocalization point. Naturally, we have numerically checked the validity of this argument by demonstrating how an eigenstate localizes as disorder strength in-

¹The Hamiltonian is presumed to be Hermitian [81].

²In the interacting case, eigenstate thermalization hypothesis (ETH) and many-body localization (MBL) have been the two competing key paradigms; at least in the Hermitian case.

creases. We have subsequently introduced the so-called Hatano–Nelson model (i.e., a one-dimensional tight-binding model with non-reciprocal hopping) as a prototypical example of a non-Hermitian effective Hamiltonian. We have described how a localization–delocalization transition becomes possible in this spatially one-dimensional³ but non-Hermitian model. We have also emphasized that the wave-packet dynamics in this model is also extremely peculiar.

In Chapter 3, we have reviewed many-body localization, which is the localization phenomenon in an interacting many-body system. A remarkable feature of interacting systems is the appearance of a delocalized phase even in one dimension. A many-body delocalized phase generally satisfies ETH that justifies thermalization in an isolated many-body quantum system. We have introduced the definition of thermalization in an isolated many-body system and shown how the ETH justifies such thermalization. We have also introduced the phenomenological picture of MBL and shown the breaking of the ETH. Thereafter, we introduced the concrete procedures for calculating S_{tot} and more subdivided S_{tot} , i.e., S_{num} and S_{conf} . We reviewed how S_{tot} characterizes the static and dynamical properties of the ETH and MBL phases. For static property, ETH-MBL transition involves the transition of S_{tot} from a volume-law (ETH phase) to an area-law (MBL phase). For dynamical property, S_{tot} exhibits a power-law growth with time in the ETH phase while a logarithmic growth in the MBL phase. Based on the behavior of S_{tot} in the Hermitian systems, we reviewed the dynamical behavior of S_{tot} in the non-Hermitian system with non-reciprocal hopping and emphasized the open problem which may be overlooked.

In Chapter 4, we have highlighted the nature of the unusual wave packet spreading in a non-Hermitian system with non-reciprocal hopping (Hatano–Nelson model) [Eqs. (4.1) and (4.21)]. Disorder has been modeled by a quasi-periodic potential (Aubry–André model) [Eq. (4.2)]. In a Hermitian system, a wave packet spreading is gradually suppressed by disorder. Contrastingly, in a non-Hermitian system, it does not occur even in the clean limit, at least in the Hermitian way. The wave packet rather slides instead of spreading. The disorder tends to localize a wave function, whereas the non-reciprocity tends to delocalize it. Weak disorder exerts negligible effect on this sliding behavior. When the disorder becomes comparable to non-reciprocity, this characteristic behavior tends to be replaced with a cascade-like wave packet spreading analogous to the Hermitian case. We have clearly demonstrated the mechanism [see Eq. (4.17), and related arguments] why the wave packet slides instead of spreading in our system and how this behavior tends to be destroyed by the quasi-periodic potential (cf. Fig. 4.3). In the non-Hermitian case, the fundamental principle that governs the wave packet spreading is different from that in the Hermitian case.

In Chapter 5, we have seen how such unusual wave packet spreading in the non-Hermitian model leads to anomalous behaviors in the entanglement behavior.⁴ First, the specific wave packet spreading mentioned leads to strong suppression of the entanglement entropy, especially, in the delocalized phase as the non-Hermiticity g increases. Second, in the presence of interaction, a finite imaginary part of the eigenenergy combined with the logarithmic growth (effect of

³A localization-delocalization transition usually does not occur under such low dimensionality.

⁴As for another anomalous feature in the entanglement dynamics in a non-Hermitian PT model, see Refs. [82, 83].

dephasing) leads to a characteristic non-monotonic behavior of the entanglement entropy. We have observed that the maximum value of entanglement in the time evolution becomes maximal at (or at least near) the delocalization–localization transition, thus containing information regarding the location of the transition. This, in turn, signifies that the non-reciprocity g can be used as a probe for determining the localization length ξ in the Hermitian system [73], since g is directly related to ξ ; i.e., $\xi = g^{-1}$ [see Eq. (4.5), and related footnote on it]. Note that identifying the critical localization length ξ_c is a key to reveal the nature of the ETH–MBL transition [67]. The size dependence of the entanglement dynamics shows that the entanglement entropy $S_{\text{tot}}(t)$ at its maximum in the time evolution [i.e., $\text{Max } S_{\text{tot}}(t)$] obeys the volume law, while under other circumstances (typically, in the delocalized phase) $S_{\text{tot}}(t)/S_{\text{Page}}$ tends to decrease with an increase in L , suggesting an area law. Thus, the entanglement entropy in a non-Hermitian system exhibits an unusual area–volume–area law type crossover as a result of the interplay between non-Hermiticity and the interaction.

As shown in Ref. [38], collapse of the superposition in the initial state and convergence to a single destined eigenstate $|\mu_0\rangle$ with maximal $\text{Im } E_{\mu_0}$ play a central role in the behavior of the entanglement entropy in this non-Hermitian system. Here, we have verified this point through analyses of the entanglement using different indices (e.g., number and configuration entropies) and in a wide range of parameter regimes. In the localized side, most of the eigenstates are localized; however, a few eigenstates still include a small but finite imaginary part $\text{Im } E$, sufficient to compete with the logarithmic growth (dephasing) at least over an extremely long time scale, leading to the characteristic non-monotonic behavior of $S_{\text{tot}}(t)$.

Finally, extending the analyses performed in this study to systems of larger size is challenging. In Hermitian systems, Krylov-based time evolution [25] and tensor network techniques [72, 84, 45] are known to be applicable to deal with large-sized systems. The extension of these techniques to the non-Hermitian case is a potential direction of future work.

Appendix A

Notes on the choice of the boundary condition

The non-Hermitian system with non-reciprocal hopping is extremely sensitive to the choice of the boundary condition. Under the open boundary condition (OBC), all the bulk wave functions tend to localize near a boundary of the system. This is referred to as non-Hermitian skin effect [85, 86]. All the eigenvalues are real in this case. Contrastingly, under the periodic boundary condition (PBC), wave functions extend over the entire system (i.e., no non-Hermitian skin effect), and eigenvalues become complex.

The sensitivity of the system to the boundary condition has already been recognized in the original studies of Hatano and Nelson [33, 34]. Recent intensive discussions on non-Hermitian topological insulators have revealed its further consequences. In topological insulators, the bulk topology under the PBC is in one-to-one correspondence with the appearance/disappearance of topological boundary states under the OBC (the bulk-boundary correspondence). In a non-Hermitian system that is subjected to the non-Hermitian skin effect, the eigen wave functions are localized under the OBC, whereas they are extended under the PBC. This sharp difference results in the breaking of the bulk-boundary correspondence [85, 86, 87, 88]. As another remark, the non-Hermitian skin effect is proposed to be topological; its occurrence under the OBC is protected by a specific winding property of the complex energy spectrum under the PBC [89].

Under the PBC, the eigenenergies of the system takes complex values; particularly, the system exhibits a complex spectrum in the clean limit. The complex nature of the spectrum ($\text{Im } E \neq 0$) is closely related to the plane wave nature of the eigen wave function. Under the OBC, this is no longer true even in the clean limit. In the presence of weak disorder, the eigen wave functions are extended as far as it is not exceedingly strong and that is sufficient for maintaining the complex spectrum. Exceedingly strong disorder causes the eigen wave function to be localized, pushing the spectrum toward the real axis. Thus, the delocalization–localization transition in this system inevitably accompanies a spectral transition from complex to real. In an interacting system $V \neq 0$, one can expect that this still holds. Indeed, based on the observation that numerically estimated critical points of the ETH–MBL and complex–real transitions are close, the authors of Ref. [36] conjecture that the two transitions actually coincide in the thermodynamic limit. This is also reinforced by certain analytic arguments. In addition to the conjectured double transition, the authors of Ref. [37] highlighted the third topological transition, which is described in the last paragraph as “ at the

double transition, the winding property of the complex spectrum under the PBC also changes, which is in one-to-one correspondence with the disappearance of the non-Hermitian skin effect under the OBC ” [37].

Appendix B

Free particle wave-packet dynamics in a Hermitian system

The stationary phase approximation is the guiding principle describing the spreading of a wave packet in the Hermitian limit. An explanation of this is given in this Appendix. The Hamiltonian

$$H_{hs} = \sum_j -J(|j\rangle\langle j+1| + |j+1\rangle\langle j|), \quad (\text{B.1})$$

which is equivalent to Eq. (4.1) at $g = 0$ and $W = 0$, is used below. Its eigenenergy and eigenvector specified by a wave number k are $\epsilon_k = -2J \cos(k)$ and $|k\rangle = \frac{1}{\sqrt{L}} \sum_j \exp(ikj)|j\rangle$, respectively. Let us consider the time evolution of the wave packet with an initial state that is localized at site j_0 . Its time evolution is expressed as

$$\begin{aligned} |\Psi(t)\rangle &= \sum_k e^{i2J \cos(k)t} |k\rangle \langle k | \Psi(t=0)\rangle \\ &= \frac{1}{\sqrt{L}} \sum_{k,j} e^{i2J \cos(k)t} e^{ik(j_0-j)} |j\rangle \\ &\sim \frac{1}{2\pi} \sum_x \int_0^{2\pi} dk e^{i2J \cos(k)t} e^{ikx} |x\rangle \\ &= \frac{1}{2\pi} \sum_x i^x \int_{-\pi}^{\pi} e^{-i2J \sin(k)t} e^{ikx} dk |x\rangle = \sum_x i^x \tilde{J}_x(2Jt) |x\rangle, \end{aligned} \quad (\text{B.2})$$

where $\tilde{J}_x(2Jt)$ is the Bessel function.

Figure B.1(a) shows the time evolution of $|\Psi(j, t)|$ at site j (abscissa) at time t (ordinate) expressed by a variation of plot colors indicated in the color bar, where $\Psi(j, t)$ is defined as $|\Psi(t)\rangle = \sum_j \Psi(j, t)|j\rangle$. One observes that the wave packet symmetrically spreads in the entire system. This indicates that $|\Psi(j_0, t)|$ approaches 0 in the limit of $t \rightarrow \infty$, exhibiting the delocalization tendency. That is quantified by the return probability (RP) defined by

$$\text{RP} = |\langle \Psi(t=0) | \Psi(t) \rangle|^2. \quad (\text{B.3})$$

In the limit of $t \rightarrow \infty$, RP assumes 0 in the delocalized phase, while it assumes a finite value in the localized phase. Hence, one can characterize the localization–delocalization transition by using RP. In the delocalized phase, the wave packet

spreads throughout the system, so that $|\langle \Psi(t=0) | \Psi(t) \rangle|$ becomes 0 in the limit of $t \rightarrow \infty$. In contrast, in the localized phase, a large portion of the wave packet remains in the initial state, so that $|\langle \Psi(t=0) | \Psi(t) \rangle|$ remains finite even in the limit of $t \rightarrow \infty$. The free particle case belongs to the delocalized phase. This can

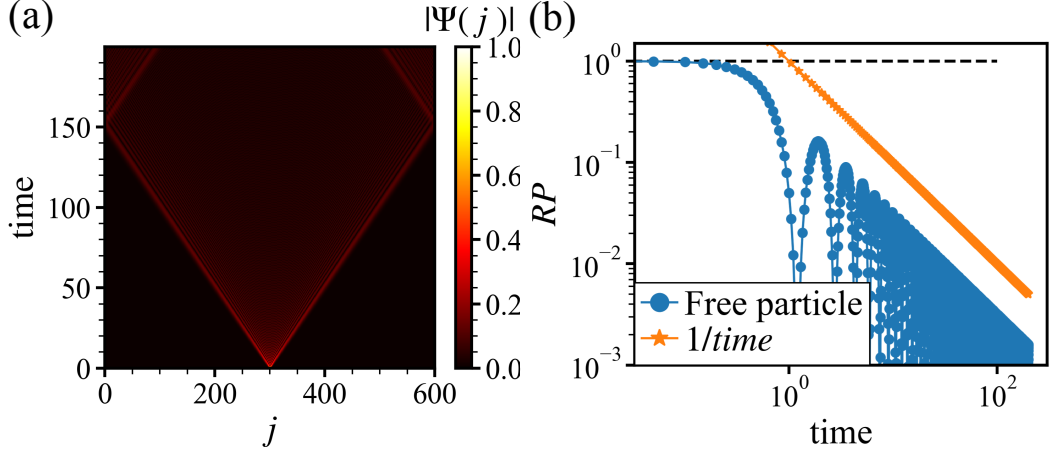


Figure B.1: Free particle dynamics in the Hermitian case: (a) $|\Psi(j,t)|$ and (b) RP as a function of time. Data are obtained in the system of $L = 601$ with the initial state localized at $j_0 = 301$. The black dotted line in panel (b) represents the line of $RP=1$.

be seen in the asymptotic behavior of $\langle \Psi(t=0) | \Psi(t) \rangle$ by using the stationary phase approximation. This result is

$$\begin{aligned}
 \langle \Psi(0) | \Psi(t) \rangle &= \frac{1}{2\pi} \int_0^{2\pi} dk e^{i2J \cos(k)t} \\
 &\sim \frac{1}{2\pi} \int_{-\infty}^{\infty} dk (e^{i2Jt(1+\frac{1}{2}(k-1)^2)} + e^{i2Jt(-1-\frac{1}{2}(k-1)^2)}) \\
 &= \frac{1}{\sqrt{4t}} (e^{i2Jt-\frac{i\pi}{4}} + e^{-i2Jt+\frac{i\pi}{4}}) \\
 &= \frac{1}{\sqrt{t}} \cos(2Jt - \frac{\pi}{4}), \tag{B.4}
 \end{aligned}$$

where the stationary phase points are $k = 0$ and $k = \pi$. RP is immediately obtained as

$$RP = |\langle \Psi(0) | \Psi(t) \rangle|^2 \sim \frac{1}{t}, \tag{B.5}$$

which vanishes in the limit of $t \rightarrow \infty$. Figure B.1(b) shows that RP in the free particle case decreases as time increases. This behavior is consistent with the asymptotic solution expressed in Eq. (B.5), indicating that the stationary phase approximation correctly characterizes the wave-packet dynamics in the Hermitian limit.

Appendix C

Free particle wave-packet dynamics in a non-Hermitian system with $\text{Im } \epsilon_k \neq 0$

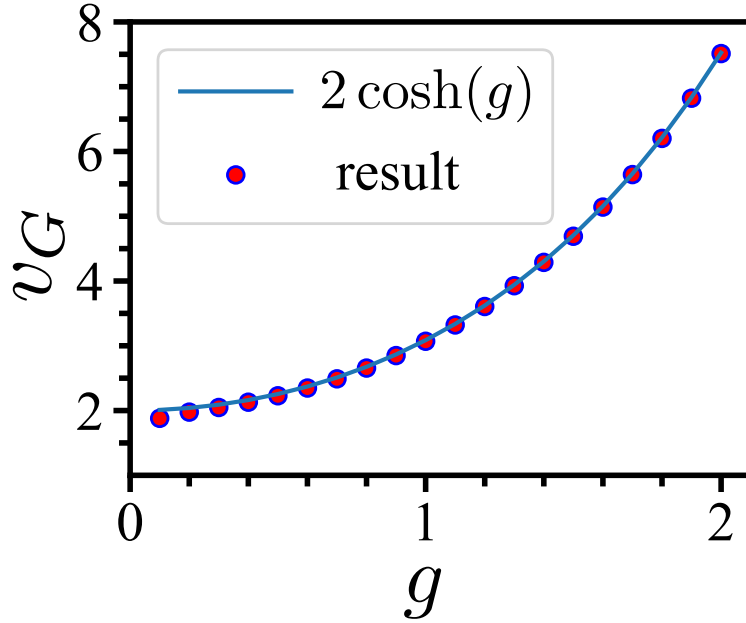


Figure C.1: g dependence of the sliding velocity $v_G = [x_G(t) - x_G(0)]/t$ in the case of $W = 0$. From the results shown in Fig. 4.4 (a), data at $W = 0$ is extracted and replotted as a function of g . The solid line represents Eq. (C.3). Data are obtained in the system of $L = 601$ and $\theta_0 = 0$ (no disorder averaging) and with the initial state localized at $j_0 = 580$. Taken from Fig. 14 of Ref. [74]. ©2022 American Physical Society.

Let us consider a free particle motion prescribed by the Hamiltonian (4.1). For simplicity, we switch off the quasi-periodic potential (4.2); $W = 0$. In this disorder-free case, the eigenstates of the Hamiltonian (4.1) under the PBC take the form of a plane wave e^{ik} , while the corresponding eigenenergies ϵ_k become complex; refer to Eqs. (4.14) and (4.15). considering the initial state $|\psi(t=0)\rangle$ as shown in Eq. (4.7), we consider its time evolution Eq. (4.10). Considering the limit $L \rightarrow \infty$, we replace the summation over k in the last line of Eq. (4.10) by an integral:

$$|\psi(t)\rangle = \sum_j |j\rangle \int_0^{2\pi} dk \frac{1}{\sqrt{2\pi}} e^{2i \cos(k-ig)t + ik(j_0-j)}. \quad (\text{C.1})$$

The one-body spectrum $\epsilon = \epsilon_k$ is complex as in Eq. (4.14), and its imaginary part $\text{Im } \epsilon_k$ becomes maximal at $k = k_0 = -\frac{\pi}{2}$. Accordingly, in the integral over k in Eq. (C.1), the dominant contributions governing the long time dynamics stem from those near $k = k_0$;

$$\begin{aligned}
|\psi(t)\rangle &\simeq \sum_j |j\rangle \int_{-\frac{\pi}{2}-\delta k}^{-\frac{\pi}{2}+\delta k} dk \frac{1}{\sqrt{2\pi}} e^{2i \cosh(g)(k+\frac{\pi}{2})t} \\
&\quad \times e^{2 \sinh(g)(1-\frac{1}{2}(k+\frac{\pi}{2})^2)t+i(k+\frac{\pi}{2})(j_0-j)} \\
&\simeq \sum_j |j\rangle \int_{-\infty}^{\infty} dk \frac{1}{\sqrt{2\pi}} e^{2i \cosh(g)kt} \\
&\quad \times e^{2 \sinh(g)(1-\frac{k^2}{2})t+ik(j_0-j)} \\
&= \sum_j |j\rangle \exp\left(-\frac{((j_0-j)+2 \cosh(g)t)^2}{4 \sinh(g)t}\right) \\
&\quad \times e^{2 \sinh(g)t} / \sqrt{4 \sinh(g)t}. \tag{C.2}
\end{aligned}$$

Based on the last expression, one can read the group velocity of the wave packet as

$$v_G = 2 \cosh(g), \tag{C.3}$$

which is consistent with our calculations (Fig. C.1). Note that v_G increases with the increase in g . The last expression takes the form of a Gaussian wave packet that slides in the direction imposed by g . The expanse Δx of the wave packet gradually increases in real space in the course of time as $\Delta x \simeq 2\sqrt{\sinh(g)t}$, while the corresponding width $\Delta k \sim 1/\Delta x$ in the reciprocal space tends to diminish [see Fig. 4.3 (a)]. The above features are also quite manifest in panels (a) and (b) of Fig. 4.2, although the data shown in this figure is obtained in a weak disorder case. In time evolution, the state $|\psi(t)\rangle$ as expressed in Eq. (C.1) tends to be governed by the eigenstates with maximal $\text{Im } \epsilon_k$ [see Eq. (4.17)], while the individual eigenstates take the form of a plane wave.

Note that the form of the Gaussian wave packet (C.2) suggests that it obeys a square-root scaling typical to classical diffusion dynamics. Of course, we consider the coherent quantum dynamics of the wave function $\psi(x, t)$ that is governed by the Schrödinger equation. However, in the present non-Hermitian setup, the non-reciprocal nature of the hopping strongly suppresses the interference of the complex wave function $\psi(x, t)$, characteristic to the Schrödinger quantum dynamics. As a result, the wave function $\psi(x, t)$ as expressed in Eq. (C.2) effectively obeys the classical diffusion dynamics.

Appendix D

Effects of anticommutation relation on entanglement dynamics

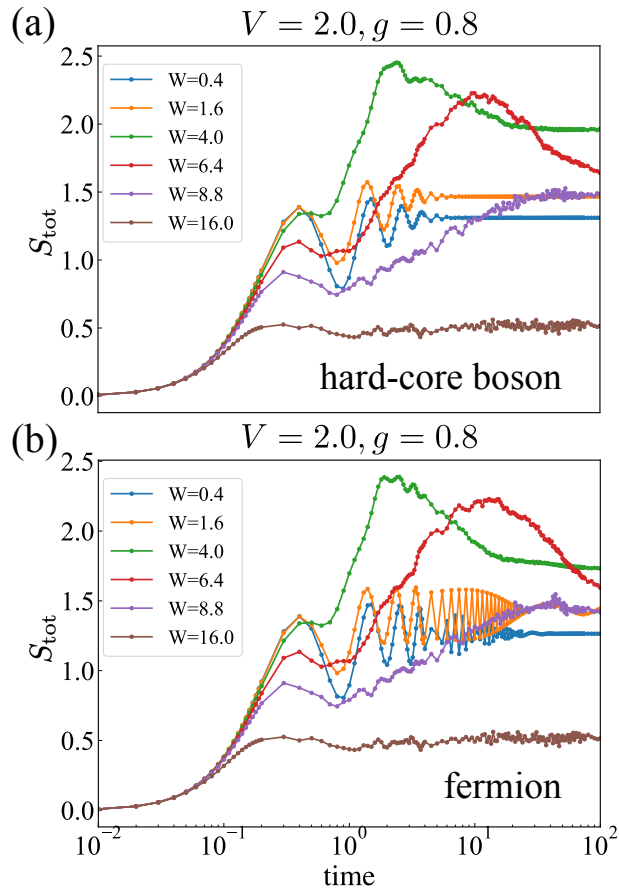


Figure D.1: Time evolution of the entanglement entropy in the (a) hard-core boson and (b) fermion models. We employ the same numerical parameters as in Fig. 5.4. Taken from Fig. 15 of Ref. [74]. ©2022 American Physical Society.

Thus far we have considered systems of hard-core bosons; cf. Refs. [36] and [37]. In a system of true fermions, the anticommutation of b_j and b_j^\dagger leads to a subtle sign difference at the periodic boundary. Here, we examine whether this sign difference results in a significant consequence in entanglement dynamics. Figure D.1 (a) shows selected plots from Fig. 5.4 (b), which demonstrates time evolution of the entanglement entropy in the case of $g = 0.8$ in the hard-core boson model. Figure D.1 (b) represents the corresponding data in the fermion

model under the same condition. In the critical and localized regimes, $W > 3-4$, the wave functions are not extended, and the corresponding fermion states are expected to be immune to the sign difference. The result of our simulation in the fermionic case confirms that the entanglement entropy exhibits essentially the same behavior in the two models, that is, the anticommutation relation plays no role in this regime. In the delocalized regime ($W < 3-4$), the wave functions are extended over the entire system, so that the resulting fermion state may be influenced by the statistics. In this regime, the entanglement entropy exhibits an oscillatory behavior in the intermediate time scale: a simple damped oscillation in the case of hard-core boson model. In the fermionic case, one can still recognize a similar oscillatory pattern; however, it does not take any longer than a simple damped oscillation and also survives longer than in the hard-core boson case. Thus, the anticommutation relation influences the behavior of the entanglement entropy in the delocalized regime at a quantitative level; however, the qualitative statements regarding its behavior in the hard-core boson model can still be applied to the fermionic case. The behavior of the entanglement entropy is essentially unchanged in the critical and localized regimes.

Appendix E

The entanglement entropy in the ETH and MBL phases (Hermitian case)

Let us comment on the relation between the entanglement entropy and the localization length. The multifractal dimension D_2 expressed in Eq. (5.4) measures the extent to which the eigenstates are localized in Hilbert space; this is related to the extent to which the wave functions are localized in real space. Thus, in the regime of strong disorder in the Hermitian case: $g = 0$, D_2 behaves asymptotically as $D_2 \sim \log(\xi)$ [67], where ξ represents the localization length in real space. This implies that the true Fock space-localization $D_2 = 0$ is generally never achieved [43, 90, 91], since ξ is generally finite in the localized phase, except in the limit $W \rightarrow \infty$.

Fock-space localization effectively restricts the available Hilbert space, thus affecting the maximal value of the entanglement entropy; cf. in the free case, it expressed as Eq. (5.2). In a more generic case with a finite D_2 , it becomes [92]

$$S_{\text{tot}} \sim D_{\text{ent}} \frac{L}{2} \log(2), \quad (\text{E.1})$$

where D_{ent} is a quantity related to D_2 :

$$D_{\text{ent}} = \begin{cases} 1, & D_2 \geq 1/2 \\ 2D_2, & D_2 < 1/2. \end{cases} \quad (\text{E.2})$$

In the ETH side of $D_2 > 1/2$, the reduction of the multifractal dimension D_2 due to a finite W does not lead to reduction of the entanglement entropy S_{tot} , while in the MBL side of $D_2 < 1/2$, S_{tot} decreases linearly with a decrease in D_2 . S_{tot} does not exhibit a finite jump at the ETH–MBL transition point of $D_2 = 1/2$ and gradually crosses over from the ETH side to the MBL side. In the time evolution of $S_{\text{tot}}(t)$ plotted in Fig. 5.1 (a), its saturated value in the long time scale remains the same in the delocalized phase of $W \leq 2$, while in the localized phase of $W > 2$, it decreases continuously from this value with an increase in W .

References

- [1] J. M. Deutsch. Quantum statistical mechanics in a closed system. Phys. Rev. A, Vol. 43, pp. 2046–2049, Feb 1991.
- [2] Mark Srednicki. Chaos and quantum thermalization. Phys. Rev. E, Vol. 50, pp. 888–901, Aug 1994.
- [3] Marcos Rigol, Vanja Dunjko, and Maxim Olshanii. Thermalization and its mechanism for generic isolated quantum systems. Nature, Vol. 452, No. 7189, p. 854–858, Apr 2008.
- [4] I. V. Gornyi, A. D. Mirlin, and D. G. Polyakov. Interacting electrons in disordered wires: Anderson localization and low- t transport. Phys. Rev. Lett., Vol. 95, p. 206603, Nov 2005.
- [5] D.M. Basko, I.L. Aleiner, and B.L. Altshuler. Metal–insulator transition in a weakly interacting many-electron system with localized single-particle states. Annals of Physics, Vol. 321, No. 5, pp. 1126–1205, 2006.
- [6] Rahul Nandkishore and David A. Huse. Many-body localization and thermalization in quantum statistical mechanics. Annual Review of Condensed Matter Physics, Vol. 6, No. 1, pp. 15–38, 2015.
- [7] Fabien Alet and Nicolas Laflorencie. Many-body localization: An introduction and selected topics. Comptes Rendus Physique, Vol. 19, No. 6, pp. 498–525, 2018.
- [8] Dmitry A. Abanin, Ehud Altman, Immanuel Bloch, and Maksym Serbyn. Colloquium: Many-body localization, thermalization, and entanglement. Rev. Mod. Phys., Vol. 91, p. 021001, May 2019.
- [9] M. Schreiber, S. S. Hodgman, P. Bordia, H. P. Lüschen, M. H. Fischer, R. Vosk, E. Altman, U. Schneider, and I. Bloch. Observation of many-body localization of interacting fermions in a quasirandom optical lattice. Science, Vol. 349, No. 6250, p. 842–845, Jul 2015.
- [10] J.-y. Choi, S. Hild, J. Zeiher, P. Schauss, A. Rubio-Abadal, T. Yefsah, V. Khemani, D. A. Huse, I. Bloch, and C. Gross. Exploring the many-body localization transition in two dimensions. Science, Vol. 352, No. 6293, p. 1547–1552, Jun 2016.
- [11] P. Roushan, C. Neill, J. Tangpanitanon, V. M. Bastidas, A. Megrant, R. Barends, Y. Chen, Z. Chen, B. Chiaro, A. Dunsworth, and et al. Spectroscopic signatures of localization with interacting photons in superconducting qubits. Science, Vol. 358, No. 6367, p. 1175–1179, Nov 2017.

- [12] J. Smith, A. Lee, P. Richerme, B. Neyenhuis, P. W. Hess, P. Hauke, M. Heyl, D. A. Huse, and C. Monroe. Many-body localization in a quantum simulator with programmable random disorder. Nature Physics, Vol. 12, No. 10, p. 907–911, Jun 2016.
- [13] Kai Xu, Jin-Jun Chen, Yu Zeng, Yu-Ran Zhang, Chao Song, Wuxin Liu, Qiujiang Guo, Pengfei Zhang, Da Xu, Hui Deng, Keqiang Huang, H. Wang, Xiaobo Zhu, Dongning Zheng, and Heng Fan. Emulating many-body localization with a superconducting quantum processor. Phys. Rev. Lett., Vol. 120, p. 050507, Feb 2018.
- [14] P. W. Anderson. Absence of diffusion in certain random lattices. Phys. Rev., Vol. 109, pp. 1492–1505, Mar 1958.
- [15] Bela Bauer and Chetan Nayak. Area laws in a many-body localized state and its implications for topological order. Journal of Statistical Mechanics: Theory and Experiment, Vol. 2013, No. 09, p. P09005, sep 2013.
- [16] David J. Luitz, Nicolas Laflorencie, and Fabien Alet. Many-body localization edge in the random-field heisenberg chain. Phys. Rev. B, Vol. 91, p. 081103, Feb 2015.
- [17] Vedika Khemani, S. P. Lim, D. N. Sheng, and David A. Huse. Critical properties of the many-body localization transition. Phys. Rev. X, Vol. 7, p. 021013, Apr 2017.
- [18] Jonas A. Kjäll, Jens H. Bardarson, and Frank Pollmann. Many-body localization in a disordered quantum ising chain. Phys. Rev. Lett., Vol. 113, p. 107204, Sep 2014.
- [19] Maksym Serbyn, Alexios A. Michailidis, Dmitry A. Abanin, and Z. Papić. Power-law entanglement spectrum in many-body localized phases. Phys. Rev. Lett., Vol. 117, p. 160601, Oct 2016.
- [20] Marko Žnidarič, Tomaž Prosen, and Peter Prelovšek. Many-body localization in the heisenberg xxz magnet in a random field. Phys. Rev. B, Vol. 77, p. 064426, Feb 2008.
- [21] Jens H. Bardarson, Frank Pollmann, and Joel E. Moore. Unbounded growth of entanglement in models of many-body localization. Phys. Rev. Lett., Vol. 109, p. 017202, Jul 2012.
- [22] Maksym Serbyn, Z. Papić, and Dmitry A. Abanin. Universal slow growth of entanglement in interacting strongly disordered systems. Phys. Rev. Lett., Vol. 110, p. 260601, Jun 2013.
- [23] Kartiek Agarwal, Sarang Gopalakrishnan, Michael Knap, Markus Müller, and Eugene Demler. Anomalous diffusion and griffiths effects near the many-body localization transition. Phys. Rev. Lett., Vol. 114, p. 160401, Apr 2015.

- [24] Yevgeny Bar Lev, Guy Cohen, and David R. Reichman. Absence of diffusion in an interacting system of spinless fermions on a one-dimensional disordered lattice. Phys. Rev. Lett., Vol. 114, p. 100601, Mar 2015.
- [25] David J. Luitz, Nicolas Laflorencie, and Fabien Alet. Extended slow dynamical regime close to the many-body localization transition. Phys. Rev. B, Vol. 93, p. 060201, Feb 2016.
- [26] Yuto Ashida, Zongping Gong, and Masahito Ueda. Non-hermitian physics. Advances in Physics, Vol. 69, No. 3, pp. 249–435, jul 2020.
- [27] Zongping Gong, Yuto Ashida, Kohei Kawabata, Kazuaki Takasan, Sho Higashikawa, and Masahito Ueda. Topological phases of non-hermitian systems. Phys. Rev. X, Vol. 8, p. 031079, Sep 2018.
- [28] G. Barontini, R. Labouvie, F. Stubenrauch, A. Vogler, V. Guarrera, and H. Ott. Controlling the dynamics of an open many-body quantum system with localized dissipation. Phys. Rev. Lett., Vol. 110, p. 035302, Jan 2013.
- [29] Takafumi Tomita, Shuta Nakajima, Yosuke Takasu, and Yoshiro Takahashi. Dissipative bose-hubbard system with intrinsic two-body loss. Phys. Rev. A, Vol. 99, p. 031601, Mar 2019.
- [30] Julia M. Zeuner, Mikael C. Rechtsman, Yonatan Plotnik, Yaakov Lumer, Stefan Nolte, Mark S. Rudner, Mordechai Segev, and Alexander Szameit. Observation of a topological transition in the bulk of a non-hermitian system. Phys. Rev. Lett., Vol. 115, p. 040402, Jul 2015.
- [31] Xiujuan Zhang, Yuan Tian, Jian-Hua Jiang, Ming-Hui Lu, and Yan-Feng Chen. Observation of higher-order non-hermitian skin effect. Nature Communications, Vol. 12, No. 1, sep 2021.
- [32] Qian Liang, Dizhou Xie, Zhaoli Dong, Haowei Li, Hang Li, Bryce Gadway, Wei Yi, and Bo Yan. Dynamic signatures of non-hermitian skin effect and topology in ultracold atoms. Phys. Rev. Lett., Vol. 129, p. 070401, Aug 2022.
- [33] Naomichi Hatano and David R. Nelson. Localization transitions in non-hermitian quantum mechanics. Phys. Rev. Lett., Vol. 77, pp. 570–573, Jul 1996.
- [34] Naomichi Hatano and David R. Nelson. Vortex pinning and non-hermitian quantum mechanics. Phys. Rev. B, Vol. 56, pp. 8651–8673, Oct 1997.
- [35] Carl M. Bender, Stefan Boettcher, and Peter N. Meisinger. PT-symmetric quantum mechanics. Journal of Mathematical Physics, Vol. 40, No. 5, pp. 2201–2229, may 1999.
- [36] Ryusuke Hamazaki, Kohei Kawabata, and Masahito Ueda. Non-hermitian many-body localization. Phys. Rev. Lett., Vol. 123, p. 090603, Aug 2019.
- [37] Liang-Jun Zhai, Shuai Yin, and Guang-Yao Huang. Many-body localization in a non-hermitian quasiperiodic system. Phys. Rev. B, Vol. 102, p. 064206, Aug 2020.

- [38] Animesh Panda and Sumilan Banerjee. Entanglement in nonequilibrium steady states and many-body localization breakdown in a current-driven system. Phys. Rev. B, Vol. 101, p. 184201, May 2020.
- [39] Pasquale Calabrese and John Cardy. Evolution of entanglement entropy in one-dimensional systems. Journal of Statistical Mechanics: Theory and Experiment, Vol. 2005, No. 04, p. P04010, apr 2005.
- [40] Gabriele De Chiara, Simone Montangero, Pasquale Calabrese, and Rosario Fazio. Entanglement entropy dynamics of heisenberg chains. Journal of Statistical Mechanics: Theory and Experiment, Vol. 2006, No. 03, pp. P03001–P03001, mar 2006.
- [41] Vincenzo Alba and Pasquale Calabrese. Entanglement dynamics after quantum quenches in generic integrable systems. SciPost Phys., Vol. 4, p. 17, 2018.
- [42] Stefano Longhi. Phase transitions in a non-hermitian aubry-andré-harper model. Phys. Rev. B, Vol. 103, p. 054203, Feb 2021.
- [43] Takahiro Orito and Ken-Ichiro Imura. Multifractality and fock-space localization in many-body localized states: One-particle density matrix perspective. Phys. Rev. B, Vol. 103, p. 214206, Jun 2021.
- [44] Takahiro Orito, Yoshihito Kuno, and Ikuo Ichinose. Deformation of localized states and state transitions in systems of randomly hopping interacting fermions. Phys. Rev. B, Vol. 105, p. 094201, Mar 2022.
- [45] Takahiro Orito, Yoshihito Kuno, and Ikuo Ichinose. Nonthermalized dynamics of flat-band many-body localization. Phys. Rev. B, Vol. 103, p. L060301, Feb 2021.
- [46] Takahiro Orito, Yoshihito Kuno, and Ikuo Ichinose. Interplay and competition between disorder and flat band in an interacting creutz ladder. Phys. Rev. B, Vol. 104, p. 094202, Sep 2021.
- [47] Takahiro Orito, Yoshihito Kuno, and Ikuo Ichinose. Exact projector hamiltonian, local integrals of motion, and many-body localization with symmetry-protected topological order. Phys. Rev. B, Vol. 101, p. 224308, Jun 2020.
- [48] Ikuo Ichinose, Takahiro Orito, and Yoshihito Kuno. Flat-band full localization and symmetry-protected topological phase on bilayer lattice systems. Phys. Rev. B, Vol. 103, p. 184113, May 2021.
- [49] Yoshihito Kuno, Takahiro Orito, and Ikuo Ichinose. Information spreading and scrambling in disorder-free multiple-spin-interaction models. Phys. Rev. A, Vol. 106, p. 012435, Jul 2022.
- [50] Takahiro Orito, Yoshihito Kuno, and Ikuo Ichinose. Quantum information spreading in random spin chains with topological order. Phys. Rev. B, Vol. 106, p. 104204, Sep 2022.

- [51] Phillip Weinberg and Marin Bukov. QuSpin: a Python Package for Dynamics and Exact Diagonalisation of Quantum Many Body Systems part I: spin chains. SciPost Phys., Vol. 2, p. 003, 2017.
- [52] Phillip Weinberg and Marin Bukov. QuSpin: a Python Package for Dynamics and Exact Diagonalisation of Quantum Many Body Systems. Part II: bosons, fermions and higher spins. SciPost Phys., Vol. 7, p. 20, 2019.
- [53] Serge Aubry and Gilles André. Analyticity breaking and anderson localization in incommensurate lattices. Ann. Israel Phys. Soc., Vol. 3, p. 133, 01 1980.
- [54] Naomichi Hatano and David R. Nelson. Non-hermitian delocalization and eigenfunctions. Phys. Rev. B, Vol. 58, pp. 8384–8390, Oct 1998.
- [55] E. Abrahams, P. W. Anderson, D. C. Licciardello, and T. V. Ramakrishnan. Scaling theory of localization: Absence of quantum diffusion in two dimensions. Phys. Rev. Lett., Vol. 42, pp. 673–676, Mar 1979.
- [56] Mahito Kohmoto. Metal-insulator transition and scaling for incommensurate systems. Phys. Rev. Lett., Vol. 51, pp. 1198–1201, Sep 1983.
- [57] Christian Aulbach, André Wobst, Gert-Ludwig Ingold, Peter Hänggi, and Imre Varga. Phase-space visualization of a metal–insulator transition. New Journal of Physics, Vol. 6, No. 1, p. 70, jul 2004.
- [58] Michele Modugno. Exponential localization in one-dimensional quasi-periodic optical lattices. New Journal of Physics, Vol. 11, No. 3, p. 033023, mar 2009.
- [59] Naomichi Hatano and Hideaki Obuse. Delocalization of a non-hermitian quantum walk on random media in one dimension. Annals of Physics, Vol. 435, p. 168615, dec 2021.
- [60] David J. Luitz. Long tail distributions near the many-body localization transition. Phys. Rev. B, Vol. 93, p. 134201, Apr 2016.
- [61] Boris L. Altshuler, Yuval Gefen, Alex Kamenev, and Leonid S. Levitov. Quasiparticle lifetime in a finite system: A nonperturbative approach. Phys. Rev. Lett., Vol. 78, pp. 2803–2806, Apr 1997.
- [62] Sthitadhi Roy, J. T. Chalker, and David E. Logan. Percolation in fock space as a proxy for many-body localization. Phys. Rev. B, Vol. 99, p. 104206, Mar 2019.
- [63] Sthitadhi Roy and David E. Logan. Fock-space correlations and the origins of many-body localization. Phys. Rev. B, Vol. 101, p. 134202, Apr 2020.
- [64] Nicolas Laflorencie, Gabriel Lemarié, and Nicolas Macé. Chain breaking and kosterlitz-thouless scaling at the many-body localization transition in the random-field heisenberg spin chain. Phys. Rev. Research, Vol. 2, p. 042033, Nov 2020.

- [65] David A. Huse, Rahul Nandkishore, and Vadim Oganesyan. Phenomenology of fully many-body-localized systems. Phys. Rev. B, Vol. 90, p. 174202, Nov 2014.
- [66] John Z. Imbrie. On many-body localization for quantum spin chains. Journal of Statistical Physics, Vol. 163, No. 5, pp. 998–1048, apr 2016.
- [67] Giuseppe De Tomasi, Ivan M. Khaymovich, Frank Pollmann, and Simone Warzel. Rare thermal bubbles at the many-body localization transition from the fock space point of view. Phys. Rev. B, Vol. 104, p. 024202, Jul 2021.
- [68] V. Ros, M. Müller, and A. Scardicchio. Integrals of motion in the many-body localized phase. Nuclear Physics B, Vol. 891, pp. 420–465, 2015.
- [69] John Z. Imbrie, Valentina Ros, and Antonello Scardicchio. Local integrals of motion in many-body localized systems. Annalen der Physik, Vol. 529, No. 7, p. 1600278, 2017.
- [70] Maksym Serbyn, Z. Papić, and Dmitry A. Abanin. Local conservation laws and the structure of the many-body localized states. Phys. Rev. Lett., Vol. 111, p. 127201, Sep 2013.
- [71] Alexander Lukin, Matthew Rispoli, Robert Schittko, M. Eric Tai, Adam M. Kaufman, Soonwon Choi, Vedika Khemani, Julian Léonard, and Markus Greiner. Probing entanglement in a many-body-localized system. Science, Vol. 364, No. 6437, pp. 256–260, 2019.
- [72] Elmer V. H. Doggen, Frank Schindler, Konstantin S. Tikhonov, Alexander D. Mirlin, Titus Neupert, Dmitry G. Polyakov, and Igor V. Gornyi. Many-body localization and delocalization in large quantum chains. Phys. Rev. B, Vol. 98, p. 174202, Nov 2018.
- [73] Sascha Heußen, Christopher David White, and Gil Refael. Extracting many-body localization lengths with an imaginary vector potential. Phys. Rev. B, Vol. 103, p. 064201, Feb 2021.
- [74] Takahiro Orito and Ken-Ichiro Imura. Unusual wave-packet spreading and entanglement dynamics in non-hermitian disordered many-body systems. Physical Review B, Vol. 105, No. 2, jan 2022.
- [75] E. H. Lieb and D. W. Robinson. The finite group velocity of quantum spin systems. Commun.Math. Phys., Vol. 28, p. 201, 1972.
- [76] Marcos Rigol, Vanja Dunjko, Vladimir Yurovsky, and Maxim Olshanii. Relaxation in a completely integrable many-body quantum system: An ab initio study of the dynamics of the highly excited states of 1d lattice hard-core bosons. Phys. Rev. Lett., Vol. 98, p. 050405, Feb 2007.
- [77] Ranjan Modak, Vincenzo Alba, and Pasquale Calabrese. Entanglement revivals as a probe of scrambling in finite quantum systems. Journal of Statistical Mechanics: Theory and Experiment, Vol. 2020, No. 8, p. 083110, aug 2020.

